The imaginary-time method for relativistic problems

V. S. Popov
Institute of Theoretical and Experimental Physics, 117218 Moscow, Russia

V. D. Mur and B. M. Karnakov
Moscow Engineering Physics Institute, 115409 Moscow, Russia

(Submitted 25 June 1997)
Pis'ma Zh. Éksp. Teor. Fiz. **66**, No. 4, 213–218 (25 August 1997)

A relativistic version of the imaginary-time method is presented. The method is used to calculate the probability w of ionization of a bound state by electric and magnetic fields of various configurations (including the case when the binding energy E_b is comparable to mc^2). The formulas cover as limiting cases both the ionization of nonrelativistic bound systems (atoms and ions) and the case $E_b=2mc^2$, when w equals the probability of electron–positron pair production from the vacuum in the presence of a strong field. © *1997 American Institute of Physics.* [S0021-3640(97)00116-3]

PACS numbers: 32.80.Rm

1. The imaginary-time method (ITM) was proposed in Refs. 1 and 2 in connection with the calculation of the probability of multiphoton ionization of atoms by a strong light wave. Subbarrier trajectories satisfying the classical equations of motion but with imaginary time t are introduced in order to describe the tunneling process. The imaginary part of the action calculated along such a trajectory determines the particle tunneling probability.

The effect of a magnetic field on the ionization of atoms and ions was recently investigated by the ITM.[3,4] The subbarrier motion of the electron was assumed to be nonrelativistic, which is valid for valence electrons. In the case of the ionization of the K shell in heavy atoms, however, relativistic effects become substantial, and to take them into account systematically (in the quasiclassical approximation) it is necessary to extend the ITM to the relativistic case. Such an extension could also be helpful in a number of problems of relativistic nuclear physics and quantum chromodynamics. We shall show that such an extension is possible for the specific problem of the ionization of a bound state whose energy $E_b=mc^2-E_0$ is comparable to the rest energy mc^2, and we shall find the main (exponential) factor in the ionization probability. We shall also briefly discuss the problem of taking the Coulomb interaction into account in the tunneling process and the calculation of the pre-exponential factor.

2. We start with the ionization of a level bound by short-range forces, under the action of electric ($\mathcal{E}$) and magnetic ($\mathcal{H}$) fields, which we assume to be static and uniform.

a) In the case when only an electric field is present the subbarrier trajectories have the form

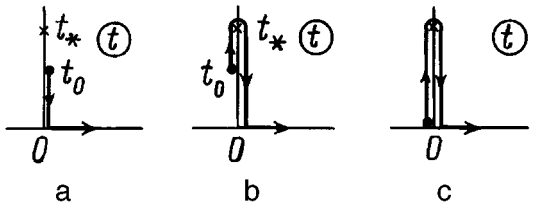

FIG. 1. Variation of the ''time'' t in subbarrier motion for a level with energy $E_0>0$ (a); $0>E_0>-m$ (b); $E_0=-m$ (c). The crosses represent the branch point $t=t_*$ of the function $[p(t)^2+m^2]^{1/2}$.

$$x=\frac{ip_\perp}{e\mathcal{E}}(\sin^{-1}\tau_0-\sin^{-1}\tau),\quad y=0,\quad z=\frac{M}{e\mathcal{E}}(\sqrt{1-\tau^2}-\sqrt{1-\tau_0^2}),\tag{1}$$

where $\tau=ie\mathcal{E}t/M$ is real and is related to the proper time s by the expression $s=-i(m/e\mathcal{E})\sin^{-1}\tau$, $M=\sqrt{m^2+p_\perp^2}$, the z axis is directed along $\vec{\mathcal{E}}$, and $p_\perp$ is the transverse momentum. The time t_0 at which the subbarrier motion starts is determined from the conditions[2]

$$\mathbf{r}(t_0)=0,\quad H(t_0)=m(1-\dot{\mathbf{r}}^2)^{-1/2}=E_0,\tag{2}$$

(in the gauge $\varphi(0,t)=\mathbf{A}(0,t)=0$ and in the approximation of a zero-range force), whence

$$et_0=\frac{im}{e\mathcal{E}}(1-\epsilon_0^2+q^2)^{1/2},\quad q=p_\perp/m.\tag{3}$$

Here $E_0=m\epsilon_0$ is the energy of the bound state ($-1\leqslant\epsilon_0<1$; the values $\epsilon_0=\pm1$ correspond to the boundaries of the upper and lower continua). The probability of electron tunneling along the trajectory (1) equals[1,2]

$$dw(\mathbf{p}_\perp)=\frac{\text{const}}{\hbar m}\exp\left\{-\frac{2}{\hbar}\,\text{Im}\;W(p_\perp)\right\}d^2p_\perp,\tag{4}$$

where W is the abbreviated action

$$W=\int_{t_0}^{0}(L+E_0)dt-(\mathbf{p}\cdot\mathbf{r})_{t=0},\quad L=-\sqrt{1-v^2}+e(\mathbf{A}\cdot\mathbf{v})-e\varphi,\tag{4a}$$

(in what follows, as a rule, $\hbar=c=1$). As the level moves deeper, t_0 moves in the complex plane, making a circuit around the branch point t_* as shown in Fig. 1. Thus

$$\begin{aligned}W&=\frac{im^2}{2e\mathcal{E}}\left[(1+q^2)\cos^{-1}\frac{\epsilon_0}{\sqrt{1+q^2}}-\epsilon_0\sqrt{1-\epsilon_0^2+q^2}\right]\\&=\frac{im^2}{2e\mathcal{E}}[\Phi(\epsilon_0)+q^2\cos^{-1}\epsilon_0+O(q^4)],\end{aligned}\tag{5}$$

$\Phi(\epsilon)=\cos^{-1}\epsilon-\epsilon\sqrt{1-\epsilon^2}$. Integrating (4) over the transverse momentum, we find the total ionization probability of the s level

$$w(\mathcal{E},\epsilon_0)=\frac{mc^2}{2\hbar}|A_\kappa|^2\frac{\mathcal{E}/F_{\rm cr}}{\cos^{-1}\epsilon_0}\exp\left\{-\frac{F_{\rm cr}}{\mathcal{E}}\Phi(\epsilon_0)\right\}, \tag{6}$$

where A_κ is the asymptotic ($r\to\infty$) coefficient of the wave function of the bound state in the absence of the field $\mathcal{E}$ (compare with formula (9) in Ref. 3) and $F_{\rm cr}=m^2c^3/e\hbar$ is the critical or Schwinger field that is characteristic in quantum electrodynamics.[5,6]

In the nonrelativistic limit ($\epsilon_0\to 1$) this formula passes into the well-known expression[7,8] for the ionization probability of negative ions (of the type H^-, Na^-, and so on). For $\epsilon_0=-1$, i.e., for a level which has dropped down to the boundary of the lower continuum (the critical charge of the nucleus $Z_{\rm cr}(1s_{1/2})=173$, (see Refs. 9–12), the exponential factor in Eq. (6) becomes $\exp(-\pi F_{\rm cr}/\mathcal{E})$ and is identical to the corresponding factor in the Schwinger formula[5] for the probability of electron–positron pair production from the vacuum in an electric field $\mathcal{E}$.

b) If the fields $\mathcal{E}$ and $\mathcal{H}$ are parallel, then the trajectory of a relativistic particle is a helix with a variable pitch. The subbarrier trajectory is obtained from the well-known equations[13] by analytical continuation in t, the contour of integration in (4a) having the same form as in Fig. 1. Finally,

$$\text{Im } W(p_\perp)=\frac{m^2}{2e\mathcal{E}}\Phi(\epsilon_0)+\sinh\left(\frac{\mathcal{H}}{\mathcal{E}}\cos^{-1}\epsilon_0\right)\frac{p_\perp^2}{2e\mathcal{H}}+\ldots\ . \tag{7}$$

Integrating (4) and (7) over $p_\perp$ we obtain

$$w(\mathcal{E},\mathcal{H})/w(\mathcal{E},0)=\sigma/\sinh\,\sigma,\quad \sigma=\mathcal{H}\mathcal{E}^{-1}\cos^{-1}\epsilon_0. \tag{8}$$

For nonrelativistic bound states $\epsilon_0=1-\frac{1}{2}\alpha^2\kappa^2\to 1$ ($\alpha=e^2/\hbar c=1/137$, $\kappa\sim 1$). For this reason $\sigma=\alpha\kappa\mathcal{H}/\mathcal{E}$ is identical to the parameter γ introduced in Ref. 3, and Eq. (8) yields the correct expression for the pre-exponential factor $P=\gamma/\sinh\gamma$ in the case of ionization of a negative ion.[4,14] In the other limit, $\epsilon_0=-1$, we have $\sigma=\pi\mathcal{H}/\mathcal{E}$, and Eq. (8) agrees with the first term in the Schwinger expansion[5,6] for the imaginary part of the effective Lagrangian in scalar electrodynamics:

$$w_0(\mathcal{E},\mathcal{H})=\frac{\alpha}{2\pi}\,\mathcal{E}\mathcal{H}[\sinh(\pi\mathcal{H}/\mathcal{E})]^{-1}\exp(-\pi F_{\rm cr}/\mathcal{E}) \tag{9}$$

(if $\mathcal{E},\mathcal{H}\ll F_{\rm cr}$,[a)] then the subsequent terms in this expansion are exponentially small compared with the term (9)).

The ITM makes it possible to obtain an equation of the type (9) for fermions as well. It is only necessary to introduce the spin correction

$$\frac{ie}{2m}\epsilon_{\alpha\beta\mu\nu}\int F^{\alpha\beta}u^\mu s^\nu ds=\frac{e}{m}\int\{(\mathbf{s}\cdot\vec{\mathcal{H}})-(\mathbf{v}\cdot\mathbf{s})(\mathbf{v}\cdot\vec{\mathcal{H}})+(\mathbf{v}\cdot\mathbf{s})\cdot\vec{\mathcal{E}}\}dt$$

to the action. This contribution of this correction as t traverses the loop in Fig. 1c can be calculated by means of the Bargmann–Michel–Telegdi equations[15] for spin $s=1/2$ in an external field. Finally, an equation similar to Eq. (9) but with $(\sinh\sigma)^{-1}$ replaced by $2\coth\sigma$, where $\sigma=\pi\mathcal{H}/\mathcal{E}$, is obtained for $w_{1/2}(\mathcal{E},\mathcal{H})$. This formula determines the prob-

ability of electron–positron pair production from the vacuum in parallel fields (in contrast to Eq. (6), the probabilities w_0 and $w_{1/2}$ refer to the invariant 4-volume $VT=1$ and have dimensions of m^4 or $\mathrm{cm}^{-3}\cdot\mathrm{s}^{-1}$).

c) Let $\vec{\mathcal{E}}\perp\vec{\mathcal{H}}$ and $\rho=\mathcal{E}/\mathcal{H}<1$. This configuration of the fields arises in the rest system of an atom moving in a static magnetic field (Lorentzian ionization[17]). If the velocity v of the atom makes an angle φ with the magnetic field (in the laboratory coordinate system), then

$$\rho=\sqrt{\left(1-\frac{1}{\Gamma^2}\right)\Big/\left(1+\frac{\cot^2\varphi}{\Gamma^2}\right)}=\begin{cases}v_\perp/c, & v\ll c\\ 1-(2\Gamma^2\sin^2\varphi)^{-1}, & \Gamma\gg 1,\end{cases} \tag{10}$$

where $\Gamma=(1-v^2/c^2)^{-1/2}$ is the Lorentz factor. The extremal subbarrier trajectory minimizing Im W is given in parametric form[b)] as

$$x=\frac{im}{e\mathcal{H}}\cdot\frac{a\rho}{(1-\rho^2)^{3/2}}\left(\tau-\frac{\tau_0}{\sinh\tau_0}\sinh\tau\right),\quad y=\frac{m}{e\mathcal{H}}\cdot\frac{a\rho}{1-\rho^2}\cdot\frac{\tau_0}{\sinh\tau_0}$$
$$\times(\cosh\tau_0-\cosh\tau),\quad z=0,\quad t=\frac{im}{e\mathcal{H}}\cdot\frac{a}{(1-\rho^2)^{3/2}}\left(\tau-\rho^2\frac{\tau_0}{\sinh\tau_0}\sinh\tau\right). \tag{11}$$

From Eq. (2) follow equations for the constant a (integral of the motion) and τ_0

$$\frac{\tanh\tau_0}{\tau_0}=\frac{\rho^2 a}{a-(1-\rho^2)\epsilon_0},\quad \cosh\tau_0=\frac{a-(1-\rho^2)\epsilon_0}{\rho\sqrt{a^2+\rho^2-1}}, \tag{12}$$

where the subbarrier motion starts at the time $t_0=(im/e\mathcal{H})\sqrt{1-\rho^2}\,\epsilon_0\tanh\tau_0/[(\tanh\tau_0/\tau_0)-\rho^2]$. The ionization probability is (to exponential accuracy)

$$w\propto\exp\{-F_{\mathrm{cr}}\mathcal{E}^{-1}\Phi(\epsilon_0,\rho)\},\quad \Phi=\rho\tau_0(1-\rho^2)^{-1/2}(1-\epsilon_0 a). \tag{13}$$

Let us discuss some particular cases. In the limit $\epsilon_0\to 1$ it is convenient to switch to atomic units

$$w=\frac{me^4\kappa^2}{2\hbar^3}|A_\kappa|^2\frac{\mathcal{E}}{\mathcal{E}_a}\exp\left\{-\frac{2\kappa^3\mathcal{E}a}{3\mathcal{E}}\left[1+\alpha^2\frac{\kappa^2}{30\mathcal{E}^2}\left(\mathcal{H}^2-\frac{9}{4}\mathcal{E}^2\right)\right]\right\}, \tag{14}$$

which gives the ionization probability for a negative ion taking account of corrections of order α^2. Here $\mathcal{E}_a=\alpha^3 F_{\mathrm{cr}}$ is the electric field intensity in atomic units, $\kappa=\sqrt{E_b/I_H}$, and I_H is the ionization potential of the hydrogen atom. Note the surprisingly high accuracy of this approximation: Even at $E_0=0$ (i.e., for a level whose binding energy equals the rest energy) the error of the expression in the exponential in Eq. (14) equals 2% in the case of an electric field and only 0.2% in the case of crossed fields.

As $\rho\to 0$ (switching off of the electric field) we have

$$w\propto\exp\{-\epsilon_b^2 F_{\mathrm{cr}}\mathcal{H}/\mathcal{E}^2\},\quad \epsilon_b=E_b/m=1-\epsilon_0, \tag{15}$$

where $\mathcal{E}\ll\mathcal{H}\ll F_{\mathrm{cr}}$. Finally, in the case $\rho\to 1$ (crossed fields, i.e., $\mathcal{E}\perp\mathcal{H}$ and $\mathcal{E}=\mathcal{H}$)

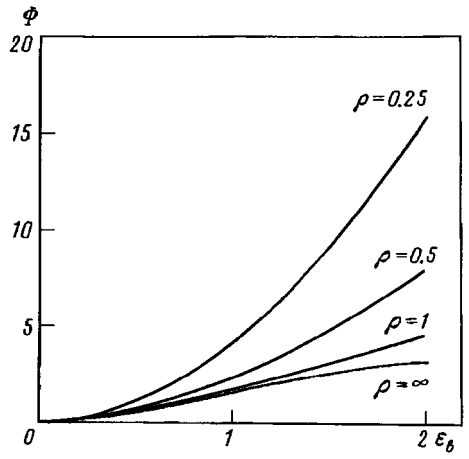

FIG. 2. The function Φ in Eq. (13) plotted versus the binding energy of the level $\epsilon_b=(m-E_0)/m$. The values of the ratio $\rho=\mathcal{E}/\mathcal{H}$ are indicated on the curves.

$$\Phi(\epsilon_0,\rho=1)=2\sqrt{3}\,\frac{\xi^3}{1+\xi^2},\quad \xi=\left[1-\frac{1}{2}\epsilon_0(\sqrt{\epsilon_0^2+8}-\epsilon_0)\right]^{1/2}. \tag{16}$$

Specifically, $w\propto\exp(-9F_{\rm cr}/2\mathcal{E})$ for $\epsilon_0=-1$. In contrast to the probability of pair production from vacuum, which vanishes for crossed fields,[5] here the probability w is nonzero. This is explained by the fact that in the case at hand there is a preferred reference frame (in which the atom is at rest), and the transformation to a Lorentz system, where the field $\mathcal{E}$ can be made as weak as desired, qualitatively alters the formulation of the problem.

For $\mathcal{E}>\mathcal{H}$ the formulas can be derived from Eqs. (11)–(13) by analytical continuation: $(1-\rho^2)^{1/2}\to i(\rho^2-1)^{1/2}$ and $\tau\to i\tau$, the ''time'' t in the subbarrier motion remaining purely imaginary.

The function $\Phi(\epsilon_0,\rho)$ is presented in Fig. 2 for an electric field ($\rho=\infty$), for the the case of crossed fields ($\rho=1$), and also for $\rho=1/2$ and 1/4. A magnetic field (with fixed $\mathcal{E}$) decreases the ionization probability, stabilizing the level. This is easily understood on the basis of the ITM: As $\mathcal{H}$ increases, the subbarrier trajectory ''twists'' and the barrier width increases.

4. The Coulomb interaction appears in (4a) just as in the nonrelativistic case, so that its contribution can be taken into account according to a formula from perturbation theory in the ITM:

$$\delta W=-i\eta\,\ln\,\mu r_1+Z\alpha\int_{t_1}^{0}[\mathbf{r}_0^2(t)]^{-1/2}dt, \tag{17}$$

where $r_1=[\mathbf{r}_0^2(t_1)]^{1/2}$,

$$\eta=Z\alpha\epsilon_0(1-\epsilon_0^2)^{-1/2},\quad \mu=m\sqrt{1-\epsilon_0^2}, \tag{17a}$$

and r_1 is the matching point, which falls out of the final answer. If the extremal subbarrier trajectory $\mathbf{r}_0(t)$ is known analytically (as, for example, in Eq. (1) or (11)), then the calculation of the Coulomb correction reduces to quadratures. For example, the extremal trajectory is obtained from Eq. (1) with $p_\perp = 0$ and $M = m$. Calculating the integral in Eq. (17), we find the Coulomb factor $Q = \exp(-2\ \mathrm{Im}\ \delta W)$

$$Q = [2(1-\epsilon_0^2)^{3/2} F_{\mathrm{cr}}/\mathcal{E}]^{2\eta}\ \exp(2Z\alpha\ \cos^{-1}\epsilon_0), \tag{18}$$

where Z is the charge of the atomic core ($Z=1$ for neutral atoms and $Z=0$ for negative ions; in the latter case $Q=1$).

Multiplying (6) and (18), we obtain the ionization probability in an electric field ($\mathcal{H}=0$). We emphasize that in this case both the exponential factor in w and the Coulomb and pre-exponential factors are determined. Specifically, in the nonrelativistic case

$$w(\mathcal{E},\epsilon_0) = \frac{me^4\kappa^2}{\hbar^3}|A_\kappa|^2\left(\frac{\epsilon}{2}\right)^{1-2\eta} \times \exp\left\{-\frac{2}{3\epsilon}\left[1-\frac{9}{8}\alpha^2\left(\eta\epsilon\ \ln\ \epsilon+\frac{1}{15}+O(\epsilon)\right)\kappa^2+\ldots\right]\right\}, \tag{19}$$

where $\eta = Z/\kappa$ is the Sommerfeld parameter and $\epsilon = \mathcal{E}/\kappa^3\mathcal{E}_a \ll 1$. By analogy with Eq. (14) it can be expected that the domain of applicability of this approximation extends all the way up to $E_b \sim mc^2$.

In the case of fields with a complicated configuration the Coulomb factor can be calculated numerically from Eq. (17). To calculate the pre-exponential factor it is necessary to study a pencil of classical trajectories which are close to the extremal trajectory and to find the quadratic correction to the action W. Examples were given above; see Eq. (5) and (7).

We thank V. V. Vladimirskiĭ and the participants of the theoretical seminar at the Institute of Theoretical and Experimental Physics for a discussion of the results. This work was partially supported by the Russian Fund for Fundamental Research (Project 95-02-05417a).

[a)]This condition is necessary in order for the quasiclassical approximation to be applicable and is certainly satisfied in experiments (for electrons $F_{\mathrm{cr}} = 1.32\cdot 10^{16}$ V/cm or $4.41\cdot 10^{13}$ G).

[b)]Here the parameter τ is proportional to the proper time s of the particle.

[1] A. M. Perelomov, V. S. Popov, and M. V. Terent'ev, Zh. Éksp. Teor. Fiz. **51**, 309 (1966) [Sov. Phys. JETP **24**, 207 (1967)].
[2] V. S. Popov, V. P. Kuznetsov, and A. M. Perelomov, Zh. Éksp. Teor. Fiz. **53**, 331 (1967) [Sov. Phys. JETP **26**, 222 (1968)].
[3] V. S. Popov and A. V. Sergeev, JETP Lett. **63**, 417 (1996).
[4] V. S. Popov, B. M. Karnakov, and V. D. Mur, Phys. Lett. A **225**, (1997).
[5] J. Schwinger, Phys. Rev. **82**, 664 (1951).
[6] J. Schwinger (ed.), *Quantum Electrodynamics*, Dover, New York, 1964.
[7] Yu. N. Demkov and G. F. Drukarev, Zh. Éksp. Teor. Fiz. **47**, 918 (1964) [Sov. Phys. JETP **20**, 614 (1965)].
[8] L. D. Landau and E. M. Lifshitz, *Quantum Mechanics*, Pergamon Press, New York [Russian original, Nauka, Moscow, 1974].
[9] W. Pieper and W. Greiner, Zeits. Phys. **218**, 327 (1969).

[10] V. S. Popov, JETP Lett. **11**, 162 (1970); Yad. Fiz. **12**, 429 (1970) [Sov. J. Nucl. Phys. **14**, 673 (1972)].
[11] Ya. B. Zel'dovich and V. S. Popov, Usp. Fiz. Nauk **105**, 403 (1971) [Sov. Phys. Usp. **12**, 235 (1970)].
[12] W. Greiner, B. Müller, and J. Rafelski, *Quantum Electrodynamics of Strong Fields*, Springer, New York, 1985.
[13] L. D. Landau and E. M. Lifshitz, *The Classical Theory of Fields*, Pergamon Press, New York [Russian original, Nauka, Moscow, 1988].
[14] S. P. Andreev and V. A. Polunin, JETP Lett. **42**, 190 (1985).
[15] V. Bargmann L. Michel, and V. L. Telegdi, Phys. Rev. Lett. **2**, 435 (1959).
[16] M. S. Marinov and V. S. Popov, Yad. Phys. **15**, 1271 (1972) [Sov. J. Nucl. Phys. **15**, 702 (1972).
[17] B. M. Karnakov, V. D. Mur, and V. S. Popov, JETP Lett. **65**, 405 (1997).

Translated by M. E. Alferieff

Resonance enhancement of diffuse scattering of x-rays in a waveguide heterostructure

A. V. Andreev,[a)] Yu. V. Ponomarev, and I. R. Prudnikov
M. V. Lomonosov Moscow State University, 119899 Moscow, Russia

N. N. Salashchenko
Institute of Physics of Microstructures, Russian Academy of Sciences, 603600 Nizhniĭ Novgorod, Russia

(Submitted 9 July 1997)
Pis'ma Zh. Éksp. Teor. Fiz. **66**, No. 4, 219–223 (25 August 1997)

The diffuse scattering of x rays in a four-layer waveguide-type heterostructure is investigated. The dynamic enhancement of diffuse scattering is detected experimentally in regions corresponding to the excitation of waveguide modes for both the incident and scattered waves.
 [S0021-3640(97)00216-8]

PACS numbers: 79.60.Jv, 42.65.Wi, 61.10.Eq

The present letter is devoted to an investigation of the special features of diffuse scattering of x rays in nonperiodic multilayer waveguide-type nanostructures. Resonance enhancement of diffuse scattering in regions corresponding to the excitation of waveguide modes for both the incident and scattered waves was detected experimentally. The effect is of a dynamic nature and is due to the appearance of a standing interference field in the experimental structure. In the region of excitation of the waveguide modes the phase of the interference field depends strongly on the angle of incidence or the scattering angle. This makes possible precise measurements of the statistical characteristics of the roughness of the internal interfaces of the structure.

Diffuse x-ray scattering is an effective method for determining the statistical characteristics of rough surfaces,[1–5] interfaces between amorphous and crystalline films,[4–7] multilayer nanostructures,[8–10] and Langmuir–Blodgett films.[11] Intensive applications of this method in the investigation of multilayer structures began after a theory of coherent diffuse scattering was developed,[12,8,9] showing that the intensity of the scattering as a function of the angle of incidence θ_0 and the scattering angle θ_s contains a series of peaks determined by the condition $\theta_s+\theta_0=2n\theta_B$, where $n=1,2,\ldots$ and $\theta_B=\lambda/2d$ is the Bragg angle (d is the period of the structure). The profile of the peaks, which are known as Bragg surfaces, depends strongly on the statistical and correlation properties of the roughness of the internal interfaces of the structures; this has served as a basis for practical applications of the effect. The theory of coherent diffuse scattering has recently been extended to the case of nonperiodic multilayer structures.[13] In the particular case of waveguide heterostructures, together with the Bragg surfaces there also appear new surfaces of peaks corresponding to the excitation of waveguide modes. In the present work these peaks were observed experimentally and the special features of their excitation were investigated.

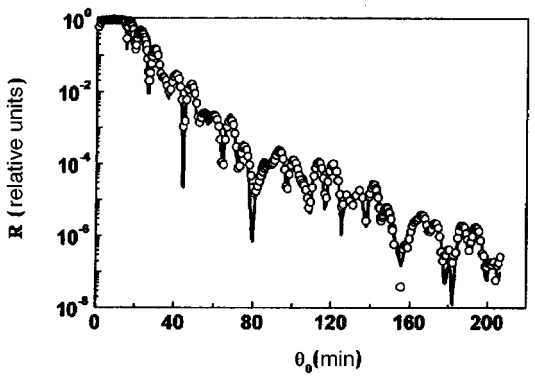

FIG. 1. Experimental (dots) and computed curves of the reflectance R versus the glancing angle.

EXPERIMENTAL PROCEDURE

The four-layer structure, consisting of a sequence of layers of carbon and chromium (Cr/C/Cr/C), was prepared at the Institute of Physics of Microstructures in Nizhniĭ Novgorod by magnetron sputtering on a 25×70 mm glass substrate. According to technological estimates, the layer thicknesses were Cr(100 Å), C(300 Å), Cr(30 Å), and C(100 Å) and the rms height of the surface roughness on the substrate did not exceed 5 Å. The top carbon layer C(100 Å) functioned as a buffer and prevented oxidation of the chromium layer.

The experiment was performed on a double-crystal x-ray spectrometer (1.5 kW x-ray tube with a copper anode, Ge(220) monochromator). The divergence of the monochromatized radiation incident on the sample did not exceed $40''$. The radiation scattered by the sample was detected with a scintillation detector (when recording the rocking curves) and with a position-sensitive x-ray detector (when recording the angular scattering spectra) with a 40×10 mm window and a spatial resolution of 0.2 mm.

EXPERIMENTAL AND NUMERICAL-MODELING RESULTS

Figure 1 displays a specular reflection curve from the experimental heterostructure. The minimum on the curve at an angle of incidence $\theta_0\approx 15'$ is due to excitation of the first waveguide mode in the carbon layer lying between the chromium layers.[14,15] The minimum at $\theta_0\approx 21'$ practically coincides with the critical angle for chromium and reflects the excitation of a quasi-waveguide mode. The subsequent oscillations are produced by the interference of the rays reflected from different interfaces. Numerical modeling of the specular reflection curve yielded the following estimates for the parameters of the heterostructure: $\rho_C=2.3$ g/cm^3, $\rho_{Ni}=7.2$ g/cm^3, SiO_2(/3.9), Cr(103.8/3.9), C(251.4/4.9), Cr(33.4/5.0), and C(109.6/9.1) (the numbers in parentheses are the layer thicknesses d_j and the rms height σ_j of the protuberances on the top boundary of the jth layer, in Å; the enumeration j of the interfaces starts with the substrate, for which $j=0$).

Figure 2a shows a set of angular diffuse scattering spectra obtained for angles of incidence near the first waveguide mode, and Fig. 2b shows the dependence of the intensity of the scattered wave on the angle of incidence for a fixed angle of emergence

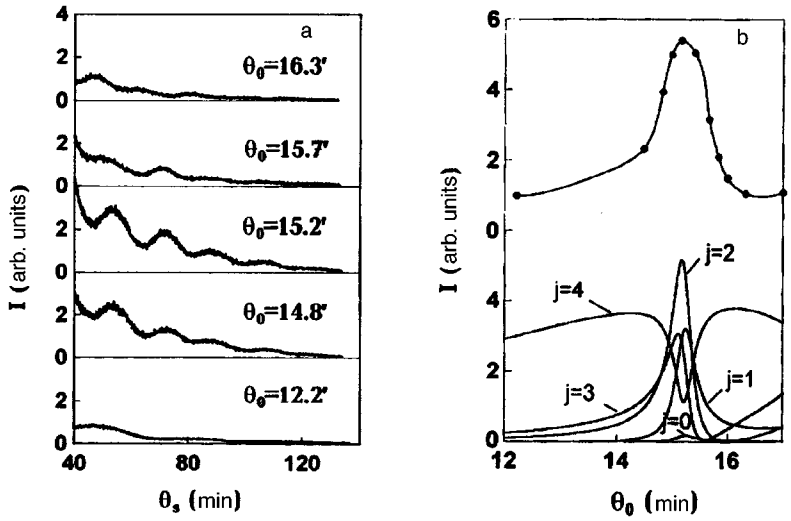

FIG. 2. a — Experimental angular spectra of diffuse scattering. b — Computed intensity of the standing wave field on different interfaces j and the experimentally measured (curve with dots) intensity of diffuse scattering for the angle $\theta_s \approx 40'$ in the region of first waveguide mode.

and the contributions of each interface to the diffuse scattering. Figure 2 demonstrates the enhancement occurring in the diffuse scattering when a waveguide mode is excited. This is due to the formation of a standing wave inside the structure on the incident field,[13] as a result of which the amplitude of the total field increases at the internal boundaries and decreases at the external boundaries (Fig. 2b).

The enhancement of the diffuse scattering is also observed experimentally in the case of excitation of a waveguide mode for the scattered wave. Figure 3 displays the three-dimensional spectra of the intensity of diffuse scattering as a function of the angles θ_0 and θ_s. The peaks in the region $\theta_s < 25'$ appear as a result of the excitation of waveguide ($\theta_s \approx 15'$) and quasi-waveguide ($\theta_s \approx 21'$) modes for the diffusely scattered wave. The enhancement of the diffuse scattering in the region of excitation of the waveguide modes for the scattered wave illustrates the reciprocity principle in electrodynamics[16] (the expression for the amplitude of the wave diffusely scattered in the heterostructure is symmetric with respect to the substitution $\theta_0 \leftrightarrow \theta_s$ (Ref. 13)). In the region of excitation of waveguide modes with respect to the angle of emergence ($\theta_s \approx 15', 21'$) the diffuse waves also form a standing wave. The diffuse scattering from the entire heterostructure depends on the amplitude and phase of this wave at each interface. The peaks in the diffuse scattering at $\theta_s \approx 15', 21'$ (Fig. 3) illustrate the increase in this interference field at the internal interfaces.[13]

The enhancement of diffuse scattering accompanying the excitation of a waveguide mode for the incident ($\theta_0 \approx 15', 21'$) and scattered ($\theta_s \approx 15', 21'$) waves is also seen in the rocking curves shown in Fig. 4 (in the recording of the rocking curve the condition $\theta_0 + \theta_s = 2\theta^* = \text{const}$ holds).

The experiments performed here show that the diffuse scattering by internal inner

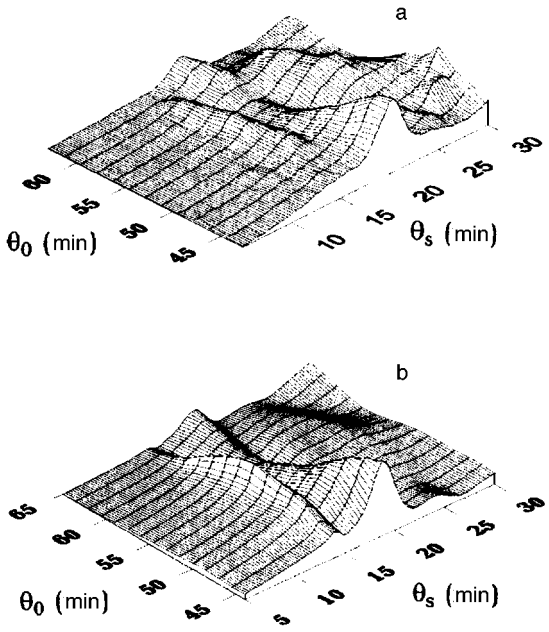

FIG. 3. Experimental (a) and computed (b) three-dimensional angular spectra of the diffuse-scattering intensity.

,surfaces in multilayer structures is extremely sensitive to the phase of the interference field of the standing wave produced in the structure. In contrast to x-ray standing wave methods, which are based on the detection of secondary processes (fluorescence, Auger electrons, and others), diffuse scattering is by its very nature sensitive to the state of the surface. This makes it possible to develop methods for studying the dynamics of surface modification under different external agencies. In investigations of the quality of the

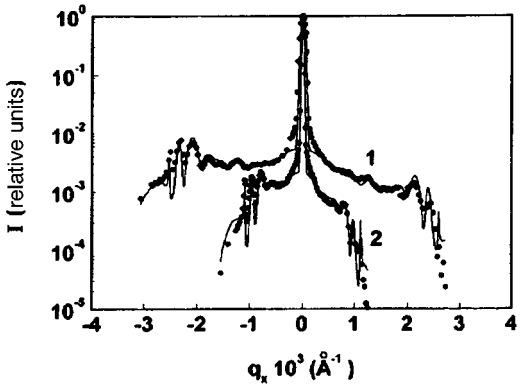

FIG. 4. Experimental (dots) and computed (solid lines) rocking curves as a function of the longitudinal component q_x of the scattering vector $[q_x=(2\pi/\lambda)\cdot(\cos\theta_0-\cos\theta_s)]$. $\theta^*\approx 69'$ (*1*) and $48'$ (*2*).

interfaces in multilayer structures, the excitation of standing waves in a structure makes it possible to distinguish the contributions made by different interfaces to the diffuse scattering. This greatly increases the accuracy of methods used to reconstruct the parameters of structures from the angular spectra of diffuse scattering.

This work was supported by the Russian Fund for Fundamental Research (Project 95-02-05256-a).

[a)]e-mail: andreev@sr.phys.msu.su

---

[1] Y. Yoneda, Phys. Rev. **131**, 2010 (1963).
[2] A. V. Andreev, Usp. Fiz. Nauk **145**, 113 (1985) [Sov. Phys. Usp. **28**, 70 (1985)].
[3] S. K. Sinha, E. B. Sirota, S. Garoff, and H. B. Stanley, Phys. Rev. B **38**, 2297 (1988).
[4] V. M. Sinaĭskiĭ and V. I. Sidenko, Prib. Tekh. Eksp. **6**, 5 (1974).
[5] A. V. Vinogradov, I. A. Brytov, A. Ya. Grudskiĭ *et al.*, *Mirror X-Ray Optics* [in Russian], Nauka, Leningrad, 1989.
[6] S. Dietrich and A. Haase, Phys. Rep. **260**, 1 (1995).
[7] W. Plotz, V. Holy, W. V. D. Hoogenhof, and K. Lischka, J. Phys. III **4**, 1565 (1994).
[8] V. Holy and T. Baumbach, Phys. Rev. B **49**, 10668 (1994).
[9] S. K. Sinha, M. K. Sanyal, S. K. Satiya *et al.*, Physica B **198**, 72 (1994).
[10] A. V. Andreev, Yu. V. Ponomarev, Yu. Ya Platonov, and N. N. Salashchenko, Proc. Soc. Photo-Opt. Instum. Eng. **2801**, 75 (1995).
[11] U. Pietsch, T. Barberka, W. Mahler, and T. H. Metzger, Thin Solid Films **247**, 230 (1994).
[12] A. V. Andreev, A. G. Michette, and A. J. Renwich, J. Mod. Opt. **35**, 1667 (1988).
[13] A. N. Andreev and I. R. Prudnikov, Kristallografiya **41**, 220 (1996) [Crystallogr. Rep. **41**, 203 (1996)].
[14] Y. P. Feng, S. K. Sinha, H. W. Deckmann *et al.*, Phys. Rev. Lett. **71**, 537 (1993).
[15] S. I. Zheludeva, M. V. Koval'chuk, N. N. Novikov *et al.*, Kristallografiya **40**, 145 (1995) [Crystallogr. Rep. **40**, 132 (1995)].
[16] L. D. Landau and E. M. Lifshitz, *Electrodynamics of Continuous Media*, Pergamon Press, New York [Russian original, Nauka, Moscow, 1992].

Translated by M. E. Alferieff

Kinetics of the photoconductivity and absorption in the $D^-(A^+)$ bands in doped silicon

Ya. E. Pokrovskiĭ, O. I. Smirnova, and N. A. Khval'kovskiĭ
Institute of Radio Engineering and Electronics, Russian Academy of Sciences, 103907 Moscow, Russia

(Submitted 15 July 1997)
Pis'ma Zh. Éksp. Teor. Fiz. **66**, No. 4, 224–227 (25 August 1997)

The photoconductivity (PC) spectra and the induced absorption of background radiation in the energy range 10–40 meV are investigated in weakly compensated B-, Ga-, and As-doped silicon at 4.2 K. It is shown that dips corresponding to the photoionization of long-lived excited states of B and As are observed in the PC spectra on the $D^-(A^+)$ bands. It is found that the frequency dependence of the PC spectra corresponds to excitation relaxation times of the order of 10^{-4} s for the states in the $D^-(A^+)$ bands. It is established that in electric fields $E>100$ V/cm the PC decreases sharply, while the induced absorption of the background radiation changes very little. This confirms the conclusion that the excitation of the $D^-(A^+)$ itself makes the main contribution to the PC. © *1997 American Institute of Physics.* [S0021-3640(97)00316-2]

PACS numbers: 61.72.Tt, 72.40.+w, 42.25.Bs

It has been established in a long series of works (see the review in Ref. 1 and the references cited in Ref. 2) that neutral donors and acceptors in silicon, upon trapping nonequilibrium electrons or holes, form stable electrically charged D^- or A^+ states similar to negatively charged hydrogen ions. For relatively high impurity densities $N>10^{16}$ cm^{-3} and weak compensations ($K<10^{-4}$) these states form $D^-(A^+)$ bands, which at low temperatures strongly affect the photoelectric and optical properties of silicon. This influence has also been observed in investigations of long-lived excited states (split off from the ground state by valley–orbit or spin–orbit interactions; see Ref. 3 and references therein) of group-V donors and group-III acceptors in silicon. In the present letter we report the results of investigations of the kinetics of the photoresponse and absorption in heavily doped, weakly compensated ($K<10^{-4}$) silicon in the photon energy range $h\nu=10-40$ meV at 4.2 K.

Figure 1 displays the photoconductivity (PC) spectra, normalized to the photon flux, and the absorption coefficient (k) of silicon doped with boron, gallium, and arsenic. The spectra were recorded while the sample was exposed to intense room-temperature background radiation, screened only by the cold silicon window of the cryostat. This stationary background illumination led to filling of both the $D^-(A^+)$ states and the deep, long-lived excited states of the boron and arsenic impurities. As one can see from Fig. 1, the absorption spectra contain only bands corresponding to the photoionization of the background-filled long-lived excited states of boron and arsenic. In the PC spectra this

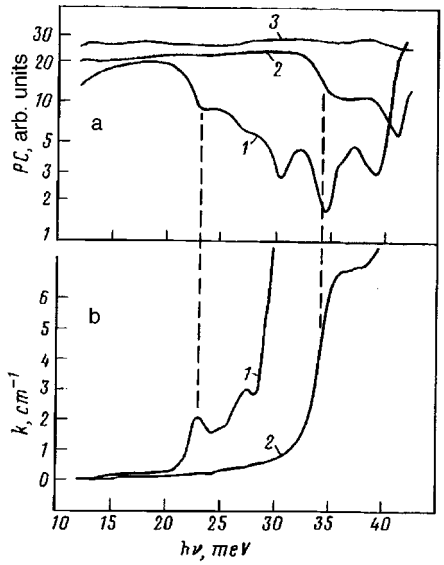

FIG. 1. Spectra of (a) the photoconductivity (PC) of silicon samples doped to density N (cm^{-3}): *1* — B ($3.6\cdot 10^{16}$); *2* — As ($1.2\cdot 10^{17}$); *3* — Ga ($3.6\cdot 10^{16}$), and (b) of the absorption coefficient k in samples *1* and *2*. The dashed lines in the figure correspond to the ionization energies of the long-lived excited states of the B and As impurities.

absorption corresponds to wide dips. Hence it follows that the absorption due to ionization of long-lived excited states is much stronger than the absorption due to photoionization of the $D^-(A^+)$ states. At the same time, the PC in the $D^-(A^+)$ band[2] is stronger than the photoresponse in the energy range corresponding to ionization of the long-lived states. As expected, the analogous features could not be observed in the PC spectra absorption spectra of gallium-doped silicon, since the long-lived excited states of this impurity cannot be filled by free holes excited into the valence band.[3]

The dominance of the $D^-(A^+)$ band photoconductivity is apparently due to the long excitation relaxation times associated with hopping processes.[2] To check this conjecture, we investigated the kinetics of the impurity photoresponse in the region 10–70 meV. Figure 2 displays the PC spectra of boron-doped silicon. These spectra were obtained with different modulation frequencies f of the radiation of the Fourier spectrometer. It is evident that the PC decreases with increasing frequency, and this decrease corresponds to a time constant of the order of 10^{-4} s. We note that no frequency dependence is observed in the energy range corresponding to ionization of the impurity ground state. A similar frequency dependence of the PC is observed in gallium- and arsenic-doped silicon. Under our experimental conditions the spectrometer radiation was much weaker than the steady background illumination. Therefore the frequency dependence of the PC is determined by a change occurring within the $D^-(A^+)$ impurity band itself when the band is photoexcited.

This conclusion is confirmed by comparing the dependence of the PC and the induced absorption[4] on the electric field strength E in the samples. The effect of an electric

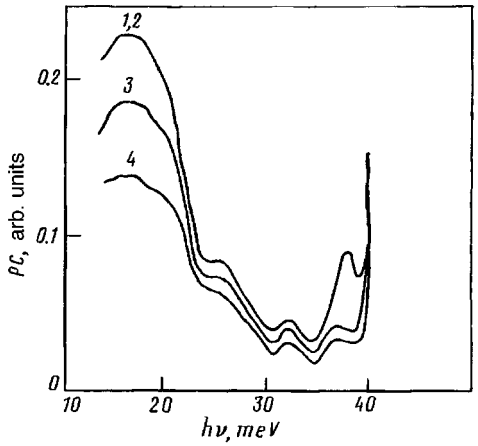

FIG. 2. Photoconductivity spectrum of a boron-doped silicon sample (sample *1*) for different modulation frequencies f (Hz) of the spectrometer radiation: *1* — 170; *2* — 520; *3* — 1050; *4* — 2000.

field on the PC spectra on the A^+ band in boron-doped silicon was investigated in Ref. 2. Similar investigations were performed in the present work. The integrated absorption of the thermal background radiation caused by the photoexcitation of silicon samples by modulated laser radiation with wavelength 3.39 μm ($h\nu = 366$ meV) was investigated.[4] We determined the photoionization cross section for the ground state of boron atoms by photons with this energy to be $3 \cdot 10^{-17}$ cm^2. For this reason, for silicon samples 0.1 cm thick a quite uniform volume excitation was obtained all the way up to $N = 10^{17}$ cm^{-3}. The part of the exciting radiation that was not absorbed in the sample was completely stopped by a polyethylene light filter. The background radiation that passed through the sample and the filter struck a gallium- or antimony-doped germanium photoresistor with a high sensitivity in the energy range 10–40 meV. The variable part of the response V of the photoresistor was proportional to the absorption of the background radiation caused by the excitation of the sample by the modulated laser radiation. The spectrum and the intensity of the background radiation could be changed by placing in front of the sample cooled crystalline or fused quartz filters, which are transparent to the laser beam but are practically nontransmitting for background radiation with photon energies exceeding 40 and 15 meV, respectively.

Figure 3 displays the PC as a function of the electric field intensity E in boron-doped silicon for $h\nu = 20$ meV. In constructing this curve, the photoresponses in different fields at energies corresponding to the photoexcitation of holes from the ground state into the valence band were equalized. The figure also displays the E-dependent induced absorption for the same sample under similar background conditions. One can see from the figure that the absorption varies very little with increasing E. The induced absorption could be due to the modulation of the population of both the long-lived excited state[4] and the A^+ band, both phenomena being characterized by slow relaxation. At the same time the PC drops rapidly with increasing E. The dependence of the PC on E is attributed in Ref. 2 to the delocalization of ionized pairs of impurity atoms A^+–A^- and the change in

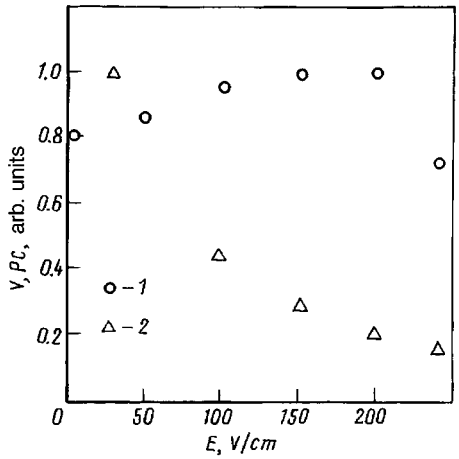

FIG. 3. Curves of the induced absorption V (*1*) and the photoconductivity (*2*) versus the intensity of the electric field E for the B-doped silicon sample *1*.

the effective hopping mobility in the A^+ band. The absence of a strong E-dependence of the absorption in our experiments is not inconsistent with such a conclusion, even if the induced absorption in weakly compensated silicon is due mainly to the A^+ states. Indeed, the ionization probability of the A^+ centers is determined by their density but not by their mobility. The E-dependence of the PC that we observed differs from that established in Ref. 2. This could be due to the different intensity of the background excitation.

The results presented show that in heavily doped, weakly compensated silicon both $D^-(A^+)$ and long-lived excited states of simple donors and acceptors appear simultaneously and their interaction must be taken into account. It is possible that the long-lived excited states play a large role in relaxation processes taking place in the $D^-(A^+)$ bands.[2]

This work was sponsored by the Russian Fund for Fundamental Research (Grant 96-02-16243).

[1] E. M. Gershenzon A. P. Mel'nikov, R. I. Rabinovich, and N. A. Serebryakova, Usp. Fiz. Nauk **132**, 353 (1980) [Sov. Phys. Usp. **23**, 684 (1980)].
[2] A. P. Mel'nikov, Yu. A. Gurevich, L. N. Shestakov, and E. M. Gershenzon, JETP Lett. **63**, 100 (1996).
[3] Ya. E. Pokrovskiĭ, O. I. Smirnova, and N. A. Khval'kovskiĭ, Zh. Éksp. Teor. Fiz. **112**, 221 (1997) [JETP **85**, 121 (1997)].
[4] Ya. E. Pokrovskii, O. I. Smirnova, and N. A. Khvalkovskii, Solid State Commun. **93**, 405 (1995).

Translated by M. E. Alferieff

Degenerate slightly nonideal Bose gas in a parabolic trap

V. A. Alekseev[a)] and D. D. Krylova
P. N. Lebedev Physical Institute, Russian Academy of Sciences, 117924 Moscow, Russia

(Submitted 24 June 1997)
Pis'ma Zh. Éksp. Teor. Fiz. **66**, No. 4, 228–231 (25 August 1997)

The correction to the energy and the number of particles in excited oscillator states is found in the approximation of a pair interaction between the particles at close to zero temperature. It is shown that in the case of the traps used in experiments the gas starts to differ appreciably from an ideal gas when more than $N=1000$ particles are trapped. © *1997 American Institute of Physics.*
[S0021-3640(97)00416-7]

PACS numbers: 71.10.Li, 03.75.Fi

In the Bose–Einstein condensation experiments performed in the last two years, the neutral particles were confined in traps whose potential can be taken as parabolic to a high degree of accuracy.[1–3] In the present letter the energy of such atoms and the maximum number of particles in the oscillator ground state are calculated in the pair-interaction approximation at close to zero temperature using Bogolyubov's method[4,5] for free particles, which simplifies substantially in the case of a parabolic trap.

The Hamiltonian of a system of N particles in the pair-interaction approximation has the form[5]

$$\hat{H}=\sum_s \epsilon(s)a_s^+ a_s+\frac{1}{2}\sum_{s_1,s_2,s_1',s_2'} U_{s_1,s_2}^{s_1',s_2'}\, a_{s_1'}^+ a_{s_2'}^+ a_{s_1} a_{s_2}, \tag{1}$$

where $\epsilon(s)$ is the energy of a discrete state s, measured from the level with the minimum energy $s=0$; a_s^+ and a_s are operators creating and annihilating a particle in the state s; and,

$$U_{s_1,s_2}^{s_1',s_2'}=\langle s_1' s_2'|U(\mathbf{r}_1-\mathbf{r}_2)|s_1 s_2\rangle. \tag{2}$$

In the case of a parabolic trap s is a triple index $\mathbf{s}=(s_x,s_y,s_z)$, and $\Psi_{\mathbf{s}}(\mathbf{r})=\Psi_{s_x}(x)\Psi_{s_y}(y)\Psi_{s_z}(z)$ are the oscillator wave functions

$$\Psi_s(x)=(R\sqrt{\pi}2^s s!)^{-1/2}\exp\left(-\frac{x^2}{2R^2}\right)H_s\left(\frac{x}{R}\right),\quad R=\sqrt{\frac{\hbar}{m\omega}}, \tag{3}$$

where ω is the frequency of the oscillator, m is the mass of the atom, and H_s is a Hermite polynomial.

At low temperatures only the terms in Eq. (1) that are of zeroth and first order in the particle number N need be retained: $\frac{1}{2}U_0 a_0^4$ and $a_0^3(U_s^* a_s^+ + U_s a_s)$, where $a_0=\sqrt{N}$ and $U_s=\langle 00|U|s0\rangle$. Finally, we obtain in place of Eq. (1)

$$\hat{H}=\sum_s \epsilon(s)a_s^+ a_s+\frac{1}{2}N^2U_0+N^{3/2}\sum_{s\neq 0}(U_s^* a_s^+ + U_s a_s). \tag{4}$$

The trivial substitution

$$a_s^+ = b_s^+ - N^{3/2}\frac{U_s}{\epsilon(s)}, \quad a_s = b_s - N^{3/2}\frac{U_s^*}{\epsilon(s)}, \quad s\neq 0, \tag{5}$$

reduces the Hamiltonian (4) to the diagonal form

$$\hat{H}=\frac{1}{2}N^2U_0+\sum_s \epsilon(s)b_s^+ b_s - N^3\sum_{s\neq 0}\frac{|U_s|^2}{\epsilon(s)}. \tag{6}$$

The energy and chemical potential at $T=0$ have the form

$$E_0=\frac{1}{2}N^2U_0-N^3\sum_{s\neq 0}\frac{|U_s|^2}{\epsilon(s)}, \quad \mu=\frac{\partial E_0}{\partial N}=NU_0-3N^2\sum_{s\neq 0}\frac{|U_s|^2}{\epsilon(s)}. \tag{7}$$

The average number of particles in a level $s\neq 0$ equals

$$N_s=\langle a_s^+ a_s\rangle=\left\langle\left(b_s^+ - N^{3/2}\frac{U_s}{\epsilon(s)}\right)\left(b_s - N^{3/2}\frac{U_s^*}{\epsilon(s)}\right)\right\rangle = n_s + N^3\frac{|U_s|^2}{\epsilon^2(s)}, \tag{8}$$

where $n_s=\langle b_s^+ b_s\rangle$ is the average number of quasiparticles determined by the Bose distribution function. At $T=0$ the average number of excited quasiparticles equals zero (i.e., $n_s=0$ for $s\neq 0$) and Eq. (8) implies that there are $N^3\Sigma_{s\neq 0}|U_s|^2/\epsilon^2(s)$ true particles in the excited states, while the number of particles in the ground state is

$$N_0=N\left[1-N^2\sum_{s\neq 0}\frac{|U_s|^2}{\epsilon^2(s)}\right]. \tag{9}$$

In the case of the oscillator eigenfunctions (3) appearing in Eqs. (7) and (9) the sums can be calculated almost exactly. For this, we note first that the ''effective size'' of an oscillator in the case of traps with characteristic frequencies $\omega\sim 100$ s^{-1} and $m=10^{-22}$ g is $R\sim 10^{-3}$ cm, which is certainly much larger than the effective range of the potential $U(\mathbf{r})$. For this reason, the potential U in the matrix elements (2) can be replaced by a δ-function, whereupon $U_\mathbf{s}$ assumes the form

$$U_\mathbf{s}=\sqrt{\frac{2}{\pi}}\hbar\bar{\omega}\frac{a}{\bar{R}}\prod_i (-1)^{n_i}\Omega_i^{1/2}\frac{((2n_i)!)^{1/2}}{2^{2n_i}(n_i)!}, \quad s_i=2n_i, \tag{10}$$

$$U_\mathbf{s}=0, \quad s_i=2n_i+1, \quad n_i=0,1\ldots,$$

where $\bar{\omega}=\sqrt{(\omega_x^2+\omega_y^2+\omega_z^2)/3}$, $\Omega_i=\omega_i/\bar{\omega}$, $\bar{R}=\sqrt{\hbar/m\bar{\omega}}$, and a is the scattering length, which is related to the interaction potential $U(\mathbf{r})$ by the expression[5]

$$\int U(\mathbf{r})d\mathbf{r}=\frac{4\pi\hbar^2}{m}a.$$

Expressing in terms of $\bar{\omega}$ and Ω_i the energy $\epsilon_\mathbf{s}=\hbar\bar{\omega}(\mathbf{s}\cdot\vec{\Omega})$ of the $\mathbf{s}$th oscillator level, we can see that the number of particles in a level $\mathbf{s}\neq 0$ is given by

$$N_{\mathbf{s}}=N^3\frac{1}{2\pi}\left(\frac{a}{\overline{R}}\right)^2\frac{1}{(\vec{\Omega}\cdot\mathbf{n})^2}\prod_i\frac{\Omega_i(2n_i)!}{2^{4n_i}(n_i!)^2},\quad s_i=2n_i, \tag{11}$$

$$N_{\mathbf{s}}=0,\quad s_i=2n_i-1,\quad n_i=1,2,\ldots,$$

i.e., only levels with even s_i are occupied. When expression (10) is substituted in, the sums appearing in Eqs. (7) and (9) become

$$\sum_{\mathbf{n}\neq 0}\frac{|U_{\mathbf{s}}|^2}{\epsilon^{\nu}(\mathbf{s})}=\frac{2^{1-\nu}}{\pi}(\hbar\overline{\omega})^{2-\nu}\left(\frac{a}{\overline{R}}\right)^2 Q_{\nu},\quad \nu=1,2, \tag{12}$$

$$Q_{\nu}=\sum_{\mathbf{n}\neq 0}\frac{1}{(\mathbf{n}\cdot\vec{\Omega})^{\nu}}\prod_{i=1}^{3}\frac{\Omega_i(2n_i)!}{2^{4n_i}(n_i!)^2}.$$

Writing $(\mathbf{n}\cdot\vec{\Omega})^{-\nu}$ as an integral

$$(\mathbf{n}\cdot\vec{\Omega})^{-\nu}=\int_0^{\infty}u^{\nu-1}du\,\exp(-(\mathbf{n}\cdot\vec{\Omega})u),\quad \nu=1,2,$$

and using the value of the sum

$$\sum_{k=0}^{\infty}\frac{t^k(2k)!}{(k!)^2}=(1-4t)^{-1/2},$$

we can perform the summation over n_i in Eq. (12), after which Q_{ν} takes the form

$$Q_{\nu}=\Omega_1\Omega_2\Omega_3\int_0^{\infty}u^{\nu-1}\left[\prod_i\left(1-\frac{1}{4}\exp(-u\Omega_i)\right)^{-1/2}-1\right]du. \tag{13}$$

In the case of an isotropic trap $\overline{\omega}=\omega$, $\Omega_i=1$, $Q_1\approx 0.45$, $Q_2\approx 0.41$, and the expressions for the ground state energy and the number of particles in the ground state at $T=0$ assume the form

$$E_0=\frac{1}{\sqrt{2\pi}}\hbar\omega\frac{a}{R}N^2\left[1-0.36\frac{a}{R}N\right], \tag{14}$$

$$N_0=N\left[1-0.065\left(\frac{a}{R}N\right)^2\right]. \tag{15}$$

The quantity Na/R approximately equals the ratio of the average interaction energy $\overline{E}=(N/R^3)\int U(\mathbf{r})d\mathbf{r}=(N/R^3)(\hbar^2/m)a$ between a single atom and the environment to the energy splitting between the oscillator levels. This explains the appearance of this quantity as an expansion parameter in Eqs. (14) and (15). Naturally, in the approach studied here the number N_0 of particles in the ground state should differ very little from the total number N of particles. It is evident from Eq. (15) that at $T=0$ the relative number of particles in the excited states equals $(N-N_0)/N=0.065(Na/R)^2$. Requiring that this quantity not exceed 0.1, we obtain a criterion under which the atoms in a trap can be treated as an ideal gas: $(Na/R)^2\leqslant 1.5$. Hence it follows that the gas starts to differ from an ideal gas when the particle number $N\geqslant R/a\approx 3000$ ($R\approx 3\cdot 10^{-4}$ cm, $a\approx 10^{-7}$

cm), which is typical for the experiments that have been performed.[1–3] The criterion for the applicability of the pair interaction approximation, $N \ll (R/a)^3 \sim 10^{10}$, holds with a large margin.

As one can see from Eq. (5), the average values $\langle a_s \rangle = -N^{3/2}(U_s^*/\epsilon_s)$ are nonzero. This indicates the formation of a coherent condensate wave function $\Psi = a_0\psi_0 + \Sigma_{s\neq 0}\langle a_s \rangle \psi_s$.

The method employed here to diagonalize the Hamiltonian permits finding the properties of only the stationary states of the system. The metastable states, which drop out of this analysis, were studied in Ref. 6.

This work was supported in part by a grant from the Russian Fund for Fundamental Research (No. 96-02-18695) and the State Science and Technology Program ''Metrologiya.''

[a)]e-mail: valeks@sci.lebedev.ru

---

[1] M. H. Anderson, J. R. Ensher, M. R. Matthews *et al.* Science **269**, 198 (1995).
[2] C. C. Bradley, C. A. Sackett, J. J. Tolett *et al.*, Phys. Rev. Lett. **75**, 1687 (1995).
[3] K. B. Davis, M.-O. Mewes, M. R. Andrews *et al.*,Phys. Rev. Lett. **75**, 3969 (1995).
[4] N. Bogoljubov, J. Phys. (USSR) **11**, 23 (1947).
[5] E. M. Lifshitz and L. P. Pitaevskiĭ, *Statistical Physics, Part II*, Pergamon Press, New York [Russian original, Nauka, Moscow, 1978].
[6] Yu. Kagan, G. V. Shlyapnikov, J. T. M. Walraven, Phys. Rev. Lett. **76**, 2670 (1996).

Translated by M. E. Alferieff

Nature of conduction via impurities in uncompensated silicon

A. P. Mel'nikov, Yu. A. Gurvich, and E. M. Gershenzon
Moscow Pedagogical State University, 119882 Moscow, Russia

L. N. Shestakov
Maritime State University, 163006 Arkhangel'sk, Russia

(Submitted 4 July 1997)
Pis'ma Zh. Éksp. Teor. Fiz. **66**, No. 4, 232–236 (25 August 1997)

The static conductivity $\sigma(E)$ and photoconductivity (PC) at radiation frequencies $\hbar\omega=10$ and 15 meV in Si doped with shallow impurities (density $N=10^{16}-6\times10^{16}$ cm^{-3}, ionization energy $\epsilon_1\simeq45$ meV) with compensation $K=10^{-4}$–10^{-5} in electric fields $E=10$–250 V/cm are measured at liquid-helium temperatures T. Special measures are taken to prevent the high-frequency part of the background radiation ($\hbar\omega>16$ meV) from striking the sample. It is found that the conductivity $\sigma(E)$ is due to carrier motion along the D^- band, which is filled with carriers under the influence of the field E. In fields $E<E_q$ ($E_q\simeq100$–200 V/cm) the carrier motion consists of hops along localized D^- states in a 10–15 meV energy band below the bottom of the free band (energy $\epsilon=\epsilon_1$); for $E>E_q$ carriers drift along localized D^- states with energy $\epsilon\geqslant\epsilon_1-10$ meV. An explanation is proposed for the threshold behavior of the field dependence of the photo- and static conductivities. © *1997 American Institute of Physics.*
[S0021-3640(97)00516-1]

PACS numbers: 61.72.Tt, 72.40.+w

1. According to established ideas, conduction via impurities at liquid-helium temperatures in lightly doped crystal semiconductors with compensations $K\ll1$ is due to hops of electrons (vacancies) along a band of ground states of the impurity (σ_3 conductivity). The properties of this conduction have been studied quite well.[1,2] However, we have observed that in silicon with extremely low compensation ($K\leqslant10^{-4}$) and a density of the main impurity $N=10^{16}$–10^{17} cm^{-3}, an impurity conductivity $\sigma(E)$ with substantially different properties is realized.

For $E<E_q\approx200$ V/cm the observed conductivity ($\sigma(E)=\sigma_M$) increases monotonically with T in the entire temperature range $T=2$–15 K all the way up to the onset of conduction due to ionization of impurities.[3] In this respect it is similar to Mott conductivity with a variable hopping length, $\sigma_M\sim\exp(-T_0/T)^{1/4}$. In the range of fields $E_M<E<E_q$ ($E_M\approx50$ V/cm) σ_M varies with E according to a law close to $\sigma_M\sim\exp\alpha E$ (see Fig. 1, curve *1*). The conductivity σ_M can be several orders of magnitude higher than the expected value of the σ_3 conductivity. (For the sample described below it is estimated that $\sigma_3<10^{-12}$ S/cm.) In Ref. 3 no explanation was found for the σ_M conductivity.

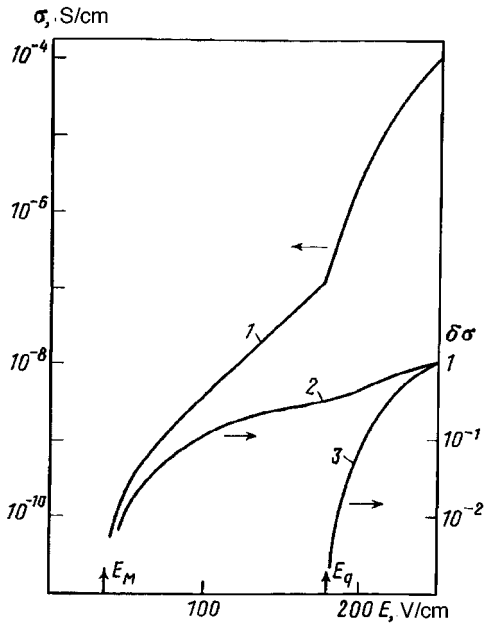

FIG. 1. $\sigma(E)$ — curve *1*, $\delta\sigma_{15}(E)$ — curve *2*, and $\delta\sigma_{10}(E)$ — curve *3* for a Si:B sample ($N=3.6\times10^{16}$ cm^{-3} and $K=5.5\times10^{-5}$) at $T=4.2$ K. The $\delta\sigma_{15}$ and $\delta\sigma_{10}$ curves are normalized to their values at $E=250$ V/cm.

Attempts to attribute σ_M to hops along a band of ground states were unsuccessful.

For $E>E_q$ conductivity of a different type ($\sigma(E)=\sigma_q$; see Fig. 1, curve *1*) appears in a threshold manner.[4] This type of conductivity is characterized by a very sharp dependence on the electric field — quasi-breakdown. In Ref. 4 it was suggested that carrier motion under quasi-breakdown conditions takes place near a transport level ($\epsilon_{\rm tr}$) located in the region of localized states of the D^- band. We underscore that a hopping character of σ_M and σ_q was not established in Refs. 3 and 4.

2. In the present letter we report the results of investigations that make it possible to determine the energy position and nature of the states as well as the character of the carrier motion along these states under conditions of σ_M and σ_q conductivity. The PC at the frequencies of water-vapor laser radiation ($\lambda=80$ and 119 μm or $\hbar\omega=15$ and 10 meV, respectively) was measured. The static conductivity $\sigma(E)$ was measured at the same time.

We call attention to an important feature of our measurements. Background radiation which strikes the sample is inevitably present in PC and absorption experiments. In the experiments performed thus far the background led to filling of the D^- band: Carriers were excited into the free band and trapped in D^- states (see, for example, Ref. 5). In the present work, a system of cold filters that did not transmit radiation with frequency $\hbar\omega>16$–17 meV was placed in front of the sample, and filling of the D^- band under the influence of the background radiation did not occur, i.e., the D^- band was empty at

$E=0$. Under these conditions the static conductivity $\sigma(E)$ was identical to the dark conductivity.

3. The function $\sigma(E)$ for a Si:B sample ($N=3.6\times10^{16}$ cm^{-3}, $K=5.5\times10^{-5}$) at $T=4.2$ K is displayed in Fig. 1 (curve *1*). One can see that $\sigma(E)$ appears in a threshold manner at $E=E_M\approx50$ V/cm. In the region $E_M<E_q$ (≈180 V/cm) the conductivity $\sigma(E)$ increases by approximately a factor of 10^2 according to the law $\sigma_M\sim\exp\alpha E$. These properties as well as the temperature dependence of the conductivity (not presented here) make it possible to identify $\sigma(E)$ for $E<E_q$ with the conductivity σ_M described in Sec. 1. For $E>E_q$ a sharp intensification of the E dependence of the conductivity is observed: Quasi-breakdown arises, and $\sigma(E)=\sigma_q$.

The same figure displays the PC signals (variations of the conductivity) at the frequencies $\hbar\omega=15$ meV (curve *2* — $\delta\sigma_{15}$) and $\hbar\omega=10$ meV (curve *3* — $\delta\sigma_{10}$). Curves *2* and *3* are normalized to their values at $E=250$ V/cm. The PC signal $\delta\sigma_{15}$ appears for $E>E_M$ and $\delta\sigma_{10}$ appears for $E>E_q$. We note that both signals appear in a threshold manner.

4. Let us now discuss the results obtained. We shall first determine the origin of $\delta\sigma_{15}$ and $\delta\sigma_{10}$. The ground states of the impurities (energy $\epsilon=0$) cannot serve as the initial states for these phototransitions. If that were the case, states with energies of 10 and 15 meV would be the final states. These are deep states with very low density in the tail of the D^- band. The probability of such transitions is exponentially small, since the initial and final states are strongly localized and spatially separated. For this reason, they cannot lead to appreciable PC. The $\delta\sigma_{10}$ and $\delta\sigma_{15}$ signals could only be due to transitions into the free band (energy $\epsilon>\epsilon_1\approx45$ meV) from the D^- states. Therefore these signals serve as an indicator of the appearance of carriers in states with $\epsilon>\epsilon_1-15$ meV ≈30 meV and $\epsilon\geqslant\epsilon_1-10$ meV ≈35 meV. Under the experimental conditions (no filling of the D^- states by the background radiation) the appearance of carriers in these states can be due only to the action of E.

The $\delta\sigma_{15}$ and σ_M signals appear at the same field $E=E_M$ (see Fig. 1). The $\delta\sigma_{10}$ signal is absent in this interval $E_M<E<E_q$. This leads to the conclusion that the transport level $\epsilon_{\rm tr}(E)$, near which the carriers determining the conductivity σ_M are found, lies in a band 10–15 meV below the conduction band bottom: 30 meV $<\epsilon_{\rm tr}<35$ meV.

The $\delta\sigma_{10}$ signal appears for fields $E>E_q$. The conductivity σ_q appears at the same field. Hence it follows that σ_q is due to the motion of carriers near the level $\epsilon=\epsilon_{\rm tr}\geqslant35$ meV.

To determine the character of the carrier motion we shall employ the results of spectral measurements of the PC in the range $\hbar\omega=30$–45 meV.[6] It was shown in Ref. 6 that in fields above a critical value a band of delocalized states appears in the D^- band and a mobility threshold $\epsilon_\mu(E)$ arises. As E increases, the delocalization band becomes wider and ϵ_μ shifts sharply downwards in energy right down to $\epsilon=\epsilon_\mu\simeq35$ meV.

Figure 2 (curve *1*) displays the experimental dependence $\epsilon_\mu(E)$ for the sample studied. One can see that the shift of ϵ_μ and the appearance of σ_q and $\delta\sigma_{10}$ take place in the same field $E=E_q=180$ V/cm. This signifies that the conductivity σ_q is due to delocalized states in the D^- band: $\epsilon_{\rm tr}\geqslant\epsilon_\mu$, i.e., this is a drift-type conductivity.

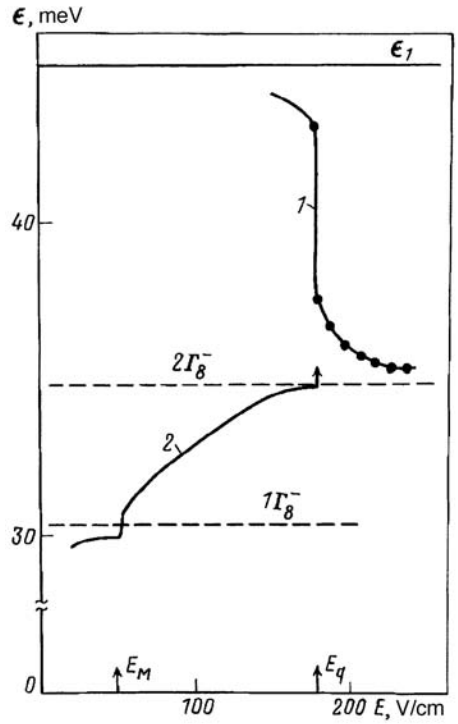

FIG. 2. Curve *1* — $\epsilon_\mu(E)$ for the same sample. Curve *2* — schematic representation of the function $\epsilon_{tr}(E)$. Dashed lines — $1\Gamma_8^-$ and $2\Gamma_8^-$ excited states of boron in silicon.

For $E<E_q$ the threshold ϵ_μ is high or is absent altogether. Therefore, the conductivity σ_M is of a hopping nature.

In summary, the experimental results show that in crystalline silicon with the indicated values of N and K conduction via impurities is due to carrier motion along states in the D^- band. This is a nonequilibrium conduction which arises as a result of the filling of the states in the D^- band by carriers in an electric field. In fields below E_q the conduction is due to hops of carriers along localized states in the D^- band: $\sigma(E)=\sigma_M$. For $E>E_q$ the conductivity is due to drift along delocalized states: $\sigma(E)=\sigma_q$.

At the same time that carriers appear in the D^- band an equal number of vacancies appears in the band of ground states. The σ_3 conductivity increases as well. However, the conductivity that we observed is so high that the contribution of the σ_3 conductivity can certainly be neglected.

5. We shall now discuss another result which we think is interesting — the threshold character of the appearance of σ_M and σ_q and the corresponding PC signals. It is natural to conjecture that the states in the D^- band are filled in a field E by nonactivational hops of carriers along states in the tail of the band which start from the Fermi level $\epsilon=\epsilon_F$. (The presence of a long tail in D^- band was discovered earlier in spectral measurements of absorption in more heavily doped Si specimens.[5]) As E increases, the level ϵ_{tr} shifts

upward; this is indicated by the successive appearance of PC signals. The presence of threshold features indicates that this motion is not continuous. Curve *2* in Fig. 2 shows a schematic plot of the function $\epsilon_{\rm tr}(E)$.

Boron in silicon possesses an $1\Gamma_8^-$ excited state with energy $\approx$30.5 meV. Trapping to this state is an effective recombination channel for nonequilibrium carriers in the D^- band, the energy of the carriers lying near this level. This recombination band apparently retards the upward motion of the level $\epsilon_{\rm tr}$. The threshold nature of the onset of σ_M and the photoresponse $\delta\sigma_{15}$ could be due to a shift of the level $\epsilon_{\rm tr}$ out of this band. The next excited state ($2\Gamma_8^-$) lies at the level $\approx$34.5 meV. In turn, it can result in a threshold effect with higher values of E.

However, for all samples in which the σ_q conductivity is observed, the threshold $E=E_q$ is observed simultaneously with delocalization of the D^- states. This is hardly an accidental coincidence. We shall show below that the filling of the band of delocalized states and hence the appearance of a drift conductivity σ_q should occur abruptly.

The frequency ν of carrier hops is determined by the expression

$$\nu=\nu_0\exp(-2r/a), \tag{1}$$

where r is the hopping distance, a is the localization radius, and ν_0 is a constant. Near ϵ_μ the radius a depends on ϵ:

$$a(\epsilon)\sim a_0\left(\frac{\epsilon_\mu}{\epsilon_\mu-\epsilon}\right)^s, \tag{2}$$

where a_0 is the radius far from ϵ_μ. (The exponent s is estimated to be 0.5–0.6.[1]) When the energy ϵ_i of the initial state is close to ϵ_μ, a hop to a state with a different energy $\epsilon_f\neq\epsilon_i$ ($\epsilon_i,\epsilon_f<\epsilon_\mu$) is a hop between centers with different radii: $a_i\neq a_f$. In this case ν corresponds to an intermediate value of a. However, if a_i and a_f differ by a sufficiently large amount, then the frequency ν is determined by the larger of these two quantities. Roughly speaking, a_i must be used to estimate ν for a downward hop and a_f must be used for an upward hop (this is evident from Eq. (2)). Then

$$\nu_{\rm up}\gg\nu_{\rm down}. \tag{3}$$

In the case at hand, let the top boundary of the carrier distribution at $E=E_q-0$ be located somewhat below 35 meV. A sudden appearance of a mobility threshold ϵ_μ near the 35 meV level (Fig. 2, curve *1*) destroys the balance between the upward and downward hops in the lower neighborhood of the level $\epsilon\approx$35 meV. A sharp restructuring of the carrier distribution occurs: carriers strive to move upward and their density in the region $\epsilon>\epsilon_\mu$ increases until the increasing downward flow restores dynamic equilibrium.

We note that in more strongly compensated specimens under the same conditions neither σ_q nor the threshold ϵ_μ nor the signal $\delta\sigma_{10}$ is observed. This confirms the fact that the mechanism considered above plays an important role: As K increases, the fluctuations of the Coulomb potential increase, the threshold ϵ_μ shifts upward or vanishes altogether, and an abrupt appearance of carriers in states with $\epsilon>$35 meV does not occur. In a certain sense the abrupt appearance of electrons above the mobility threshold can be regarded as an insulator–metal transition induced by an electric field.

This work was supported by the Russian Fund for Fundamental Research (Grant 95-02-06289a).

[1] B. I. Shklovskiĭ and A. L. Éfros, *Electronic Properties of Doped Semiconductors*, Springer-Verlag, New York, 1984 [Russian original, Nauka, Moscow, 1979].
[2] D. I. Aladashvili, Z. A. Adamiya, K. G. Lavdovskiĭ *et al.*, Fiz. Tekh. Poluprovodn. **24**, 234 (1990) [Sov. Phys. Semicond. **24**, 143 (1990)].
[3] E. M. Gershenzon, Yu. A. Gurvich, A. P. Mel'nikov, and L. N. Shestakov, JETP Lett. **51**, 231 (1990).
[4] Yu. A. Gurvich, A. P. Mel'nikov, L. N. Shestakov, and E. M. Gershenzon, JETP Lett. **61**, 730 (1995).
[5] G. A. Thomas, M. Capizzi, F. De Rosa *et al.*, Phys. Rev. **23**, 5472 (1981).
[6] A. P. Mel'nikov, Yu. A. Gurvich, L. N. Shestakov, and E. M. Gershenzon, JETP Lett. **65**, 59 (1997)

Translated by M. E. Alferieff

Structural transformations of the cumulene form of amorphous carbyne at high pressure

T. D. Varfolomeeva, S. V. Popova, A. G. Lyapin, and V. V. Brazhkin
Institute of High-Pressure Physics, Russian Academy of Sciences, 142092 Troitsk Moscow Region, Russia

S. G. Lyapin
Clarendon Laboratory, Physics Department, University of Oxford, Oxford OX1 3PU, England

Yu. P. Kudryavtsev and S. E. Evsyukov
A. N. Nesmeyanov Institute of Elemental–Organic Synthesis, Russian Academy of Sciences, 117813 Moscow, Russia

(Submitted 10 July 1997)
Pis'ma Zh. Éksp. Teor. Fiz. **66**, No. 4, 237–242 (25 August 1997)

Structural transformations of the cumulene form of amorphous carbyne which are induced by heating at high pressure (7.7 GPa) are investigated. These can be described by the sequence amorphous phase – crystal – amorphous phase – disordered graphite. Raman scattering shows that predominately the chain structure of carbyne remains at the first three stages. It was found that the intermediate crystalline phase is an unknown modification of carbon whose structure is identified as cubic ($a=3.145$ Å). A mechanism of structural transformations in carbyne that involves the formation of new covalent bonds between chains is discussed.
[S0021-3640(97)00616-6]

PACS numbers: 61.43.Er

There is now virtually no doubt that, together with the well-known crystalline modifications of carbon, consisting of trivalent (graphite and fullerite) and tetravalent (diamond and lonsdalite) carbon as well as numerous disordered phases with different fractions of atoms in sp^2 and sp^3 states, there exists another allotropic form of carbon – carbyne.[1–3] Carbyne can be synthesized by both chemical and physical methods.[2,3] We are talking about essentially an entire group of crystalline and amorphous structures in which carbon is predominately in a divalent sp state, and in addition there are two types of carbon chains – cumulene (=C=C=C=) with symmetric bonding of the atoms and polyene (–C≡C–C≡). The investigation of carbyne under pressure has been sporadic,[4–6] though even the physical properties of carbyne under normal conditions have not been adequately studied systematically. High pressures are of interest, on the one hand, because of the potential of synthesizing new crystalline phases of carbon and, on the other, because of the possibility of controlling the fractions of atoms in hybridized sp, sp^2, and sp^3 states in carbon structures.

Our objective in the present work was to study the structural transformations in

amorphous cumulene carbyne and to investigate the possibility of synthesizing in a bulk form amorphous carbon with a high fraction of sp^3 states (amorphous diamond) under relatively low pressures ~ 8 GPa easily attainable in a standard apparatus. The possibility of synthesizing the amorphous sp^3 phase of carbon (up to $\sim 80\%$ sp^3 states) exists, for example, in the case when fullerite C60 is heated up to temperatures ~ 500 °C even at $P = 12.5$ GPa.[7] In the course of the investigations it was found, however, that under a pressure of 7.7 GPa a nontrivial sequence of transformations of carbyne is observed in a narrow temperature interval 200–500°C: amorphous phase → crystal → amorphous phase. In addition, the intermediate crystalline phase is a new modification of carbon and can be identified in a cubic system. We report the results of x-ray diffraction and Raman spectroscopy investigations of carbyne specimens obtained after heating under pressure.

The initial amorphous carbyne was synthesized by low-temperature dehydrohalogenization of polyvinylidene chloride.[2,3] The experiments were performed under quasihydrostatic conditions in different modifications of a ''toroid'' type chamber, which were gauged according to transitions in Bi, Sn, and Fe. The samples were heated both with a graphite or Pd heater-container and Ta heaters with an insulating NaCl container. The temperature was measured with a Chromel–Alumel thermocouple. The x-ray measurements were performed by the powder method (Cu $K\alpha$ radiation) and on a DRON-2 diffractometer (Mo $K\alpha$) with a crystal monochromator. The density of the samples was determined by the pycnometric method. The Raman spectra were measured in the backscattering geometry on a Jobin–Yvon T64000 triple spectrometer with a liquid-nitrogen-cooled CCD matrix. The 514.5 nm line of an argon laser was used for excitation. A 10-mW beam was focused to a spot less than 10–20 μm in diameter. Varying the power of laser excitation we did not observe any structural changes in the Raman spectra. Special attention was devoted to monitoring the impurities. This was done by mass spectrometry both before and after synthesis. The total amount of impurities did not exceed 1%; K, Cl, and Si were present in appreciable quantities.

The x-ray diffraction data for carbyne phases obtained under pressure are displayed in Fig. 1. Simple compression of carbyne and heating up to about 200°C have virtually no effect on the structure of the initial carbyne, which is strongly disordered (curve *1*). Heating in the range 200–400°C results in the formation of a new crystalline phase (curve *2*). However, when the temperature is further increased the crystalline reflections vanish (curve *3*), i.e., solid-phase amorphization of a new phase is observed. At high synthesis temperatures ($T_{\text{syn}} \sim 700$–900 °C) structural transformations lead to a phase with a much sharper diffraction pattern (curve *4*). This pattern corresponds to disordered carbon with predominantly sp^2 hybridization of the atoms, i.e., a graphite-like structure. The observed sequence of transformations is statistically reliable (more than 50 specimens were synthesized), and the diffraction data obtained in Mo $K\alpha$ radiation give similar results. Preliminary investigations show that at $P = 12.5$ GPa the pattern of transformations of carbyne remains qualitatively the same; the only change is a shift in the direction of lower temperatures.

The crystalline phase of carbon (Fig. 1, curve *2*) is identified well in the cubic system with lattice parameter $a = 3.145 \pm 0.004$ Å. A careful analysis of the literature and the structural data bases showed that this modification has been unknown thus far. Furthermore, practically all known crystalline forms of carbyne have a hexagonal system,[1–3]

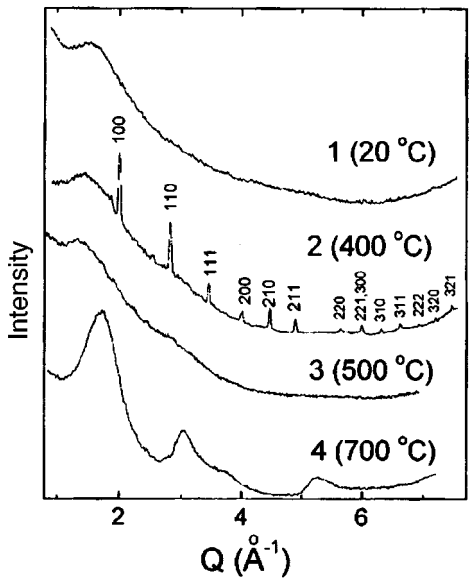

FIG. 1. X-ray diffraction patterns (Cu$K\alpha$) of carbyne after heating under pressure $P=7.7$ GPa followed by quenching. The intensity is displayed as a function of the scattering wave vector $Q=4\pi\sin\theta/\lambda$ (2θ is the scattering angle and λ the radiation wavelength).

corresponding to hexagonal packing of linear chains of different length.[1,8] In the cubic system, there are no extinctions of any reflections in the new phase. This limits the possible symmetry group of the lattice to the following: $P23$, $Pm3$, $P432$, $P\bar{4}3m$, and $Pm3m$. The new phase of carbon is stable both under normal conditions (at least for a few months) and at a higher pressure $P=12.5$ GPa. Increasing the holding time of carbyne at $T_{syn}=400$ °C under pressure from 1 min to 1 h results in a narrowing of the diffraction lines of the crystalline phase. This corresponds to the growth kinetics of crystallites of the new phase.

The Raman scattering spectra corresponding to different stages of the structural evolution of carbyne under pressure are shown in Fig. 2. It was found that the Raman spectra of the compressed initial carbyne, the samples with the new crystalline phase, and the amorphous samples obtained at $T_{syn}\sim 500$–600 °C are very similar. In these spectra a series of wide bands of different intensities is observed (near 460, 640, 1020, 1260, 1390, 1600, 1800, and 2000 cm^{-1}) against the background of strong irregular scattering. This means that the interaction of the neighboring atoms in different phases is of a short-range character, i.e., a predominantly chain structure of the covalent bonds is preserved. The presence of a line near 2000 cm^{-1}, characteristic of fragments of the cumulene chain,[9,10] also confirms this conclusion.

For $T_{syn}\geqslant 700$ °C the Raman scattering spectra change substantially (Fig. 2, curve *4*) and become identical to the spectra of microcrystalline and disordered graphite.[11] In addition, the lines near 1800 and 2000 cm^{-1} vanish. With allowance for the structural data, these changes can be clearly interpreted as a process of graphitization of carbyne,

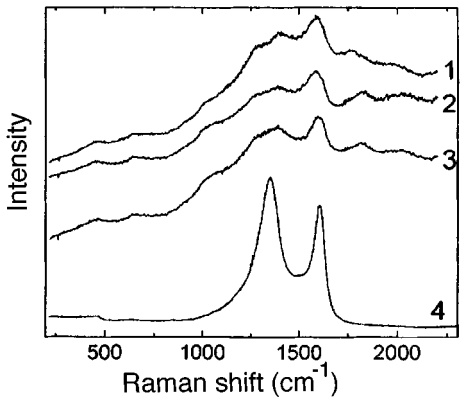

FIG. 2. Raman spectra of phases with structure corresponding to the diffraction curves in Fig. 1 (the numbering of the curves is the same as in Fig. 1).

though the experimental $P-T$ parameters correspond to regions of stability of diamond in the phase diagram. The possible formation of separate diamond-like clusters cannot be ruled out, but higher temperatures and pressures are apparently required in order for carbyne to transform into diamond (see, for example, Ref. 6).

The Raman spectra of the initial carbyne in our case are different from the spectra of cumulene carbyne, which are presented in Ref. 12. This could be due to the different morphology of the interchain covalent-bond cross-links, which are usually present to some extent in carbyne,[1,3] and the fact that the cumulene fragments between cross-links are of different length, as the dynamical analysis in Ref. 9 indicates. On the other hand, the Raman spectra obtained are in qualitatively good agreement with the infrared absorption spectra of cumulene carbyne.[9] Specifically, a minimum of the intensity is observed near 1500 cm^{-1} and the edge of a wide band is observed near 1000 cm^{-1}.

The conclusion that a predominantly chain structure (different from the two-dimensional structure in graphite) is preserved in different phases obtained at synthesis temperatures $T_{syn} \leqslant 600$ °C is confirmed by comparing the macroscopic characteristics of different samples. Their density is close, falling in the range 1.5–1.8 g/cm^3, and they are very soft (softer than graphite) and at the same time very brittle. The experimental values of the density of the specimens with the new crystal phase varied from ≈ 1.6 g/cm^3 for samples obtained after synthesis at $P = 7.7$ GPa up to ≈ 1.8 g/cm^3 for samples obtained after additional compression up to 12.5 GPa. In the case of the new crystalline phase, these values correspond to the filling interval 2.5–2.8 atoms per cubic cell. Each cell most likely contains three atoms. The fact that the cumulene chains (or their fragments) remain in the new crystalline phase imposes serious geometric restrictions on the arrangement of the carbon atoms in a cell, since the double-bond length in carbon molecules and structures varies very little in the range 1.28–1.34 Å, depending on the type of hybridization (sp or sp^2) of the atoms participating in the bond.[13]

An exact identification of the structure of the new cubic phase requires additional investigations, including the observation of electron diffraction from a single crystal. A

careful analysis of the possible cubic lattices enabled us to suggest a model of the structure of the new cubic modification of carbon based on filling of half of the sixfold positions, since the only possible positions of atoms with a multiplicity of three ($\frac{1}{2}00$, $0\frac{1}{2}0$, $00\frac{1}{2}$ or $\frac{1}{2}\frac{1}{2}0$, $\frac{1}{2}0\frac{1}{2}$, $0\frac{1}{2}\frac{1}{2}$) correspond to nearest-neighbor distances which are too large. In this model, a cell with $P23$ symmetry consisting of six atoms with the positions $x00$, $0x0$, $00x$, $\overline{x}00$, $0\overline{x}0$, and $00\overline{x}$ is studied. Choosing $x \approx 0.293$, the distance between the nearest neighbors, both along the edge of a cubic cell (for example, between $x00$ and $1-x.00$) and along the diagonals of the faces (between $x00$ and $0x0$ and so on) is found to be 1.305 Å, which is very close to the bond length in the cumulene chain 1.282 Å.[1] It was found that infinite kinked carbon chains can be packed in such a lattice in an enormous number of different ways, each cell being half-filled on the average. The corresponding structures can be both translationally symmetric and with a disordered packing of the chains. The disordered character of the packing of the chains makes it possible to explain the absence of distinct crystalline features in the Raman spectra and the ease with which such a phase is formed from an amorphous conglomerate of chains. In the model the bond length in a chain 1.305 Å is close to the length of the double bond between atoms in sp and sp^2 states (the length of the $sp=sp$ bond is 1.282 Å, $sp=sp^2$ — 1.310 Å, and $sp^2=sp^2$ — 1.338 Å[13]). This could be due to the existence of covalent cross-links between chains and interaction of π clouds of contiguous atoms in different chains. The appearance of additional cross-links could be one reason for the crystallization of the cubic phase, though the role of van-der-Waals forces between the chains should not be underestimated.

It is surprising that the amorphous phases of carbyne taken before crystallization of the cubic modification ($T_{syn} \leqslant 200$ °C) and after it becomes disordered (500–600 °C) have very similar x-ray diffraction curves and Raman spectra. However, a detailed analy-

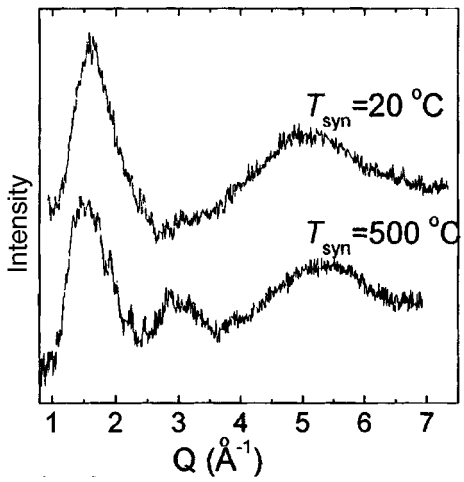

FIG. 3. Interference oscillations of the x-ray scattering intensity for compressed initial carbyne and an amorphous phase obtained by heating. The oscillations were obtained after the average line, approximated by a polynomial, is subtracted out.

sis of the structural data makes it possible to determine the differences (Fig. 3). A peak near 3 $Å^{-1}$ appears in the diffraction curves of the higher-temperature specimens. It is natural to attribute this peak to an increase in the fraction of atoms in the sp^2 state (see Fig. 1, curve *4* for graphite-like carbon). Therefore, the amorphization of the crystalline phase is probably due to the formation of additional cross-links between chains as a result of an increase in the temperature. In this case the length of the individual bonds in a chain should increase, and the lattice as a whole should become disordered and then decompose.

In conclusion, it should be noted that the observed sequence of transformations can apparently be explained by the formation of new covalent bonds, induced by a temperature increase, as well as by the competition between two types of interactions — van der Waals and covalent. Massive graphitization of carbyne occurs at high temperatures. More detailed structural investigations of the new crystalline phase should clarify the mechanism of the transformations occurring in amorphous cumulene carbyne.

We are grateful to N. V. Kalyaeva, R. A. Sadykov, and R. N. Voloshin for assisting in the experiments. This work was sponsored by the Russian Fund for Fundamental Research (Grants 95-02-03677 and 96-02-17328a).

[1] R. B. Heimann, J. Kleiman, and N. M. Salansky, Nature **306**, 164 (1983); Carbon **22**, 147 (1984).
[2] Yu. P. Kudryavtsev, S. E. Evsyukov, M. B. Guseva *et al.*, Izv. Akad. Nauk, Sr. khim. **42**, 450 (1993).
[3] Yu. P. Kudryavtsev, R. B. Heimann, and S. E. Evsyukov, J. Mater. Sci. **31**, 5557 (1996).
[4] V. I. Kasatochkin, L. E. Shterenbeg, M. E. Kazakov *et al.*, Dokl. Akad. Nauk SSSR **209**, 388 (1973).
[5] R. B. Heimann, S. Fujiwara, Y. Kakudate *et al.*, Carbon **33**, 859 (1995).
[6] T. I. Borodina, V. E. Fortov, A. A. Lash *et al.*, J. Appl. Phys. **80**, 3757 (1996).
[7] V. V. Brazhkin, A. G. Lyapin, Yu. V. Antonov *et al.*, JETP Lett. **62**, 350 (1995).
[8] Yu. P. Kudryavtsev, S. E. Evsyukov, and V. G. Babaev, Carbon **30**, 213 (1992).
[9] V. V. Korshak, Yu. P. Kudryavtsev, S. E. Evsyukov *et al.*, Dokl. Akad. Nauk SSSR **298**, 1421 (1988).
[10] J. Kurti, C. Magyar, A. Balazs, and P. Rajczy, Synth. Met. **71**, 1865 (1995).
[11] R. J. Nemanich and S. A. Solin, Phys. Rev. B **20**, 392 (1979).
[12] V. V. Berdyugin, Yu.P. Kudryavtsev, S. E. Evsyukov *et al.*, Dokl. Akad. Nauk SSSR **305**, 362 (1989).
[13] M. J. S. Dewar, *Hyperconjugation*, Ronald, New York, 1962, Chap. 4, p. 11.

Translated by M. E. Alferieff

Some special features of the transition to chaos in the self-modulation of surface spin waves

V. E. Demidov and N. G. Kovshikov
St. Petersburg State Electrical Engineering University, 197376 St. Petersburg, Russia

(Submitted 10 July 1997)
Pis'ma Zh. Éksp. Teor. Fiz. **66**, No. 4, 243–246 (25 August 1997)

The results of experimental investigations of the transition from regular to stochastic self-modulation of intense surface spin waves are presented. It is found that the transition to chaos follows the scenario of a sequence of period-doubling bifurcations. The fractal dimensions and the Kolmogorov entropy are determined for different regimes. The experiments are performed on an apparatus consisting of a microwave oscillator with a spin-wave delay line in the feedback circuit. © *1997 American Institute of Physics.* [S0021-3640(97)00716-0]

PACS numbers: 75.30.Ds, 82.40.Bj

The stochastic behavior of nonlinear systems has been attracting investigators for quite a long time. The development in recent years of a mathematical framework that makes it possible to analyze the results obtained in this field has breathed new life into this problem. The introduction of concepts such as a strange attractor, fractal, fractal dimension, and Kolmogorov entropy (see, for example, Refs. 1 and 2) has made it possible to estimate quantitatively the characteristics of the stochastic behavior of systems.

It is known that the nonlinearity of the response of a spin system to an external microwave magnetic field can result in self-modulation of spin oscillations and waves.[3] The envelope can acquire a chaotic character. These effects were observed and studied in detail in bulk ferrite specimens (see, for example, Refs. 4 and 5). They have also been investigated in thin ferrite films for a number of special cases (see, for example, Refs. 6–8). At the same time, a complete picture of stochastic phenomena in films still does not exist. This is stimulating further investigations of such phenomena with the application of modern mathematical techniques. The objective of the present work is to investigate the transition from regular to chaotic self-modulation of intense surface spin waves in yttrium iron garnet (YIG) films under conditions of a first-order decay instability.

An apparatus consisting of a microwave oscillator with a spin-wave delay line in the feedback circuit was used to investigate the self-modulation processes. The experimental conditions corresponded to the first-order decay instability of spin waves.[9] On account of the low power threshold P_{th} of nonlinear phenomena in ferrite films,[10] the nonlinearity of this system is due to the nonlinearity of the ferrite spin system, and the active element (a Mini-Circuits VNA-25 monolithic amplifier) can be regarded as linear. Epitaxial YIG films ranging in thickness from 10 to 43 μm with a saturation magnetization of 1750 G and a linear dissipation parameter of the order of 0.5 Oe were used in the experiments.

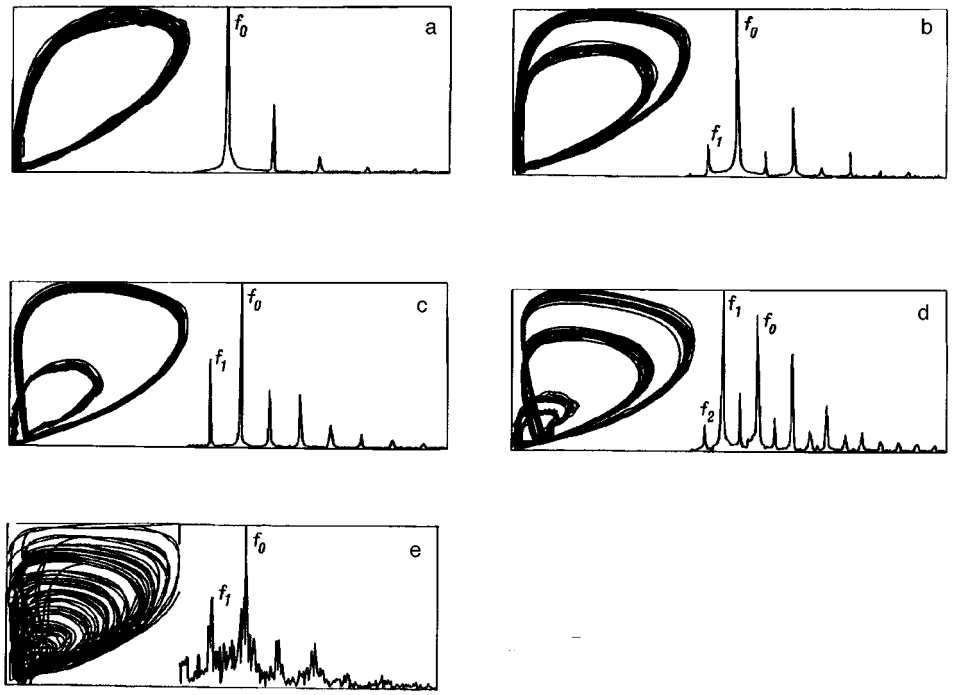

FIG. 1. Projections of attractors and spectra of the modulation signal.

The excitation and detection of surface spin waves propagating under a metallic shield pressed to the surface of the film were accomplished with 30 μm wide microstrip transducers separated by a distance of 10 mm. A model of the delay line was placed in a 540 Oe magnetic field oriented tangent to the surface of the film. The carrying frequency of the oscillations under these conditions was equal to approximately 3250 MHz. The microwave signal power P_{IN} at the entrance of the YIG film was varied with a regulable attenuator connected in series with the delay line. The microwave signal generated by the system was detected in order to distinguish the amplitude-modulation signal and the result was fed to an ADC connected to a computer for further analysis.

The attractors of the system were reconstructed from the time series $U(t)$ obtained. The reconstruction of the phase space was accomplished by the delay method.[11] The components of the d-dimensional vector $\mathbf{x}(t)$ in phase space in this case were obtained by shifting the signal $U(t)$ in time by some delay τ:

$$\mathbf{x}(t)=\{U(t),U(t+\tau),\ldots,U(t+(d-1)\tau)\}.$$

The dimension d of the phase space is called the embedding dimension of the attractor and is determined by the number of degrees of freedom participating in the oscillatory motion.

Figure 1 displays projections of the attractors on the x_1-x_2 plane and the spectra of the initial time series with different powers P_{IN} for a 43 μm thick film. It is evident from

the figure that as the power fed into the system increases, the initially regular modulation evolves into a stochastic modulation. In the case of Fig. 1a, corresponding to $P_{IN}=410$ μW, only one frequency, $f_0=520$ kHz, and its harmonics are observed in the modulation spectrum. After the first period-doubling bifurcation at $P_{IN}=480$ μW (Fig. 1b) a second frequency, $f_1=f_0/2$, appears in the spectrum. As the input power increases further, a redistribution of energy in the spectrum occurs (see Fig. 1c, corresponding to $P_{IN}=600$ μW) and for $P_{IN}=680$ μW a second period-doubling bifurcation occurs (Fig. 1d) with the frequency $f_2=f_0/4$ appearing. When the power level reaches $P_{IN}=750$ μW, sharp stochastization of the attractor occurs (Fig. 1e). The modulation spectrum becomes continuous.

As the process evolves, the fundamental frequency f_0 and the multiple frequencies f_1 and f_2 shift into the high-frequency part of the spectrum by approximately 240 kHz.

The above-described path of the transition to chaos agrees with the universal Feigenbaum scenario,[12] which is partially disrupted by the presence of external noise, as is manifested in the appearance of stochasticity even after only two period-doubling bifurcations.[13]

To analyze the regimes described above, the fractal dimensions D of the attractors, showing the internal arrangement of the set of points of the attractor and the Kolmogorov entropy K, which shows the average rate of loss of information about the system in time, were calculated.[1] A computational procedure based on correlation integrals was used.[14,15] The correlation integral

$$C_d(l)=\lim_{N\to\infty}\frac{1}{N^2}\sum_{i,j}^{N}\theta[l-||\mathbf{x}_i-\mathbf{x}_j||]$$

characterizes the relative number of pairs of points belonging to an attractor which are separated by a distance less than l. Here d is the dimension of the phase space (the embedding dimension of the attractor), N is the number of analyzed points, $\theta(x)$ is the Heaviside step function, and $\|\mathbf{x}\|$ is the norm in phase space. The slope of the curve $\log C_d(\log l)$ in the limit $l\to 0$ equals numerically the correlation dimension of the attractor D_c in the d-dimensional phase space; this dimension is a lower bound on the fractal dimension. The distance between the neighboring curves in the limits $l\to 0$ and $d\to\infty$ divided by the time step τ equals numerically the correlation entropy is a lower bound on the Kolmogorov entropy.

Curves of D versus the embedding dimension d of attractors in different regimes are displayed in Fig. 2a (the numbers on the curves correspond to the number of the regime in Fig. 1). As d increases, the curves saturate, reaching a constant level. The numerical value of this level gives the true fractal dimension, and the value of d for which saturation occurs gives the true embedding dimension of the attractor. It is evident from the figure that $D=1$ in regime *1*, i.e., the attractor consists of a closed trajectory of a limit cycle. Regimes *2–4* are characterized by $D<2$, indicating that the external noise partially disrupts the closure of the trajectories on the attractor. For regime *5* one has $D=2.3$. This attests to the fact that the attractor is topologically a ribbon and possesses the property of mixing of trajectories, which is characteristic of strange attractors.

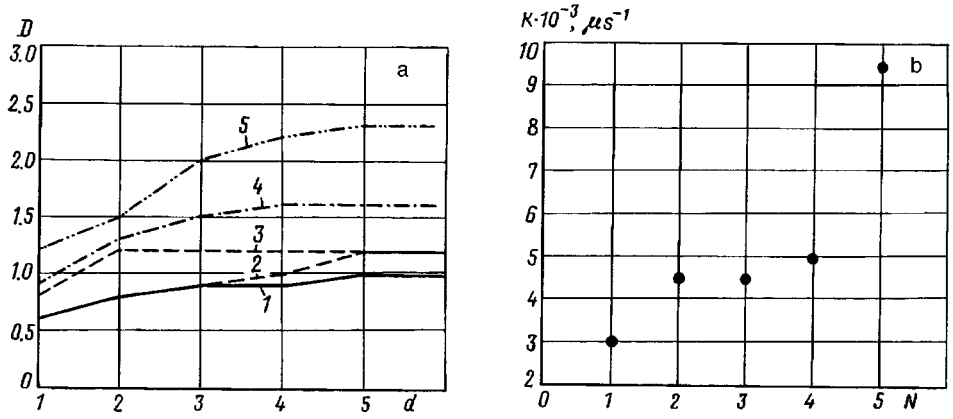

FIG. 2. Curves of the fractal dimension of attractors versus the embedding dimension in different regimes (a) and the Kolmogorov entropy in different regimes (b).

Another fact pointing to the existence of determinate chaos is the sharp jump in the Kolmogorov entropy accompanying the transition to regime *5* (see Fig. 2b). It is known that the Kolmogorov entropy characterizes the rate of divergence of the trajectories of the attractor, i.e., mixing of the trajectories intensifies sharply at a transition to regime *5*.

The results obtained are convincing evidence supporting the existence of determinate chaos in the system investigated. The attractor of the system in phase space is stochastic, which is expressed in the mixing and exponential divergence of the phase trajectories as well as in the fractal structure of the attractor. The computed quantitative characteristics show that the attractor has a low dimension ($D=2.3$), attesting to the small number of active degrees of freedom, i.e., the small number of parametrically coupled spin waves which exchange energy. The transition to chaos follows the model scenario of a sequence of period-doubling bifurcations.

I am deeply grateful to B. A. Kalinikos for a discussion of the results obtained in this work.

This work was sponsored by the Russian Fund for Fundamental Research (Grant 96-02-19515).

[1] G. Shuster, *Deterministic Chaos*, Physik Verlag, Weinheim, 1984 [Russian translation, Mir, Moscow, 1988].
[2] J. Feder, *Fractals*, Plenum Press, New York, 1988 [Russian translation, Mir, Moscow, 1991].
[3] V. S. L'vov, *Nonlinear Spin Waves* [in Russian], Nauka, Moscow, 1987.
[4] A. I. Smirnov, Zh. Éksp. Teor. Fiz. **90**, 385 (1986) [Sov. Phys. JETP **63**, 222 (1986)].
[5] G. Benner, R. Kheĭn, F. Redel'shperger, and G. Vize, Izv. vyssh. uchebn. zaved., ''PND'' **3**, 32 (1995).
[6] B. A. Kalinikos, N. G. Kovshikov, and A. N. Slavin, Zh. Éksp. Teor. Fiz. **94**, 159 (1988) [Sov. Phys. JETP **67**, 303 (1988)].
[7] A. V. Kozhevnikov, Yu. A. Filimonov, G. M. Dudko, and G. T. Kazakov, Pis'ma Zh. Tekh. Fiz. **13**, 736 (1987) [Sov. Tech. Phys. Lett. **13**, 306 (1987)].
[8] G. M. Dudko and A. N. Slavin, Fiz. Tverd. Tela (Leningrad) **31**, 114 (1989) [Sov. Phys. Solid State **31**, 979 (1989)].
[9] A. G. Gurevich and G. A. Melkov, *Magnetic Oscillations and Waves* [in Russian], Nauka, Moscow, 1994.

[10] B. A. Kalinikos, N. G. Kovshikov, and P. A. Kolodin in *Abstracts of Reports at the 2nd All-Union School–Seminar on Spin-Wave Microwave Electronics* [in Russian], Ashkhabad, 1985, p. 77.
[11] F. Takens, *Lecture Notes in Mathematics*, Warwick, Springer-Verlag **898**, 366 (1980).
[12] M. J. Feigenbaum, J. Stat. Phys. **19**, 25 (1978).
[13] A. B. Neĭman, Izv. Vyssh. Uchebn. Zaved. ''PND'' **3**, 8 (1995).
[14] P. Grassberger and I. Procaccia, Phys. Rev. A **28**, 2591 (1983).
[15] P. Grassberger and I. Procaccia, Physica D **9**, 189 (1983).

Translated by M. E. Alferieff

Magnetism and structural phase transitions in $LiTmF_4$ powders

A. V. Klochkov and V. V. Naletov
Kazan State University, 420008 Kazan, Russia

I. R. Mukhamedshin, M. S. Tagirov, and D. A. Tayurskiĭ
Kazan State University, 420008 Kazan, Russia; University of Kanazawa, 920-11 Kanazawa, Japan

H. Suzuki
University of Kanazawa, 920-11 Kanazawa, Japan

(Submitted 19 June 1997; resubmitted 10 July 1997)
Pis'ma Zh. Éksp. Teor. Fiz. **66**, No. 4, 247–250 (25 August 1997)

The field (0–5.5 T) and temperature (2–300 K) dependences of the magnetization of $LiTmF_4$ powders with particle sizes of 1 μm and 56–400 μm are investigated experimentally and theoretically. It is concluded that a transition layer exists between the thulium ions in the bulk and the ions at the surface. Two magnetic-field-induced structural phase transitions are observed at low temperatures, and the temperature dependence of the critical magnetic fields is established. © *1997 American Institute of Physics.* [S0021-3640(97)00816-5]

PACS numbers: 61.43.Gt, 75.30.Kz, 75.60.Ej

The discovery of Tm^{3+} defect paramagnetic centers on the surface of finely dispersed powders of the van Vleck dielectric paramagnet $LiTmF_4$ (Ref. 1) has stimulated further investigation of their magnetic properties. Such investigations are of interest both from the standpoint of gaining a deeper understanding of the nature of the magnetic coupling of the nuclear spins in liquid ^{3}He and the solid-state paramagnetic substrate[2–4] and for determining the possibility of achieving dynamic polarization of the nuclei in liquid ^{3}He through the use of van Vleck paramagnets.[5] In the present work we investigated two types of $LiTmF_4$ powders: finely dispersed powder with characteristic particle size of 1 μm (sample *S*) and powder with large particles (sample *B*) with sizes in the range 56–400 μm. It is known[6] that the magnetic properties of $LiTmF_4$ crystals are highly anisotropic and therefore all experiments were performed on nonoriented powders fixed in Stycast 1266A epoxy resin. This prevented the particles from rotating in high magnetic fields and simplified the averaging procedure in the calculations. The procedure for preparing the powders is described in our early works.[1,3]

The temperature dependence of the magnetization of the samples in the temperature interval 2–300 K and the dependence of the magnetization on the applied magnetic field in the interval 0–5.5 T were measured with a dc-SQUID model MPSM (Quantum Design).

Figure 1 displays the measurement results for the field dependence of the magneti-

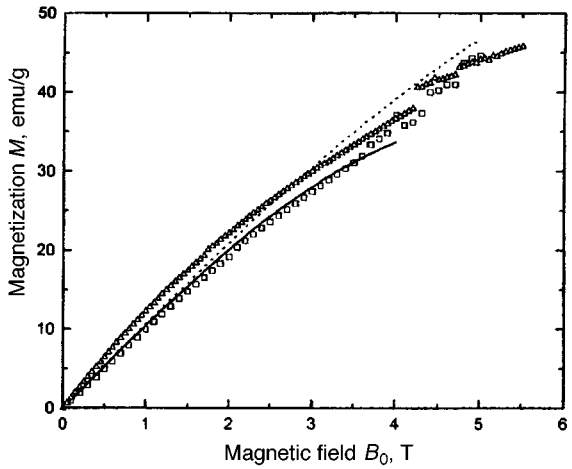

FIG. 1. Field dependence of the magnetization (□ — sample *B*, △ — sample *S*) at $T=2$ K. The dotted line corresponds to the computational results obtained with the Hamiltonian (1); the solid line shows the result obtained with the electron–deformation interactions taken into account (see text).

zation $M(B_0)$ of the *B* and *S* samples as well as the computational results. As one can see from the figure, the magnetization of the sample *B* grows monotonically in fields up to 4 T. This dependence cannot be described even on the basis of exact diagonalization of the Hamiltonian

$$H_0=H_{CEF}+H_Z, \tag{1}$$

where H_{CEF} describes the crystalline electric field and H_Z is the Zeeman interaction with the applied magnetic field (see the dotted line in Fig. 1). This is understandable, considering the strong electron–deformation interaction in $LiTmF_4$ (Ref. 7). Taking this interaction into account in first-order perturbation theory using the parameters from Ref. 8 gives good agreement with experiment (solid line in Fig. 1). The magnetization of sample *S* also grows monotonically in fields up to 4 T. The additional contribution to the total magnetization is clearly seen. However, this contribution cannot be attributed only to the appearance of defect paramagnetic centers Tm^{3+} (Ref. 1). This is confirmed by investigations of the temperature dependence of the magnetization (Fig. 2) in weak magnetic fields ($B_0=10^{-3}$ T). In such weak fields magnetostriction effects can be neglected, so that a calculation for sample *B* using the Hamiltonian (1) gives excellent agreement with experiment (the solid line *1* in Fig. 2). The dotted line represents the computational results obtained for the sample *S* taking account of the Tm^{3+} defect paramagnetic centers ($g=11.6$, $\Delta=0.3$ cm^{-1}, concentration 0.4%).[1] To understand the nature of the additional contribution, it is sufficient to start from a simple precondition. During the preparation of the finely dispersed powder, the crystal structure undergoes distortions in the last layer near the surface of the crystalline particles. The strongest distortions at the surface of the particles result in the formation of Tm^{3+} defect paramagnetic centers, and in a layer near the surface the Stark structure of the Tm^{3+} ions gradually transforms with increasing distance from the surface into a structure characteristic for a single crystal (Fig. 3). Since

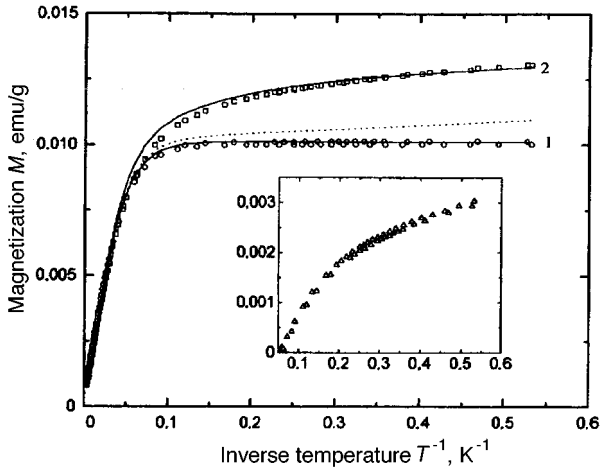

FIG. 2. Temperature dependence of the magnetization (○ — sample *B*, □ — sample *S*). The solid line *1* corresponds to the computational results obtained with the Hamiltonian (1). The dotted line shows the computational results obtained taking account of the defect paramagnetic ions Tm^{3+} (concentration 0.4% relative to the lattice ions). The solid line *2* was obtained by taking account of both the defect paramagnetic centers and the ions with altered Stark structure in the transition layer. Inset: Difference of the magnetizations of samples *B* and *S*.

the total magnetization is measured, it is impossible to obtain detailed information about the local distortions of the crystal field, as was done in the investigation of the optical absorption spectra of Tm^{3+} ions in $LiTmF_4$ with paramagnetic impurities.[9,10] However, even the rough assumption that this transition layer contains one type of Stark spectrum

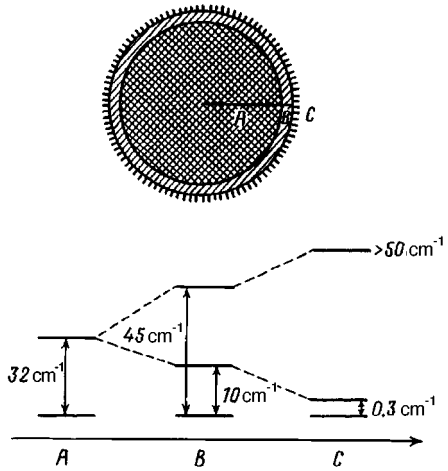

FIG. 3. Arrangement of the lower levels of the Stark structure of Tm^{3+} ions ($^3H_6$ term) in different parts of a crystal particle: ordinary van Vleck ions in the nucleus of the particle (*A*), van Vleck ions in the transition layer (*B*), and paramagnetic ions directly at the surface of the particle (*C*).

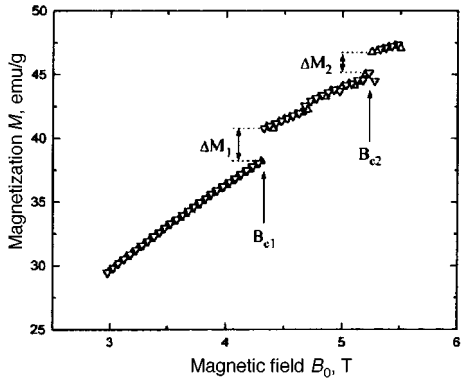

FIG. 4. Example of a magnetic-field-induced structural phase transition in sample S at $T=6$ K.

of the Tm^{3+} ion, with splittings of 10 and 45 cm^{-1} from the main singlet to the sublevels of the doublet split by the distortions of the crystal field instead of 32 cm^{-1} in the undistorted crystal lattice (see Fig. 3), gives fairly good qualitative and quantitative agreement with a physically reasonable number of ions in the transition layer (4% of the total number of thulium ions). The lack of detailed information about the crystal-field parameters and the electron–deformation interaction constants in the transition layer makes it impossible to perform calculations of the field dependence of the magnetization of the sample S.

As one can see from Fig. 1, for both samples some anomalies are observed in the field dependence of the magnetization in high magnetic fields (exceeding 3.7 T). In a more careful investigation of the field dependence of the magnetization in the fields 3–5 T, we observed two jumps in the curve $M(B_0)$ which convincingly attest to structural phase transitions in this material. Figure 4 displays a characteristic example of the measurement of $M(B_0)$ at $T=6$ K. The observed transitions can be characterized by the magnitudes of the magnetization jump ΔM_1 and ΔM_2 as well as the critical fields B_{c1} and B_{c2} in which they occur. The jumps ΔM_1 and ΔM_2 are virtually temperature-independent, while the critical magnetic fields exhibit a pronounced temperature dependence (Fig. 5). Although the existing information is inadequate for drawing definite conclusions about structural phase transitions in $LiTmF_4$, there is no doubt that such transitions do occur, since a magnetic-field-induced structural phase transition due to the cooperative Jahn–Teller effect has already been observed in the van Vleck paramagnet $TmPO_4$ with the initial magnetic properties.[11] Structural transformations in the compound $LiTmF_4$ itself under low hydrostatic pressures were discovered in the ^{169}Tm NMR data and in the ESR of the Er^{3+} impurity ions.[12] It is obvious that a better understanding of the nature of the structural transformations in $LiTmF_4$ as well as information about the two additional equilibrium crystal structures appearing in strong magnetic fields can be obtained only by investigating single-crystal samples by radio spectroscopy methods (ESR of impurity rare-earth ions, Tm^{3+} submillimeter ESR, and ^{19}F NMR) as well as x-ray crystallographic analysis in fields of 4 T at low temperatures.

We thank M. A. Teplov and B. Z. Malkin for their interest in this work, R. Yu.

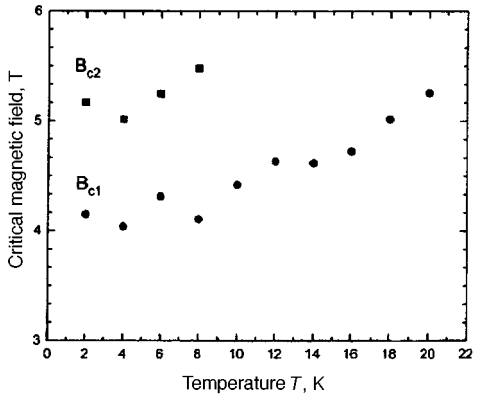

FIG. 5. Temperature dependence of the critical magnetic fields in sample *S*.

Abdulsabirov and S. L. Korableva for growing the crystals, and M. Sekin for assistance in the measurements of the magnetization of the samples.

This work was supported by the Russian Fund for Fundamental Research (Project 97-02-16470) and the Competitive Center at St. Petersburg University (Project 95-0-7.4-133) and as part of a collaboration between Kazan University and the Department of Science at the University of Kanazawa.

[1] A. V. Klochkov, V. V. Naletov, M. S. Tagirov *et al.*, JETP Lett. **62**, 585 (1995).
[2] A. V. Egorov, F. L. Aukhadeev, M. S. Tagirov, and M. A. Teplov, JETP Lett. **39**, 584 (1984).
[3] A. V. Egorov, O. N. Bakharev, A. G. Volodin *et al.*, Zh. Éksp. Teor. Fiz. **97,** 1175 (1990) [Sov. Phys. JETP **70**, 658 (1990)].
[4] V. V. Naletov, M. S. Tagirov, D. A. Tayurskiĭ, and M. A. Teplov, Zh. Éksp. Teor. Fiz. **108,** 577 (1995) [JETP **81**, 311 (1995)].
[5] M. S. Tagirov and D. A. Tayurskiĭ, JETP Lett. **61**, 672 (1995).
[6] A. V. Egorov, M. V. Eremin, M. S. Tagirov, and M. A. Teplov, Zh. Éksp. Teor. Fiz. **77**, 2375 (1979) [Sov. Phys. JETP **50**, 1145 (1979)].
[7] S. A. Al'tshuler, V. I. Krotov, and B. Z. Malkin, JETP Lett. **32**, 214 (1980).
[8] L. K. Aminov, B. Z. Malkin, and V. F. Teplov, in *Handbook on the Physics and Chemistry of Rare Earths*, edited by K. A. Gshneider and L. Eyring, 1996, Vol. 22, Chap. 150.
[9] L. K. Aminov, A. V. Vinokurov, I. N. Kurkin *et al.*, Phys. Status Solidi B **152**, 191 (1989).
[10] L. K. Aminov, B. Z. Malkin, M. A. Koreĭba *et al.*, Opt. spektrosk. **68,** 835 (1990) [Opt. Spectrosc. **68**, 487 (1990)].
[11] B. G. Vekhter, A. Z. Kazeĭ, M. D. Kaplan *et al.*, JETP Lett. **54**, 578 (1991).
[12] R. Yu. Abdulsabirov, I. S. Konov, S. L. Korobleva *et al.*, Zh. Eksp. Teor. Fiz. **76,** 1023 (1979) [Sov. Phys. JETP **49**, 517 (1979)].

Translated by M. E. Alferieff

Specific features of the dielectric spectra of the liquid crystal 5CB in the decimeter wavelength range

B. A. Belyaev, N. A. Drokin, V. F. Shabanov, and V. N. Shepov
L. V. Kirenskiĭ Institute of Physics, Siberian Branch of the Russian Academy of Sciences, 660036 Krasnoyarsk, Russia

(Submitted 14 July 1997)
Pis'ma Zh. Éksp. Teor. Fiz. **66**, No. 4, 251–253 (25 August 1997)

The dispersion and anisotropy of the permittivity of the liquid crystal 5CB in the solid, nematic, and isotropic phases are investigated at frequencies ranging from 50 to 1000 MHz using discretely tunable hybrid microstrip cavities. Resonance features which grow with increasing temperature are observed in the dielectric spectra. It is found that the section of the dispersion which is due to oriented vibrations of the mesophase molecules covers the frequency range almost up to 300 MHz, and the resonances found could be due to conformational vibrations of the molecules. © *1997 American Institute of Physics.* [S0021-3640(97)00916-X]

PACS numbers: 77.84.Nh, 83.70.Jr, 77.22.Ch

The dispersion of the permittivity of liquid crystals is largely due to orientational mechanisms of the polarization of mesophase molecules.[1] The following facts have been established: For nematic liquid crystals (NLCs) the relaxation rates of the rotation of molecules around their short or long axis range from 1 kHz to 10 MHz.[2,3] However, investigations show that the characteristic motions of molecules and the corresponding relaxation rates are much more diverse. Specifically, some relaxation times and their physical interpretation have been obtained using Cole–Cole plots in studies of the dielectric spectra of NLCs over a wide frequency range.[2–4] Measurements of the dielectric characteristics at frequencies above 10 MHz have been performed at only six fixed frequencies.[4]

In the present work we investigated the dielectric permittivity and anisotropy spectra of the liquid crystal 5CB in the frequency range that is most difficult to access experimentally: from 50 to 1000 MHz. The measurements were performed on ring-shaped hybrid microstrip cavities (sensors) with a cell for the experimental material. The cell was fabricated in the form of vertical parallel plates at the antinodes of the rf electric field.[5] A NLC sample was poured into the 100 μm gap between the plates and held there by surface tension forces. Discrete tuning of the frequency of the cavities with a small step was accomplished by connecting miniature calibrated inductive elements into the break in the ring in the region of a current antinode. The measurements were performed in a thermostatic chamber, and the temperature was maintained constant to within 0.1 °C.

The real component ϵ' of the permittivity of the NLC was determined according to the shift of the resonance frequency of the sensor with the sample relative to the empty

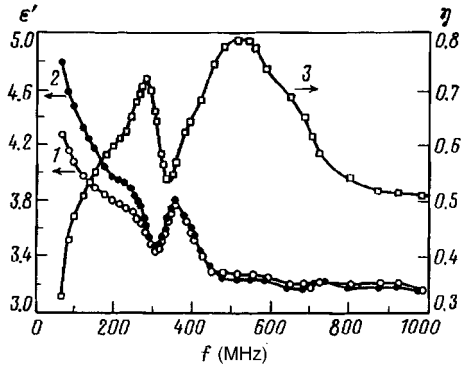

FIG. 1. Frequency dependence of the real components of the permittivity ($\epsilon'_{\parallel}$ — curve *1*, $\epsilon'_{\perp}$ — curve *2*) and of the anisotropy of the dielectric loss (curve *3*) in the nematic phase of the liquid crystal.

sensor. Benzene ($\epsilon=2.28$) was used as the reference material for calibrating the cavities. As a result, the absolute accuracy achieved in determining ϵ' was not lower than 0.02. To measure the anisotropy of the permittivity of the liquid crystal (difference of $\epsilon_{\parallel}$ and $\epsilon_{\perp}$) the sensor with the thermostatic chamber in place was immersed in a static field $H=2200$ Oe generated by an electromagnet. The field oriented the director of the NLC molecules either parallel to or perpendicular to the direction of the rf pump field.

Figure 1 displays the spectra of the real components $\epsilon'_{\parallel}$ and $\epsilon'_{\perp}$ of the permittivity of the experimental liquid crystal (curves *1* and *2*, respectively). The spectra were measured for the ordered nematic phase at temperature $t=20$ °C. One can see that the dispersion of $\epsilon'_{\parallel}$ and $\epsilon'_{\perp}$ is strongest in the range 50–500 MHz. In addition, both curves have a pronounced minimum near 300 MHz and a sharp maximum near 350 MHz. It is also evident that the anisotropy $\epsilon'_{\perp}-\epsilon'_{\parallel}\approx 0.5$ at 50 MHz decreases monotonically with increasing frequency and practically vanishes above 300 MHz.

Figure 1 also displays the frequency dependence of the relative difference of the imaginary components of the permittivity $\eta=(\epsilon''_{\parallel}-\epsilon''_{\perp})/\epsilon''_{\perp}$ (curve *3*), characterizing the anisotropy of dielectric loss in the sample. This curve was constructed according to the change in the intensity of the resonance of the sensor with the sample in place for two orientations of the static magnetic field. In the experiment η was determined with an absolute accuracy of 0.01 or better. One can see that the anisotropy of the dielectric losses has two maxima, near 300 and 500 MHz, separated by a deep minimum near 350 MHz at the location of the maxima of $\epsilon'_{\perp}$ and $\epsilon'_{\parallel}$. It is known[3] that in the crystal under study the anisotropy of the dielectric loss practically vanishes near 10 MHz, where a maximum of ϵ'' due to the resonant vibrational motions of the molecules is observed. However, the experiment shows that even at 50 MHz $\eta\approx 0.3$ and it increases with frequency, reaching a maximum $\eta\approx 0.8$ at 500 MHz, and then decreases monotonically with increasing frequency to $\eta\approx 0.5$ at 1000 MHz.

Figure 2 displays the $\epsilon'_{\perp}$ spectra, measured for three different states of the mesophase of a 5CB crystal — solid ($t=10$ °C), liquid nematic ($t=25$ °C), and liquid isotropic ($t=50$ °C). One can see that the dispersion is strongest for the nematic phase

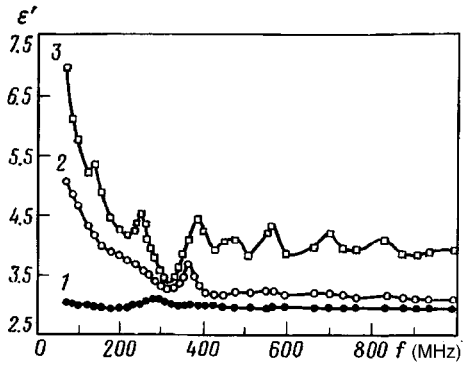

FIG. 2. Frequency dependence of the real component ϵ' of the permittivity of the liquid crystal in the solid phase (curve *1*), the nematic phase (curve *2*), and the isotropic phase (curve *3*).

and the isotropic liquid (curves *2, 3*). There is virtually no dispersion in the solid state in the entire frequency range (curve *1*) with the exception of the region near 300 MHz where a weak dispersion is clearly seen. As the temperature increases, the special features of the dispersion which were observed near 300 MHz intensify, and after the transition into the isotropic liquid an entire series of additional peaks at lower and higher frequencies (curve *3*) appears.

It is interesting to note that as the temperature increases, the component ϵ' of the permittivity increases in the entire frequency range with the exception of a small region near 300 MHz, where it changes very little (see curves *2* and *3*). Experiment shows that the component ϵ'' of the permittivity also increases monotonically with temperature in the entire frequency range. However, at temperatures of phase transitions from the solid state into the nematic phase and from the nematic phase into an isotropic liquid, the dielectric losses increase in small jumps, which are well detected in the intensity of the resonance of the sensor.

Comparing curves *1* and *2* in Fig. 1, one can see that the orientation of the director of the molecules relative to the rf electric field influences the dispersion spectra only at frequencies ranging from 50 to 300 MHz, where a monotonic decrease with $\epsilon'_{\perp}$ and $\epsilon'_{\parallel}$ converging at the same time are observed. It is obvious that this section is a continuation of the high-frequency slope of the dispersion curves resulting from the resonance of the orientational oscillations of the molecules.

The resonance features in the dispersion curves at frequencies above 300 MHz are apparently due to intramolecular conformational motions of flexible molecular fragments.[4] They could lead, specifically, to resonances of the long alkyl chains of the ''tails'' or strongly polar C–N groups.[6] This conclusion is also confirmed by temperature investigations of the permittivities, whence it follows that the high-frequency resonances in the dispersion curves $\epsilon'(f)$ are most pronounced with increasing temperature in the isotropic phase of the NLC. Furthermore, the anisotropy of the dielectric loss, which is so pronounced in the nematic phase, practically vanishes in the isotropic phase of the liquid crystal.

[1] P.-G. de Gennes, *The Physics of Liquid Crystals*, Oxford University Press, New York, 1993 [Russian translation, Mir, Moscow, 1977].
[2] P. G. Cummins, D. A. Dunmur, and D. A. Laidler, Mol. Cryst. Liq. Cryst. **30**, 109 (1975).
[3] H. Mada and A. Nishikawa, Jpn. J. Appl. Phys., Part 2 **32**, Part 2, L1009 (1993).
[4] J. M. Wacrenier, C. Druon, and D. Lippens, Mol. Phys. **43**, 97 (1981).
[5] B. A. Belyaev, N. A. Drokin, and V. N. Shepov, Zh. Tekh. Fiz. **65**, 189 (1985) [Tech. Phys. **40**, 216 (1995)].
[6] I. P. Bazarov and É. V. Gevorkyan, *Statistical Physics of Liquid Crystals* [in Russian], Moscow State University Press, Moscow, 1992.

Translated by M. E. Alferieff

Ferromagnetism of manganese compounds

R.O. Zaĭtsev
Kurchatov Institute Russian Science Center, 123182 Moscow, Russia

(Submitted 15 July 1997)
Pis'ma Zh. Éksp. Teor. Fiz. **66**, No. 4, 254–259 (25 August 1997)

It is shown on the basis of the notion of a strong electron–electron interaction in the unit cell that a ferromagnetic instability is possible in a system with hops between manganese cations and oxygen anions. The phase diagram for the existence of ferromagnetic ordering as a function of the degrees of underfilling n_p and n_t of the $2p^6$ shell of oxygen and the $3t_g^6$ shell of manganese, respectively, is constructed. © *1997 American Institute of Physics.* [S0021-3640(97)01016-5]

PACS numbers: 75.50.Cc

Strong Hubbard repulsion within a unit cell causes a substantial increase in the spin part of the magnetic susceptibility.[1] However, it can be shown[2] that as the electron density increases, the electron–electron scattering amplitude calculated at the Fermi surface decreases, making it impossible for ferromagnetism to arise in the entire domain of applicability of the gas approximation. These arguments, which are confirmed by cluster calculations, actually pertain only to electronic s states with two internal spin degrees of freedom. In the antiferromagnetic compound $La^{3+}Mn^{3+}O_3^{2-}$ the manganese cations are in a trivalent state, so that the manganese possesses two holes in the six-electron t_{2g} shell.

The manganese ions in the antiferromagnetic compound $Ca^{2+}Mn^{4+}O_3^{2-}$ are in a tetravalent state. This corresponds to the presence of three holes in the t_{2g}^6 shell.[3]

Denoting the number of holes in the t_{2g}^6 shell of Mn by n_t and the number of holes in the $2p^6$ shell of the oxygen anions O^{2-} by n_p, the condition of electrical neutrality for the compound $La_{(1-x)}^{3+}Me_x^{2+}MnO_3$ can be expressed in form

$$n_t+3n_p=x+2. \tag{1}$$

Here $x<1$ is the concentration of divalent group-II metallic substituent ions Me (Ca, Sr, Ba).

As the number n_p of oxygen holes varies from 0 to 1, the number of holes at the cations varies from 3 to 0.

1. STATEMENT OF THE PROBLEM AND GENERAL RELATIONS

In compounds with the perovskite structure, the most probable hops are those which occur between the cations of the transition element located at the center of a simple cubic unit cell and the closest oxygen anions located at the centers of the faces.

We shall assume that the hops occur without a change in the spin projection, so that the Hamiltonian is determined by a single hopping integral $t(\mathbf{r})$

$$\hat{H}=\sum_{\mathbf{r},\mathbf{r}',\sigma,\eta,\nu} t(\mathbf{r}-\mathbf{r}')[\hat{d}^{+}_{\mathbf{r},\sigma,\eta}\hat{p}_{\mathbf{r},'\sigma,\nu}+\text{ h.c.}]+\sum_{\mathbf{r},\sigma,\eta}[\epsilon_d-\sigma H]\hat{d}^{+}_{\mathbf{r},\sigma,\eta}\hat{d}_{\mathbf{r},\sigma,\eta}$$

$$+\sum_{\mathbf{r},\sigma,\nu}[\epsilon_p-\sigma H]\hat{p}^{+}_{\mathbf{r},\sigma,\nu}\hat{p}_{\mathbf{r},\sigma,\nu}. \tag{2}$$

Here, μ is the chemical potential, $\sigma=\pm$ is the spin index, H is the external magnetic field, the crystal index λ assumes three values ($\eta=xy$, yz, zx) when the t_{2g} shell is filled and three values ($\nu=x$, y,z) when the p shell is filled.

In compounds of the perovskite type (La, Me)MnO_3 the threefold degenerate states of the manganese cations overlap with the three oxygen anions, each of which is triply degenerate.

In the very simple approximation employed each state of the manganese cation overlaps independently with two p states of the four nearest oxygen anions. Accordingly, the equations for the single-particle Green's function decouple into three independent equations.

The Hubbard energy for both manganese and oxygen is the largest energy parameter. For this reason, to simplify the calculations we shall assume it to be infinite.[4]

Under this assumption the problem must be solved separately for each integer interval of variation of the variable n_t.

According to the electrical-neutrality condition (1), the analysis must be confined to the range of values of the variable n_p from 0 to 1.

The experimental data show that the manganese cations in the compound (La, Ca)MnO_3 possess a positive charge between $+3$ and $+4$. Hence we conclude that in this compound the d-electron states of manganese resonate between $3d^3$ and $3d^4$ states. According to the electrical-neutrality condition (1), in the hole approximation these states correspond to the range $2<n_t<3$, where resonance between the two- and three-particle t_{2g} states occurs.

For this reason we shall examine the case $2<n_t<3$ in detail.

2. THE INTERVAL $2<n_t<3$

The lowest three-particle state possesses spin $S=3/2$ and is quadruply spin-degenerate:

$$\hat{a}^{+}_{\sigma}\hat{b}^{+}_{\sigma}\hat{c}^{+}_{\sigma}|\rangle,\quad S_z=3\sigma/2;$$

$$\frac{1}{\sqrt{3}}(\hat{a}^{+}_{\bar{\sigma}}\hat{b}^{+}_{\sigma}\hat{c}^{+}_{\sigma}|\rangle+\hat{a}^{+}_{\sigma}\hat{b}^{+}_{\bar{\sigma}}\hat{c}^{+}_{\sigma}|\rangle+\hat{a}^{+}_{\sigma}\hat{b}^{+}_{\sigma}\hat{c}^{+}_{\bar{\sigma}}|\rangle),\quad S_z=\sigma/2. \tag{3}$$

We shall construct the nine spin-1 two-particle states from the three different products of the pair creation operators. The two-particle states $^3A_2$ with the lowest energy possess spin $S=1$:

$$\hat{a}_\sigma^+\hat{b}_\sigma^+|0\rangle,\ (S_z=\sigma);\quad \frac{\hat{a}_\uparrow^+\hat{b}_\downarrow^+ + \hat{a}_\downarrow^+\hat{b}_\uparrow^+}{\sqrt{2}}|0\rangle,\ (S_z=0). \tag{4}$$

We find the six remaining two-particle states by means of the cyclic transformation $a\to b\to c\to a$. The highest-energy states ${}^1E$ and ${}^1A_1$ are neglected.

The decomposition of the transition between the two- and three-particle states with the lowest energy in terms of the X operators is determined by three genealogical coefficients:

$$\hat{a}_{\mathbf{r}\sigma}=\hat{X}_{\mathbf{r}}^{(0,\sigma,\sigma|3\sigma/2)}+\sqrt{\frac{2}{3}}\,\hat{X}_{\mathbf{r}}^{(A(yz,xz)|\sigma/2)}+\frac{1}{\sqrt{3}}\,\hat{X}_{\mathbf{r}}^{(0,\overline{\sigma,\sigma|\sigma/2})}. \tag{5}$$

We obtain the decomposition of the two other annihilation operators from Eq. (5) by means of the cyclic permutation operation.

In the absence of a field all average occupation numbers and the terminal factors f_t (Ref. 5) can be expressed in terms of n_t — the average number of electrons per cell. Taking account of the degeneracy we obtain

$$3n_{II}+4n_{III}=1,\quad 18n_{II}+12n_{III}=n_t,\quad f_t=\frac{5n_t-6}{36}. \tag{6}$$

To find the equation of state for $H=0$ we express the occupation numbers of the three-particle states in terms of the single-particle Green's function at the coinciding points. Summing over the spin index we obtain

$$n_t=2+4f_tK_0;\quad n_p=2f_pP_0. \tag{7}$$

Here $f_p=(6-5n_p)/6$, $n_F(\epsilon)$ is the Fermi distribution, and the sums K_0 and P_0 can be expressed in terms of the normal coordinates $a_p^{(\pm)}$ and the excitation spectrum $\xi_p^{(\pm)}$ (defined in Eq. (17)):

$$K_0=\sum_{\mathbf{p},\lambda=\pm}a_{\mathbf{p}}^{(-\lambda)}n_F(\xi_{\mathbf{p}}^{(\lambda)}),\quad P_0=2n_F(\epsilon_p)+\sum_{\mathbf{p},\lambda=\pm}a_{\mathbf{p}}^{(\lambda)}n_F(\xi_{\mathbf{p}}^{(\lambda)}). \tag{8}$$

The equations for the variations of the three-particle occupation numbers $\delta n_{III}^{(3\sigma/2)}$ and $\delta n_{III}^{(\sigma/2)}=-\delta n_{III}^{(-\sigma/2)}$ can be obtained from the general equation for the average value of the T-products of the annihilation operator (5) by a linear combination of three conjugate operators with arbitrary coefficients β_s:

$$b_1\beta_1 n_{III}^{(3\sigma/2)}+b_2\beta_2 n_{III}^{(\sigma/2)}+b_3\beta_3 n_{III}^{(-\sigma/2)}=T\sum_{1\leqslant k,n\leqslant 3}\sum_{\omega,\mathbf{p}}b_kG_\omega^{k,n}(\mathbf{p})\beta_n f_n. \tag{9}$$

In the simplest variant of the self-consistent field approximation (Hubbard-I approximation[6]) the matrix elements of the single-particle Green's function are determined in terms of the inverse Green's function for the zeroth approximation:

$$\hat{G}_{\omega}^{-1}(\mathbf{p})=\begin{pmatrix} (i\omega-\epsilon_k)\delta_{k,n}; & -b_k f_k \nu_x; & -b_k f_k \nu_y \\ -f_p \nu_x^* b_n; & i\omega-\epsilon_p; & 0 \\ -f_p \nu_y^* b_n; & 0; & i\omega-\epsilon_p; \end{pmatrix}, \tag{10}$$

where $\nu_s=t[1-\exp(ip_s)]$, $b_1=1$, $b_2=\sqrt{2/3}$, and $b_3=\sqrt{1/3}$.

Varying the equation (9) we obtain

$$b_1\beta_1\delta n_{III}^{(3/2)}+b_2\beta_2\delta n_{III}^{(1/2)}+b_3\beta_3\delta n_{III}^{(-1/2)}$$
$$=K_0[b_1\beta_1\delta f_1+b_2\beta_2\delta f_2+b_3\beta_3\delta f_3]+(\mathbf{b}\cdot\vec{\beta})f\delta G, \tag{11}$$

where K_0 is determined in terms of the equation of state (7): $K_0=9(n_t-2)/(5n_t-6)$.

If the vector $\vec{\beta}$ is assumed to be orthogonal to the vector $\mathbf{b}$, i.e., $\Sigma_{1\leqslant k\leqslant 3}b_k\beta_k=0$, then two relations that do not depend explicitly on the variations of the magnetic field can be obtained. We find the first equation with the conditions $b_3\beta_3=b_1\beta_1$ and $b_2\beta_2=-2b_1\beta_1$

$$\delta n_{III}^{(3/2)}=3\,\delta n_{III}^{(1/2)}. \tag{12}$$

Setting $\beta_2=0$ and $b_3\beta_3=-b_1\beta_1$ we obtain a second equation

$$(1-K_0)(\delta n_{III}^{(3/2)}+\delta n_{III}^{(1/2)})-2K_0\delta n_{II}=0. \tag{13}$$

The variations of the terminal factors can be expressed in terms of the variations of the occupation numbers

$$\delta f_1=\delta n_{III}^{(3/2)}+\delta n_{II},\quad \delta f_2=\delta n_{III}^{(1/2)},\quad \delta f_3=\delta n_{III}^{(-1/2)}-\delta n_{II}.$$

Using the additional condition $\delta n_{III}^{(-1/2)}=-\delta n_{III}^{(1/2)}$ we find the inverse relations

$$\delta n_{III}^{(3/2)}=\delta f_1+\delta f_2+\delta f_3,\quad \delta n_{III}^{(1/2)}=\delta f_2;\quad \delta n_{II}=-\delta f_2-\delta f_3. \tag{14}$$

We obtain a third equation by setting $\beta_k=b_k$. Variation of the virtual Green's function δG gives three types of terms

$$b_1^2\delta n_{III}^{(3\sigma/2)}+b_2^2\delta n_{III}^{(\sigma/2)}+b_3^2\delta n_{III}^{(-\sigma/2)}$$
$$=[K_0+L_d]\sum_{k=1,2,3}b_k^2\delta f_k^{(\sigma)}+b^2\frac{f_d}{f_p}L_d\delta f_p-b^2 f_d D_0\sigma\delta H, \tag{15}$$

where the coefficients L_d and D_0 are defined as follows:

$$L_d=\sum_{\mathbf{p},\lambda=\pm}\left\{\frac{\delta}{\delta t_{\mathbf{p}}^2}[t_{\mathbf{p}}^2 n_F(\xi_{\mathbf{p}}^{(\lambda)})a_{\mathbf{p}}^{(-\lambda)}]\right\}-K_0,\quad D_0=\sum_{\mathbf{p},\lambda=\pm}a_{\mathbf{p}}^{(-\lambda)}n_F'(\xi_{\mathbf{p}}^{(\lambda)}). \tag{16}$$

These coefficients were obtained using the explicit form of the energy spectrum and the normal coordinates

$$\xi_{\vec{p}}^{(\pm)}=\pm\sqrt{\frac{r^2}{4}+b^2 f_t f_p t_{\mathbf{p}}^2}-\mu;\quad a_{\mathbf{p}}^{(\pm)}=\frac{1}{2}\left[1\pm\frac{r}{\sqrt{r^2+4b^2 f_t f_p t_{\mathbf{p}}^2}}\right]. \tag{17}$$

Finally, we obtain the following equations for the coefficients as a function of the position of the Fermi level:

$$\mu = -\frac{\epsilon_p + \epsilon_d}{2}; \quad r = \epsilon_p - \epsilon_d; \quad b^2 = 2; \quad t_{\mathbf{p}}^2 = t^2[2 - \cos(p_x) - \cos(p_y)]. \tag{18}$$

The equation determining the variation of n_p has a form similar to expression (15)

$$\delta n_p^{(\sigma)} = 3\,\delta f_p^{(\sigma)} = L_p \frac{f_p}{b^2 f_d} \sum_{k=1,2,3} b_k^2 \delta f_k^{(\sigma)} + [P_0 + L_p]\delta f_p - f_p R_0 \sigma \delta H. \tag{19}$$

All coefficients are calculated with a zero magnetic field

$$L_p = \sum_{\mathbf{p},\lambda=\pm} \left\{ \frac{\delta}{\delta t_{\mathbf{p}}^2} [t_{\mathbf{p}}^2 n_F(\xi_{\mathbf{p}}^{(\lambda)}) a_{\mathbf{p}}^{(\lambda)}] \right\} - P_0 + 2n_F(\epsilon_p),$$

$$P_0 = 3\frac{n_p}{6 - 5n_p}; \quad R_0 = 2n_F'(\epsilon_p) + \sum_{\mathbf{p},\lambda=\pm} a_{\mathbf{p}}^{(\lambda)} n_F'(\xi_{\mathbf{p}}^{(\lambda)}). \tag{20}$$

Thus we have a system of four equations whence we find the condition for the appearance of ferromagnetism:

$$\det \begin{pmatrix} 1 - b_1^2(K_0 + L_d) & 4/3 - b_2^2(K_0 + L_d) & 1 - b_3^2(K_0 + L_d) & -b^2 f_d L_d / f_p \\ -1 & +2 & -1 & 0 \\ 1 - K_0 & 2 & 1 + K_0 & 0 \\ -b_1^2 f_p L_p / b^2 f_d & -b_2^2 f_d L_p / b^2 f_d & -b_3^2 f_p / b^2 f_d & 3 - P_0 - L_p \end{pmatrix} = 0.$$

The calculation of the determinant gives the condition

$$(3 - P_0)[3K_0(1 - K_0) - L_d(2 + 3K_0)] - 3L_p K_0(1 - K_0) = 0. \tag{21}$$

The explicit values of the genealogical coefficients were substituted here:

$$b_1^2 = 1; \quad b_2^2 = 2/3; \quad b_3^2 = 1/3; \quad b^2 = 2.$$

3. THE INTERVAL $1 < n_t < 2$

Let us examine the situation when the t_{2g} states resonate between one- and two-hole states, while the number of $2p$ holes in the oxygen $2p^6$ shell is once again less than 1 ($n_p < 1$). The occupation numbers n_t vary from 1 to 2. The single-particle states $\hat{a}_\sigma^+|0\rangle$, $\hat{b}_\sigma^+|0\rangle$, and $\hat{c}_\sigma^+|0\rangle$ possess spin 1/2. The lowest-energy two-particle states $^3A_2$ possess spin $S = 1$ and are determined by relations (4). Repeating the calculations performed in the previous section, we obtain the condition for the appearance of ferromagnetism:

$$(3 - P_0)[K_0(1 - K_0) - L_d(1 + 3K_0)] - L_p K_0(1 - K_0) = 0. \tag{22}$$

In this equation the coefficients P_0 and $L_{p,d}$ are determined by the same general relations (8), (16), and (20) but with different genealogical coefficients, terminal factors, and equation of state for n_t:

$$b^2=3, \quad f_t=\frac{4-n_t}{18}, \quad K_0=2\frac{n_t-1}{4-n_t}, \quad n_t=1+9f_tK_0. \tag{23}$$

4. THE INTERVAL $0<n_t<1$

In this region the t_{2g} system resonates between unoccupied and nine single-hole states. The conditions for ferromagnetic instability have an especially simple form

$$(3-P_0)(1-K_0)=(1-K_0)L_p+(3-P_0)L_d, \tag{24}$$

where

$$f_t=\frac{6-5n_t}{6}; \quad K_0=\frac{n_t}{6-5n_t}; \quad n_t=6f_tK_0. \tag{25}$$

5. CONCLUSIONS

The large difference between the physical situation for $n_t<1$ (condition (24)) and $3>n_t>1$ (conditions (21) and (22)) lies in the fact that for $n_t<1$ the ferromagnetism condition (24) for a small number of particles, when $K_0\to 0$, could arise only for L_d or L_p of the order of 1. In the two other regions ($2>n_t>1$ and $3>n_t>2$) ferromagnetism certainly exists even for a small number of quasiparticles, i.e., when $K_0\ll 1$. The ferromagnetic instability vanishes when $K_0\approx L_d$, as follows from conditions (21) and (22). Note that as the chemical potential increases, both quantities L_p and L_d decrease from a positive value $w_{p,d}$ to a negative value equal to $-1+w_{p,d}$.

Therefore, for small values of K_0 the left-hand side of Eqs. (21) and (22) are negative. For this reason, ferromagnetic instability necessarily arises with a small deviation of the density n_t from the value 1 or 2, since in this situation the system resonates between magnetic (Hund) states. As the density of divalent dopant cations increases, the line of electrical neutrality (1) shifts to the boundary of the region of ferromagnetic ordering. Correspondingly, for a fixed magnitude of the energy difference $r=\epsilon_p-\epsilon_d$ the Curie temperature decreases with increasing concentration x. This qualitative effect is observed when lanthanum is replaced by calcium in the compounds $La_{1-x}Ca_xMnO_3$ with $x<1/2$ (Ref. 3).

[1] E. C. Stoner, Proc. Roy. Soc. A **165**, 372 (1938).
[2] J. Hubbard and K. P. Jain, J. Phys. C **2**, 1650 (1968).
[3] J. Goodenough, Phys. Rev. **100**, 564 (1955).
[4] J. C. Slater, Phys. Rev. **82**, 538 (1951).
[5] R. O. Zaĭtsev, Zh. Éksp. Teor. Fiz. **70**, 1100 (1976) [Sov. Phys. JETP **43**, 574 (1976).
[6] J. Hubbard, Proc. Roy. Soc. A **276**, 238 (1964).

Translated by M. E. Alferieff

Pseudocritical point on the melting curve of a metastable phase

E. G. Ponyatovskiĭ[a)]

Institute of Solid-State Physics, Russian Academy of Sciences, 142432 Chernogolovka, Moscow Region, Russia

(Submitted 15 July 1997)
Pis'ma Zh. Éksp. Teor. Fiz. **66**, No. 4, 260–262 (25 August 1997)

The possibility of the existence of a limit to which the melting curve can be extrapolated into the metastable region is discussed. The analysis is made for the example of GaSb, for which the stable and metastable phases of the $T-P$ diagram are known. When the melting curve of the high-pressure modification is extrapolated to low pressures, it crosses the curve of complete instability of the disordered phase at a point k. Since the melting curve is a line of equilibrium between two phases, one of which ceases to exist at the point k because the minimum of the thermodynamic potential that corresponds to this phase becomes degenerate, the melting curve terminates at the point k and further extrapolation of the curve is physically meaningless. © *1997 American Institute of Physics.* [S0021-3640(97)01116-X]

PACS numbers: 64.60.My, 64.70.Dv

A large number of works on the investigation of solid-phase amorphization of different substances subjected to high pressures have been published over the last few decades (see the reviews in Refs. 1 and 2). In analyzing the reasons for the transition of the crystalline phases into an amorphous state the authors sometimes extrapolate the melting curve of the phase of interest into its region of metastability, all the way down to low temperatures, without discussing the admissibility of such an extrapolation. The possible characteristic features of the behavior of the thermodynamic properties of metastable disordered (liquid and amorphous) and crystalline phases along the melting curve are neglected. The firmly established belief that the melting curve cannot terminate at a liquid–vapor type critical point on account of the difference in the symmetry of the liquid and crystalline phases is considered to be completely sufficient. It is shown below for the example of the compound GaSb that in some cases the melting curve terminates at a singular point and that extrapolation of the curve beyond this point is physically meaningless.

In Ref. 3 a phenomenological two-level model of ''pseudobinary solutions'' was used to describe the thermodynamic properties of GaSb in the disordered state. This model is formally similar to the two-level model proposed earlier for calculating the $T-P$ diagrams of the isomorphic transformation in crystalline cerium,[4] with the difference that the components of the solution in this model are assumed to be not atoms in different valence states, as in the case of cerium, but rather clusters with different short-range order. The internal parameter C in this model is the volume density of clusters with

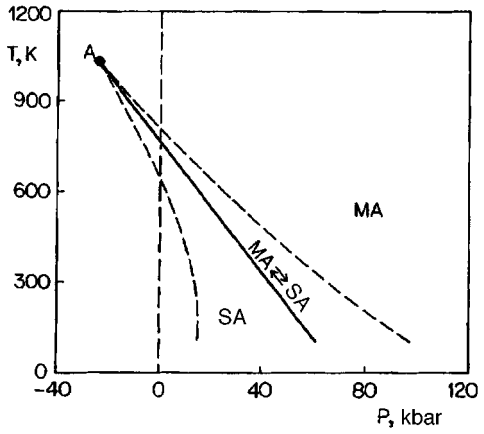

FIG. 1. Metastable $T-P$ diagram of the disordered (liquid and amorphous) GaSb: A — critical point, solid curve — line of the phase equilibrium of the semiconductor (SA) and metallic (MA) phases, dashed curves — lines of instability of the SA phase (top curve) and MA phase (bottom curve).

higher energy. The substances to which this two-level model is applicable have at least two crystalline polymorphic modifications, which differ strongly in structure, internal energy, and specific volume, for example, Ge, Si, GaSb, InSb, and H_2O. Such two-level systems are characterized by the existence of at least two disordered (liquid or amorphous) phases with different coordination numbers and volumes. They possess metastable phases in the $T-P$ diagram for a disordered state with a first-order phase equilibrium line terminating at a liquid–vapor type critical point and with curves of thermodynamic instability of these phases. The coordinates of the critical point vary strongly from system to system. For example, in the case of water the critical point on the phase equilibrium curve ''disordered low-density phase — disordered high-density phase'' lies at a low positive pressure ($\sim 150-200$ atm) and temperature of the order of 230 K. The anomalies of supercooled water at atmospheric pressure are transcritical and are described well in a two-level model.[5] In the case of the semiconductor elements Ge and Si (Ref. 6) and the compounds GaSb and InSb (Ref. 3) such a critical point lies at negative pressures, i.e., it is a virtual point, and the curves of the metastable equilibrium of the disordered metallic and semiconductor phases and the instability curves of these phases cross the temperature axis at atmospheric pressure.

Figure 1 displays the metastable $T-P$ diagram, calculated in Ref. 3, for GaSb in a disordered state. The solid line denotes the curve of equilibrium between the semiconductor (SA) and metallic (MA) disordered phases; the upper dashed line is the curve of instability of the SA phase with increasing temperature or pressure and the lower dashed line is the curve of instability of the MA phase with decreasing temperature or pressure; and, A is a liquid–vapor type critical point. In Fig. 2 the experimental stable $T-P$ diagram of GaSb with curves of melting and curves of the polymorphic transformation of the crystalline phases I and II (heavy solid lines) agrees with the computed metastable $T-P$ diagram of liquid and amorphous GaSb (heavy lines). The heavy dashed line in Fig. 2 represents the extrapolation of the melting curve of phase II into the region of meta-

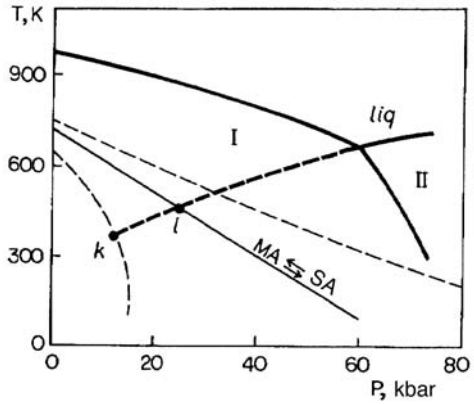

FIG. 2. Stable and metastable $T-P$ diagrams of GaSb: heavy solid curves — lines of phase equilibrium between the stable phases I, II, and liquid; the heavy dashed line is an extrapolation of the melting curve of the phase II into the region where this phase is metastable; the fine lines show the metastable $T-P$ diagram (see Fig. 1); k is a pseudocritical point.

stability of this phase. Figure 3 shows the curves of the thermodynamic potential G of the disordered GaSb versus the internal parameter C at the points l and k (see Fig. 2), which are the points of intersection of the extrapolated melting curve with the singular lines on the metastable $T-P$ diagram. These curves $G(C)$ were calculated in a two-level model using the constants presented in Ref. 3. The curves $G(C)$ are arbitrarily arranged relative to the ordinate axis for visual convenience. Curve *1* possesses two minima with equal thermodynamic potentials. The minimum of $G(C)$ corresponds to the SA phase for low values of C and the MA phase for large values of C. As one can see from Fig. 2 and 3,

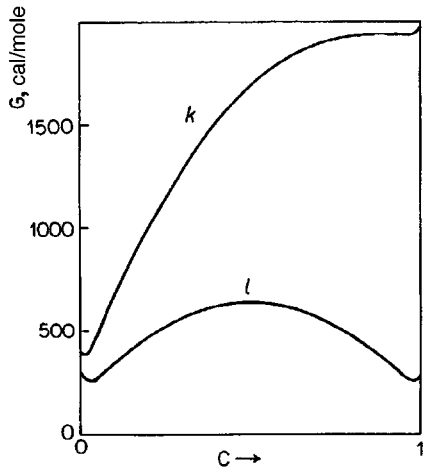

FIG. 3. Curves of the thermodynamic potential of GaSb in a disordered state versus the internal parameter C at the points k and l (Fig. 2).

at the point k the minimum of $G(C)$ corresponding to the disordered metallic state degenerates and this equilibrium ceases to be a phase. Since the melting curve is by definition a curve of the thermodynamic equilibrium between two phases, in the case at hand the critical phase II and the disordered metallic phase MA, which ceases to exist to the left of the point k, extrapolation of the melting curve to the left of this point becomes physically meaningless. Therefore the melting curve of the phase II terminates at the point k. This point is not a classical liquid–vapor type critical point because in it only one of the phases becomes unstable and the properties of both phases do not become identical. For this reason, it should be called a pseudocritical point.

I am grateful to the Russian Fund for Fundamental Research for financial support of Projects 96-02-18545 and 96-15-96806.

[a)]e-mail: ponyatov@issp.ac.ru

---

[1]E. G. Ponyatovsky and O. I. Barkalov, Mater. Sci. Rep. **8**, 147 (1992).
[2]S. M. Sharma and S. K. Sikka, Prog. Mater. Sci. **40**, 1 (1996).
[3]E. G. Ponyatovsky and T. A. Pozdnyakova, J. Non-Cryst. Solids **188**, 153 (1995).
[4]I. L. Aptekar' and E. G. Ponyatovskiĭ, Fiz. Met. Metalloved. **25**, 777 (1968).
[5]E. G. Ponyatovskiĭ, V. V. Sinitsyn, and T. A. Pozdnyakova, JETP Lett. **60**, 360 (1994).
[6]L. I. Aptekar', Dokl. Akad. Nauk SSSR **249**, 1099 (1979) [Sov. Phys. Dokl. **24**, 993 (1979)].

Translated by M. E. Alferieff

Quantum dot multiexcitons in a magnetic field

V. D. Kulakovskii
Institute of Solid State Physics, Russian Academy of Sciences, 142432 Chernogolovka, Moscow Region, Russia; Technische Physik, Universität Würzburg, Am Hubland, 97074 Würzburg, Germany

M. Bayer, M. Michel, A. Forchel, T. Gutbrod, and F. Faller
Technische Physik, Universität Würzburg, Am Hubland, 97074 Würzburg, Germany

(Submitted 15 July 1997)
Pis'ma Zh. Éksp. Teor. Fiz. **66**, No. 4, 263–268 (25 August 1997)

Multiexcitons confined in InGaAs/GaAs quantum dots (QDs) with a lateral size slightly exceeding the exciton Bohr radius are investigated by magnetophotoluminescence spectroscopy at 2 K. The Coulomb correlations in the two-exciton complex result in an additional confinement, which increases with decreasing dot size, while a magnetic field reduces this effect. A three-exciton complex is confined only by the geometric confinement potential of the QD. The exciton–exciton repulsion increases with decreasing dot size, while a magnetic field decreases the repulsion strongly when the magnetic length becomes smaller than the lateral size of the QD. A shell model for the QD multiexciton states is proposed. © *1997 American Institute of Physics.* [S0021-3640(97)01216-4]

PACS numbers: 73.61.Ey, 71.35.Ji

Optical studies of semiconductor quantum dots (QDs) open up new possibilities for investigating many-particle atoms consisting of electrons (e) and holes (h) or of multiexcitons. In bulk and in quantum wells the two excitons in a biexciton are spatially localized by their effective Coulomb interaction alone. Molecules of three or more excitons in semiconductors with simple conduction and valence band structures are unstable because of the strong Pauli repulsion between electrons (holes) with the same spin. In QDs the geometric confining potential localizes excitons in the same spatial region. The $e-h$ interaction results in a renormalization of the transition energies and of the transition matrix elements of the confined multiexcitons. In particular, it has been shown that the spatial confinement increases the biexciton binding energy in QDs.[1–5]

In the present paper we investigate the influence of an external magnetic field on multiexciton states in single, free-standing InGaAs/GaAs QDs. In contrast to the 2D case, in QDs, with their discrete energy level structure (caused by the geometric confining potential), the magnetic field lifts degeneracies of levels and, to some extent, leads the system back to a ''quasicontinuous'' energy spectrum.[6–10] Recent high-excitation studies of the QD magnetophotoluminescence (PL), carried out on arrays containing a large number of QDs, have revealed that the effect of many-particle interactions is relatively small.[11,12] The interaction energy was found to be within the inhomogeneous broadening of the luminescence by dot size fluctuations. We investigate the PL spectra of single QDs,

which allow us to obtain excitonic emission lines with narrow linewidths[5,13] and to extract information on $e-h$ interaction effects.

Isolated InGaAs/GaAs QDs were fabricated from a 5-nm thick quantum well by using low voltage electron beam lithography.[14] For the optical investigations a spacing of 50 μm between adjacent single dots was chosen. This permits investigation of individual QDs in an optical cryostat with a superconducting solenoid. The QDs were excited by an Ar^+-ion laser. The excitation power was varied in the range between 0.1 and 200 μW and the laser spot was focused down to a diameter of 20 μm. The single dot emission was dispersed by a monochromator and detected by a liquid-nitrogen-cooled CCD camera. The luminescence was integrated over times ranging from 10 seconds at high excitation densities to 2 minutes at low excitation densities.

For our studies we chose QDs with lateral sizes $L_{x,y}$ of 50–80 nm, which are slightly larger than the exciton radius a_x. In this case, on the one hand, there is a balance between the Coulomb interaction and the QD confining potentials. On the other hand, at relatively small magnetic fields of 3–6 T the magnetic length l_B is comparable to both $L_{x,y}$ and a_x and strongly influences the multiexciton states in the QD. We compare the behavior of excitons in such small dots with that in a relatively large dot, where the localization of carriers in the exciton due to the Coulomb interaction dominates.

Figures 1a and 2a display PL spectra from single $5\times45\times55$ and $5\times50\times70$ nm boxes at $B=0$ for different excitation densities. At low excitation the line labeled by X corresponds to the recombination of a single $e-h$ pair (exciton) in the QD. Its full width at half maximum is about 2 meV. This width is larger than the width in natural QDs.[13] This may be due to elastic scattering processes or to temporal fluctuations of the QD potential on account of photoexcited surface charges.

With increasing excitation density a pronounced shoulder X_2 appears on the low-energy side of the exciton line; this shoulder must be assigned to emission from a two-exciton state (recombination of one of two excitons confined in the dot; Fig. 1d). In the smaller QD (Fig. 2a) the X_2 line is well resolved and is located more than 2 meV below the exciton line. This shift arises from the effective exciton–exciton Coulomb interaction in the dot and can therefore be associated with the binding energy of the two-exciton state, Δ_{xx}. In the larger dot (Fig. 1a) the X_2 line is located closer to the X line and is only weakly resolved in the spectrum. To resolve it we recorded the differential spectrum $d2$ (Fig. 1b), which is the difference of the spectra recorded at $P=25$ μW and 10 μW. It shows that Δ_{xx} = 1.2 meV in the $5\times50\times70$ nm dot. The decrease of Δ_{xx} is in agreement with theoretical predictions .[2,3]

A comparison of Figs. 1a and 2a shows that the two-exciton-state emission from the smaller QD appears at a much (nearly 5 times) higher optical excitation. This difference is most likely due to a higher rate of surface recombination in the small QD, which precludes filling the dot with many excitons even at an excitation power of 1 mW (Fig. 2a, trace *3*). In contrast, Fig. 1a shows that in case of the larger QD an increase of the excitation power to 50–100 μW results in a further increase of the number of excitons. The Pauli exclusion principle forbids the relaxation of additional electrons and holes to the ground shells because the latter are only twofold spin-degenerate. Therefore the third exciton should occupy an excited state as shown in Fig. 1d. As a result, two lines, X_3 and

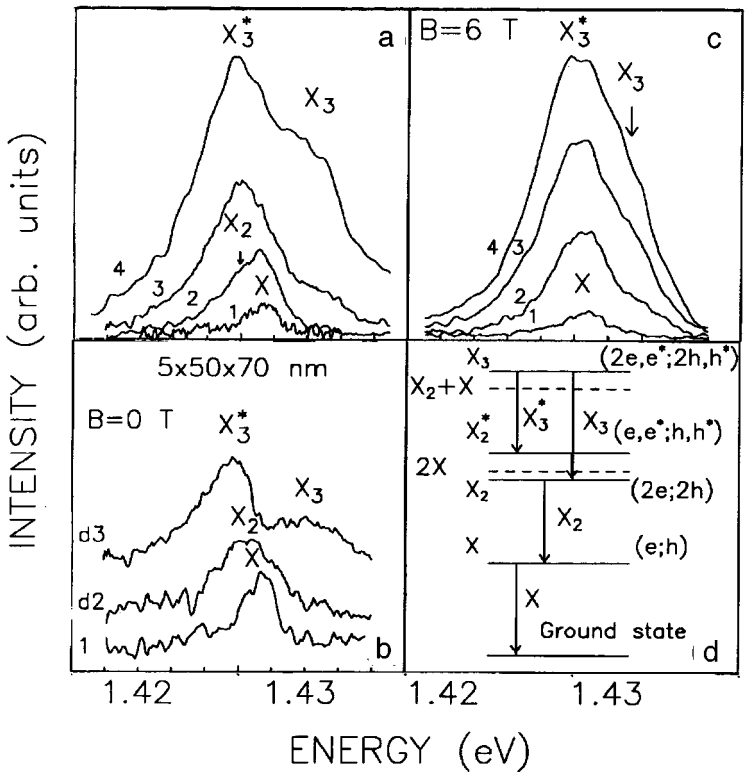

FIG. 1. Photoluminescence spectra from a single $5\times50\times70$ nm QD at $B=0$ (a,b) and 6 T (c) for different excitation powers. P [μW] = 10 (*1*), 25 (*2*), 50 (*3*), and 200 (*4*); the differential spectra $d1$ and $d2$ are obtained at 25 μW and 50 μW, respectively. The diameter of the excited spot is 20 μ. Scheme of the optical transitions of QD multiexcitons is shown in part (d). The dashed lines $2X$ and X_2+X indicate the sums of the energies of two excitons and of a biexciton and exciton, respectively.

X_3^*, are expected in the emission spectrum of X_3, which correspond to transitions to the ground or to the excited two-exciton state. Figure 1a shows that only the line X_3 appears in the spectrum as a pronounced shoulder on the high-energy side of the X line. The line X_3^* is not resolved on the low-energy tail of the line X_2 but it is well-resolved in the differential spectrum shown in Fig. 1b, trace $d3$. Thus the two peaks located 2 meV below and 3 meV above the X transition can be assigned to the recombination of excitons in the inner and outer shells, respectively. The intensity of X_3^* is about twice that of X_3, in accordance with ratio of the numbers of electrons in the inner and outer shells. The differential spectrum recorded at 50 μW is very similar to the QD emission spectrum at 200 μW, when the mean number of excitons in the QD exceeds 2.

The magnetic field changes the PL spectra. Figsures 1c and 2b display QD spectra recorded under the same excitation conditions as those in Figs. 1a and 2a, respectively, but at $B=6$ T. In the small QD (Fig. 2b) emission from the two-exciton state appears only as a poorly resolved shoulder, indicating a strong decrease of Δ_{xx}. In the larger dot

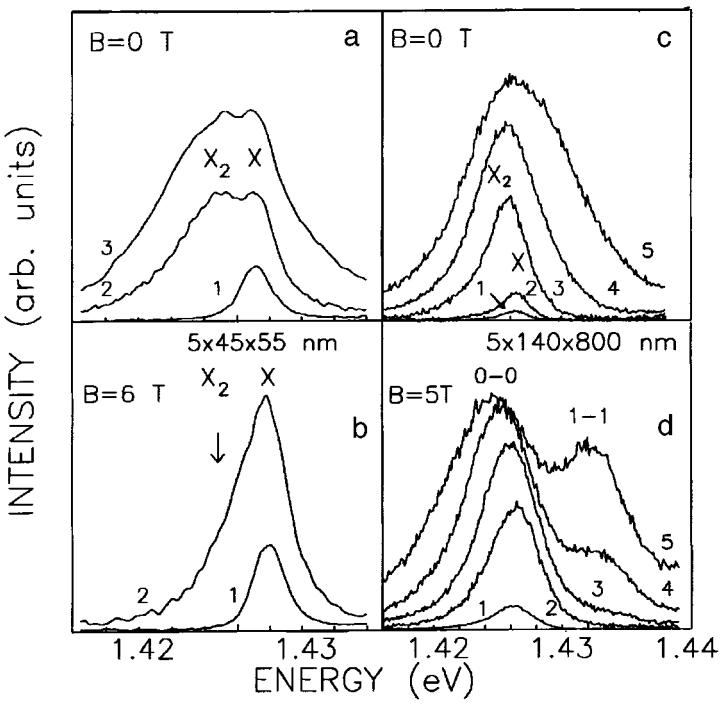

FIG. 2. Photoluminescence spectra from single $5\times45\times55$ nm (a,b) and $5\times140\times800$ nm (c,d) QDs for different excitation powers and magnetic fields. In parts (a) and (b) P [μW] = 100 (*1*), 400 (*2*) and 1000 (*2*). In parts (c) and (d) P [μW] = 10 (*1*), 20 (*2*), 100 (*3*), 200 *(4)*, 400 *(5)* and P [μW] = 20 *(1)*, 100 *(2)* 200 (*3*), 400 (*4*), 600 (*5*), respectively.

the lines X and X_2 are not resolvable at all (Fig. 1c). The first pronounced high energy shoulder appears at 50 μW, as in the case $B=0$. Therefore we can conclude that this shoulder is connected with the appearance of the third exciton in the QD. The effect of exciton–exciton interaction in the two-exciton complex is observed only in differential spectra recorded at 20–40 μW, which show a relatively small ($\sim$0.6 meV) red shift which could be connected to Δ_{xx}.

A comparison of the high excitation spectra in Figs. 1a and 1c shows that the splitting of the emission lines X_3^* and X_3 corresponding to the recombination of three-exciton complexes is also markedly smaller at $B=6$ T than at $B=0$ T. As can be seen from the transition scheme in Fig. 1d, the splitting of these lines reflects the energy of the first excited two-exciton state δ_1. The decrease of δ_1 means that the magnetic field suppresses the repulsion of excitons with similar electron (hole) spins. This behavior is in accordance with results of previous studies of QD PL on dot arrays.[11]

The limitations originating from the Pauli repulsion should decrease with increasing ratio $L_{x,y}/a_x$. Indeed, Fig. 2 illustrates that the PL behavior in a large dot is very similar to that in a quantum well. First, exciton and then biexciton emission appears in the spectrum with increasing excitation (Fig. 2c). However, no pronounced structure appears

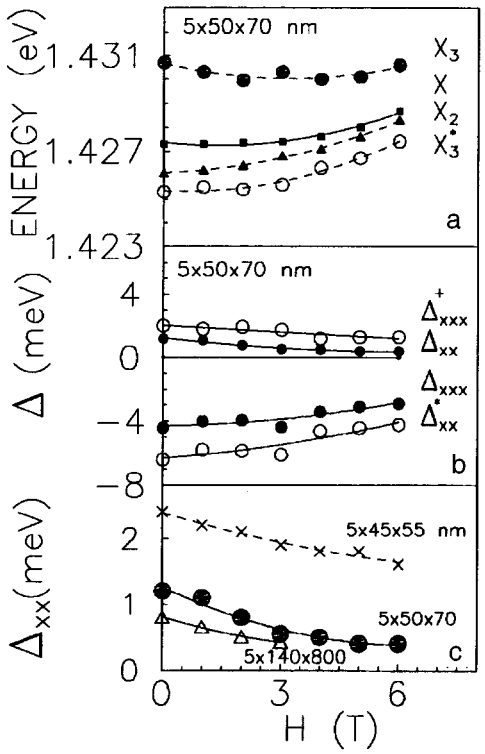

FIG. 3. Magnetic field dependence of the exciton and multiexciton transition energies (a) and of the multiexciton binding energies in the QDs (b,c).

on the high energy side of the X line with further increase of excitation density. Instead, the line transforms into the broad, structureless emission that is characteristic of a Fermi system ($e-h$ plasma). Second, in contrast to the case of small dots, the new line in the magnetoluminescence spectrum appears at a much higher energy, which is close to the cyclotron energy and hence must be assigned to the emission of electrons and holes in the next Landau level rather than to an exciton–exciton interaction.

The magnetic field dependence of the transition energies in the $5\times50\times70$ nm QD is shown in Fig. 3c. The exciton energies were determined from the PL spectra at the lowest (10 μW) excitation power, whereas the transition energies of the two- and three-exciton complexes were obtained from the differential spectra recorded at $P=25$ and $P=100$ μW, respectively. Using these data and the scheme of multiexciton transitions in Fig. 1d, we have determined the magnetic field dependence of the exciton–exciton interaction energies in the ground state, $\Delta_{xx}=\hbar\omega(X)-\hbar\omega(X_2)$, and in the excited two-exciton state, $\Delta^*_{xx}=\Delta_{xx}+\hbar\omega(X_3)-\hbar\omega(X^*_3)$, and also the interaction energy of a third exciton in the three-exciton state, $\Delta_{xxx}=\hbar\omega(X_3)-\hbar\omega(X)$. These energies are displayed in Fig. 3b. Δ_{xx} is positive whereas Δ_{xxx} is negative. This means that the effective exciton–exciton interaction in the QD is attractive only for biexcitons. Δ_{xx} increases with decreasing lateral size of the QD, from 0.8 meV for the large dot to 2.2 meV for the

smallest, 45×55 nm dot. Magnetic field decreases Δ_{xx}. The decrease depends weakly on the size of the QD and reaches 0.7–0.8 meV at 6 T. This effect originates mainly from Zeeman splitting of excitons in the magnetic field because the two excitons form s singlet state and so the second exciton must fill an excited spin state in the magnetic field. The three-exciton state has an energy larger than three times the single exciton energy and is threfore confined only by the QD confining potential. This is obviously a result of the strong Pauli repulsion of electrons (holes) with identical spins which appears with the third exciton and pushes the third exciton into the next shell. An increased magnetic field leads to a localization of particles within $2l_B$ and, hence, a decrease in the Pauli repulsion, in agreement with the experimental data in Fig. 3b. Δ_{xxx} changes from -4 meV at $B=0$ T to -3 meV at 6 T. It is obvious that Δ_{xxx} should tend to zero for L_x and/or $L_y \gg l_B$, i.e., when the excitons in the QD are separated by several l_B. This case is realized in the large, 140×800 nm, dot. Similar arguments explain also the behavior of the excited two-exciton state in the QD. Figure 3b shows that Δ_{xx}^{*} changes from -5 meV at $B=0$ T to -3.5 meV at 6 T.

Finally, we can consider the case when a third exciton in the ground state is added to the excited two-exciton state. Its binding energy is given by $\Delta_{xxx}^{+}=\hbar\omega(X_3^{*})-\hbar\omega(X)$. Figure 3b shows that the effective interaction in this case is attractive and that Δ_{xxx}^{+} even exceeds Δ_{xx}. This is natural because the third exciton fills the empty place in the inner shell occupied by one particle. The Pauli repulsion in this case has no effect, whereas the correlation energy increases with the number of particles in the QD. As expected, Fig. 3b shows that a magnetic field reduces Δ_{xx} and Δ_{xxx}^{+} in a similar way.

To sum up, we have investigated experimentally multiexciton complexes consisting of two and three excitons which are confined in a single QD with lateral dimensions slightly larger than the exciton Bohr radius. The exciton–exciton interaction in a two-exciton complex enhances the confinement; it is rather strong at zero magnetic field but decreases with increasing magnetic field. The three-exciton complex is confined only by the QD geometric confining potential. A magnetic field strongly reduces the exciton–exciton repulsion in such a complex.

This study was supported in part by the Volkswagen Foundation, by the Russian Fund for Fundamental Research RFBR 97-02-17948, and by a NATO grant.

[1] S. Schmitt-Rink, D. A. B. Miller, and D. S. Chemla, Phys. Rev. B **35**, 8113 (1987).
[2] G. W. Bryant, Phys. Rev. B **41**, 1243 (1990).
[3] Y. Z. Hu, S. W. Koch, M. Lindberg *et al.*, Phys. Rev. Lett. **64**, 1805 (1990).
[4] K. Brunner, G. Abstreiter, G. Böhm *et al.*, Phys. Rev. Lett. **73**, 1138 (1994).
[5] R. Steffen, A. Forchel, T. L. Reinecke *et al.*, Phys. Rev. B **54**, 1510 (1994).
[6] T. Demel, D. Heitmann, P. Grambow, and K. Ploog, Phys. Rev. Lett. **64**, 788 (1990).
[7] P. A. Maksym and T. Chakraborty, Phys. Rev. Lett. **65**, 108 (1990).
[8] A. A. Andreev, Y. M. Blanter, and Yu. E. Lozovik, Int. J. Mod. Phys. B **9**, 1843 (1995).
[9] V. Halonen, T. Chakraborty, and P. Pietilainen, Phys. Rev. B **45**, 5980 (1992).
[10] U. Bockelmann, Phys. Rev. B **50**, 17271 (1994).
[11] M. Bayer, A. Schmidt, A. Forchel *et al.*, Phys. Rev. Lett. **74**, 3439 (1995).
[12] R. Rinaldi, P. V. Giugno, R. Cingolani *et al.*, Phys. Rev. Lett. **77**, 342 (1996).
[13] A. Zrenner, L. V. Butov, M. Hagn *et al.*, Phys. Rev. Lett. **72**, 3382 (1994).
[14] R. Steffen, T. Koch, J. Oshinowo, and A. Forchel, Appl. Phys. Lett. **68**, 225 (1996).

Published in English in the original Russian journal. Edited by Steve Torstveit.

Features of the melting dynamics of a vortex lattice in a high-T_c superconductor in the presence of pinning centers

M. E. Gracheva, V. A. Kashurnikov,[a)] and I. A. Rudnev
Moscow State Engineering Physics Institute (Technical University), 115409 Moscow, Russia

(Submitted 4 July 1997; resubmitted 18 July 1997)
Pis'ma Zh. Éksp. Teor. Fiz. **66**, No. 4, 269–274 (25 August 1997)

The phase transition ''triangular lattice–vortex liquid'' in layered high-T_c superconductors in the presence of pinning centers is studied. A two-dimensional system of vortices simulating the superconducting layers in a high-T_c Shubnikov phase is calculated by the Monte Carlo method. It was found that in the presence of defects the melting of the vortex lattice proceeds in two stages: First, the ideal triangular lattice transforms at low temperature ($\simeq 3$ K) into islands which are pinned to the pinning centers and rotate around them and then, at a higher temperature ($\simeq 8$ K for $T_c = 84$ K), the boundaries of the ''islands'' become smeared and the system transforms into a vortex liquid. As the pinning force increases, the temperatures of both phase transitions shift: The temperature of the point ''triangular lattice–rotating lattice'' decreases slightly (to $\simeq 2$ K) and the temperature of the phase transition ''rotating lattice–vortex liquid'' increases substantially ($\simeq 70$ K).
 [S0021-3640(97)01316-9]

PACS numbers: 74.76.Bz, 74.80.Bj, 74.80.Dm

In recent years a great deal of attention has been devoted to investigations of the dynamics of phase transformations in a vortex lattice in high-T_c superconductors.[1] Especially important for practical applications of superconducting materials are questions concerning the interaction of vortex structures with both natural and artificial pinning centers.[2–8]

In the present letter we shall study a two-dimensional vortex lattice, simulating a high-T_c superconducting layer, assuming weak coupling of the flux lines in a direction perpendicular to the $a-b$ plane and in the presence of pinning centers with density much lower than that of the flux lines. It will be shown that the vortex lattice melts in two stages: First, ''islands,'' twisted around the pinning centers and weakly coupled with one another, form from an ideal triangular lattice and then, as the temperature increases further, the ''islands'' of the triangular lattice likewise melt and a transition into a liquid vortex phase occurs.

We note that vortex density patterns, similar to those which we calculated, with ''flow around'' the pinning centers were obtained in Ref. 2, where the penetration of

vortices through the boundary of the superconductor was investigated. Questions concerning ''orientational'' melting were studied recently in Ref. 9.

Let us consider a system of flat Abrikosov vortices arranged on a periodic square lattice. The spacing of the spatial grid was chosen so that the period of the grid is much less than the period of an ideal triangular vortex lattice.

Neglecting the interaction of the vortices with an external field, we have the following effective Hamiltonian:[8]

$$H=\frac{1}{2}\sum_{i\neq j}^{N} H(r_i,r_j)n_i n_j+\sum_{i=1}^{N} U_p(r_i,T)n_i, \tag{1}$$

where

$$H(r_i,r_j)=U_0(T)K_0\left(\frac{|r_i-r_j|}{\lambda(T)}\right), \quad U_0(T)=\frac{\Phi_0^2 d}{2\pi\lambda^2(T)\mu_0}.$$

Here $U_p(r_i,T)$ is the interaction energy of a vortex with a point defect at the ith site; n_i is the occupation number of the vortices (0 or 1) at the ith site of the spatial grid with a total number of sites N; $\Phi_0=hc/2e$ is the flux quantum; K_0 is a zero order modified Bessel function; d is the thickness of the superconducting layer; $\lambda(T)=\lambda(0)/\sqrt{1-(T/T_c)^{3.3}}$ is the penetration depth; and, $\mu_0=4\pi\times10^{-7}$ H/m.

For a concrete calculation we choose parameters close to the characteristics of the high-T_c superconductor $Bi_2Sr_2CaCu_2O_x$: $d=2.7$ Å, $\lambda(T=0)=1800$ Å, and $T_c=84$ K.[10]

Let the external field be $B=0.1$ T, which corresponds to the real order of magnitude of the induction for which melting of the vortex lattice is observed in bismuth high-T_c superconductors.[10,11]

The main calculations were performed on a 200×200 square spatial grid with periodic boundary conditions by the standard Monte Carlo method following the Metropolis algorithm.

The number of flux lines threading the 200×200 plane is $N_v=150$. The real vortex density corresponding to the given field B was reproduced by varying the spacing of the spatial cells so that the period a_v of the triangular vortex lattice would satisfy the relation

$$a_v^2=2\Phi_0/\sqrt{3}B. \tag{2}$$

The interaction energy with a pinning center at the point r_i was taken in the form

$$U_p(r,T)=-[U_0(T)/8]\delta_{r,r_i}, \tag{3}$$

which corresponds to $U_p(r=r_i,T=2\ \text{K})=-3.5$ meV.

The values chosen for the depth of the potential well for a pinning center are close to those actually observed in high-T_c superconductors.[1,8] Stronger pinning was also modeled ($U_p(r,T)$ is 30 times larger in magnitude).

Figures 1 and 2 display the vortex density distribution obtained by summing the instantaneous states of the vortex lattice (instantaneous vortex density) every 100 Monte

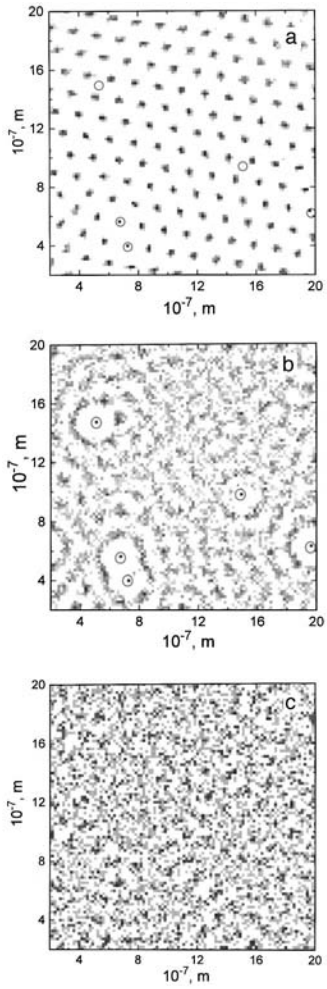

FIG. 1. Dynamics of melting of the vortex lattice with weak pinning. Circles — defects ($U_p(T=2\ \mathrm{K}) = -3.52$ meV): a) $T=1$ K; b) $T=5$ K; c) $T=35$ K.

Carlo (MC) steps. Ordinarily, 10^4 MC steps were required to thermalize the system and 10^4 MC steps were made for the calculation (i.e., data on $10^4/100$ states of the system were entered in the statistics).

Several (usually five) randomly distributed pinning centers were introduced into the lattice. This corresponds completely to the real defect density in fields $B=0.1$ T relative to the vortex density.

A practically ideal triangular lattice is reproduced in Fig. 1a ($T=1$ K). As one can see, not all defects are occupied by vortices. This attests to the stiffness of the lattice[1] at such temperatures. Defects would have been occupied with vortices if the correspondence between the arrangement of defects and the centers of the triangular lattice were ideal. At

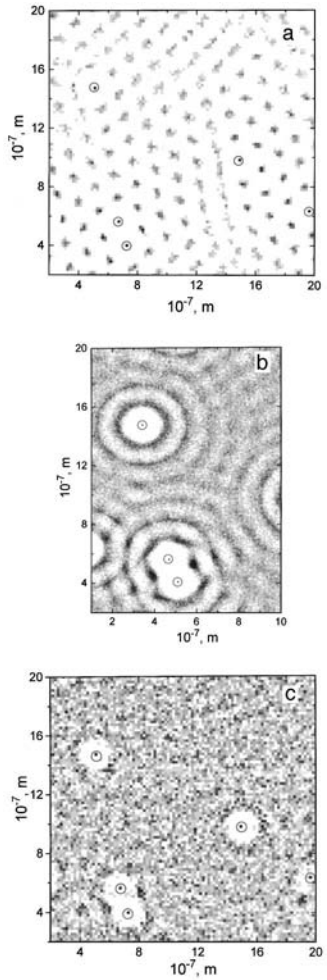

FIG. 2. Dynamics of melting of a vortex lattice with strong pinning, circles — defects ($U_p(T=2\ \mathrm{K}) = -0.115$ eV): a) $T=2$ K; b) $T=15$ K; c) $T=70$ K. For the case b) the scale on the abscissa is enlarged.

a temperature of 3 K all defects are occupied by vortices, which rigidly hold the lattice around themselves. On account of the irregularity of their arrangement the defects seemingly pull the lattice apart, breaking it at locations which are (still) far away from defects. The boundaries between the coherent regions which arise are melted and the lattice loses its stiffness.

As the temperature increases further (up to 5 K — Fig. 1b), ''islands'' of the triangular lattice, which are held around the defects and which move relative to the defects as an axis of rotation, seemingly rotate, smearing the vortex density in concentric circles with maxima on coordination spheres. A vortex-depleted region forms around the defects themselves at a distance of one coordination sphere corresponding to the period of the ideal triangular lattice, since a stationary pinned vortex prevents other vortices

from approaching closer. In this new phase state (the transition temperature is estimated to be $T_m^1 \simeq 3$ K), which we shall call a ''rotating lattice'' by analogy to the ''floating lattice'' in Ref. 2, long-range order still is present within the coherent regions, which are much larger than the average distance between the vortices and are rigidly coupled to the pinning centers.

As the temperature increases further (right up to $T = T_m^2 \simeq 7.5$ K), the vortices start to detach from the defects, the coherent regions break up, and at $T = 35$ K (far from the transition point), for example, a completely melted vortex liquid is observed (Fig. 1c).

Therefore the process of melting of the lattice in the presence of pinning centers proceeds in three phases: triangular lattice–rotating lattice–vortex liquid.

We also investigated melting in the presence of defects with a 30 times higher energy of attraction of the vortices (i.e., $U_p(T = 2\ \text{K}) = -0.115$ eV) — see Fig. 2. The main differences between this situation and the melting process studied above with weaker pinning (Fig. 1) are as follows:

a) The transition point from the triangular lattice to a rotating lattice is shifted in the direction of lower temperatures ($T_m^1 \simeq 2$ K) . Thus, displacement of the lattice starts already at $T = 2$ K (Fig. 2a), while in the case of weaker pinning at the same temperature we see a stationary triangular lattice. The pinning centers with strong attraction immediately break up the regular lattice into parts which drift behind the centers.

b) Strong pinning increases the temperature range of the rotating phase. Almost ideal twisted regions are seen at intermediate temperatures (Fig. 2b) right up to $T = 70 - 80$ K (Fig. 2c).

For a quantitative investigation of the phase transition points on melting of a vortex lattice, either a structure factor $S(q)$ for estimating the degree of long-range order or a hexagonal parameter S_6[10,11] for analyzing the short-range correlations (equivalent to the Lindemann criterion for rms deviations) is ordinarily calculated. The alternative method is to calculate the specific heat $C(T)$ of the system taking account of the fact that according to the fluctuation-dissipation theorem this quantity is related with the fluctuation of the total energy $\langle E \rangle$ as

$$C(T) = [\langle E^2 \rangle - \langle E \rangle^2]/T^2. \tag{4}$$

We reproduce in Fig. 3 the function $C(T)$ for the case of weak pinning. A feature can be seen at $T_m^1 = 3$ K that corresponds to the transition point into the rotating–lattice state. Furthermore, a quite sharp ''front'' is observed, proving that this transition is of a thermodynamic character (second-order transition). The function $C(T)$ clearly separates into three stages: Growth of the specific heat, corresponding to T_m^1, starts at $T = 3$ K (Fig. 1a); next, after this diffuse maximum, a sharp jump occurs at $T = 5$ K; and, finally, the final transition into the vortex liquid state, corresponding to the sharp peak at $T = T_m^2 = 7.5$ K, occurs. The calculation of the specific heat with strong pinning gives two clear peaks in the function $C(T)$ which correspond to the temperatures $T_m^1 = 2.5$ K and $T_m^2 = 73$ K. This corresponds completely to the previously indicated differences between the weak and strong pinning regimes (the inset in Fig. 3 illustrates the region $T \simeq T_m^1$ for this case).

In closing, we shall analyze the main results of this work. We have investigated the phase transition ''triangular lattice–vortex liquid'' in a two-dimensional vortex system

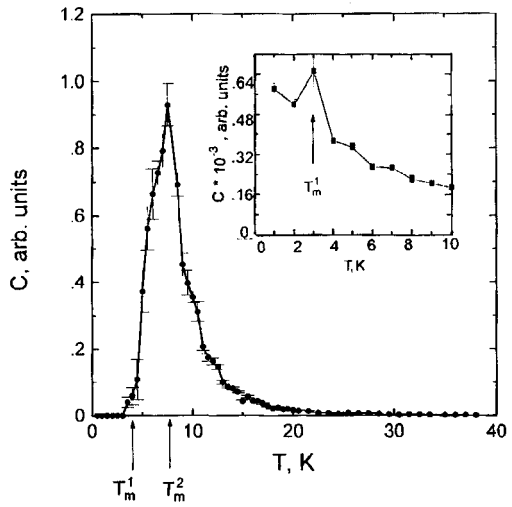

FIG. 3. Specific heat as a function of temperature for weak pinning. Inset: Region of the phase transition ''triangular lattice–rotating lattice'' for the case of strong pinning.

simulating superconducting layers in high-T_c superconductors. In the presence of pinning the system passes through an intermediate phase — a rotating lattice. The existence of the intermediate phase can be explained by the competition between two processes taking place against the background of increasing thermal mobility of the vortices: The high stiffness of the triangular lattice competes with the quite strong interaction with pinning centers, which strive to pin a vortex with its environment, causing the lattice to break up into islands around the defects.

In layered high-T_c superconductors, whose lattice is not as stiff[1] on account of the weak coupling of the superconducting layers with one another, the pinning force competes with the elastic properties of the vortex structure, expanding the region of the rotating-lattice phase up to $T \simeq T_c$. In ordinary superconductors the high stiffness of the three-dimensional Abrikosov lattice decreases only near T_c, so that the temperature range of the phase state mentioned is much narrower.[12]

The fact that the temperature of the transition into the rotating phase is low (2–3 K) signifies that the real and therefore defect high-T_c superconductors in a mixed state occupy this state practically immediately. This should lead to a substantial broadening of the current-voltage characteristics even in weak magnetic fields. This could explain the absence of an Abrikosov lattice, as tested according to the broadening of the current-voltage characteristic,[13] sometimes observed in thin films of ordinary superconductors.

Calculations show that both of the phase transitions studied above are second-order thermodynamic transitions. This is proved by the special features in the temperature dependence of the specific heat (Fig. 3).

We are grateful to Yu. E. Lozovik and B. V. Svistunov for a helpful discussion of the results and to D. V. Mel'nikov for assisting in the preparation of this paper. This work was sponsored by the State Science and Technology Program ''Current problems in

condensed-state physics,'' subprogram ''Superconductivity,'' Projects 95019 and 96026. One of us (M. E. G.) thanks the Samsung Electronics Company for financial support.

[a)]e-mail: kash@supercon.mephi.ru

---

[1] G. Blatter, M. V. Feigel'man, V. B. Geshkenbein *et al.*, Rev. Mod. Phys. **66**, 1125 (1994).
[2] C. Reichardt, J. Groth, C. J. Olson *et al.*, Phys. Rev. B **54**, 16108 (1996).
[3] D. Ertas and D. R. Nelson, Physica C **272**, 79 (1996).
[4] S. Ruy, M. Hellerquist, S. Doniach *et al.*, Phys. Rev. Lett. **77**, 5114 (1996).
[5] R. E. Hetzel, A. Sudbo, and D. A. Huse, Phys. Rev. Lett. **69**, 518 (1992).
[6] K. Yates, D. J. Newman, and P. A. J. de Groot, Phys. Rev. B **52**, R13149 (1995).
[7] R. Sasik and D. Stroud, Phys. Rev. B **52**, 3696 (1995).
[8] I. A. Rudnev, V. A. Kashurnikov, and M. A. Katargin, *Proceedings of the 8th Workshop on Critical Current in Superconductors*, Japan, May 27–29, 1996, Report P1-15; M. E. Gracheva, M. A. Katargin, V. A. Kashurnikov, and I. A. Rudnev, Fiz. Tverd. Tela (St. Petersburg) **23**, No. 11 (1997) [Phys. Solid State], in press.
[9] Yu. E. Lozovik and E. A. Rakoch, JETP Lett. **65**, 282 (1997).
[10] S. Ruy, S. Doniach, G. Deutscher, and A. Kapitulnik, Phys. Rev. Lett. **68**, 710 (1992).
[11] E. Zeldov, D. Majer, M. Konczykovski *et al.*, Nature **375**, 373 (1995).
[12] A. I. Larkin and Yu. N. Ovchinnikov, J. Low Temp. Phys. **34**, 409 (1979).
[13] A. V. Nikulov, D. Yu. Remisov and V. A. Oboznov, Phys. Rev. Lett. **75**, 2586 (1995).

Translated by M. E. Alferieff

Single-electron computing without dissipation

A. M. Bychkov, L. A. Openov,[a)] and I. A. Semenihin
Moscow State Engineering Physics Institute (Technical University), 115409 Moscow, Russia

(Submitted 2 July 1997)
Pis'ma Zh. Éksp. Teor. Fiz. **66**, No. 4, 275–279 (25 August 1997)

The possibility of performing single-electron computing without dissipation in an array of tunnel-coupled quantum dots is studied theoretically, taking the spin gate NOT (inverter) as an example. It is shown that the logical operation can be implemented at the stage of unitary evolution of the electron subsystem, although complete switching of the inverter cannot be achieved in a reasonable time at realistic values of model parameters. The optimal input magnetic field is found as a function of the interdot tunneling energy and intradot Coulomb repulsion energy. © *1997 American Institute of Physics.*
[S0021-3640(97)01416-3]

PACS numbers: 73.20.Dx

Recent advances in the fabrication of nanometer scale quantum dots open up an opportunity for practical implementation of the idea of using the states of a quantum system for data coding and processing.[1] For example, the spins of individual electrons can be viewed as the bits of information: logical one (zero) corresponds to the ''up'' (''down'') direction of the electron spin at a given quantum dot. *Spin gates* (elementary sets of quantum dots performing particular logical functions) were discussed by Bandyopadhyay *et al.*[2] and later investigated theoretically by Molotkov and Nazin[3] and by Krasheninnikov and Openov.[4] If occupation/nonoccupation of a quantum dot by a single electron is viewed as a bit 1/0, one has *charge gates*, various kinds of which have been studied, e.g., by Lent *et al.*[5] and by Nomoto *et al.*[6] In arrays of quantum dots the quantum tunneling of electrons between adjacent dots and/or Coulomb interaction of electrons with each other play a role of ''wiring,'' resulting in signal propagation from dot to dot.

The operation of spin and charge gates is based on the principle of ''ground state computation.''[2,5] According to this principle, the influence of an external source on the input dots of a particular gate causes the electron subsystem to change to a new ground state. The final spin or charge configuration reflects the result of the ''calculation.'' This result can be read from the output dots of the gate. Quantum dot gates are believed to possess high-speed performance as a consequence of extremely fast switching between different electron ground states. However, the switching rate, being dictated by dissipation processes, is not known *a priori*. For a gate consisting of a few quantum dots and operating at sufficiently low temperatures, the switching rate may turn out to be rather low (10^6 to 10^9 s^{-1}; Ref. 6), thus slowing down the computation. Hence, in studies of the

potential use of quantum dot arrays for high-speed single-electron computing one should give special attention to inelastic relaxation processes.

An alternative way has been discussed recently by Bandyopadhyay and Roychowdhury.[7] They explored the dynamic behavior of the simplest spin gate NOT (inverter) and found that there exists an optimal input signal energy for achieving its *complete* switching in the absence of inelastic relaxation. However, it remains unclear how adequately the results obtained in Ref. 7 depict reality, since its authors used the Heisenberg model to describe the correlated electrons in quantum dots. Meanwhile, it is well known that this model is just a limiting case of the more realistic Hubbard model[8] and cannot be used if the interdot electron tunneling energy V is of the order of or greater than the intradot electron repulsion energy U. It is instructive to study a broad range of V and U values in order to see if the conclusions of Ref. 7 reflect the basic physics or are just a consequence of using a particular theoretical model.

In this paper we study the unitary evolution of the electron subsystem in the spin gate NOT (inverter) making use of the Hubbard model with arbitrary values of V and U. The inverter consists of two closely spaced quantum dots (A and B) occupied by two electrons.[2,3,7] One of the two dots (say, dot A) serves for writing the input signal to the gate by the action of the local magnetic field H_A. The second dot (B) is the output. At $H_A=0$ the ground state of the inverter is the entangled state with zero magnetic moments at both dots A and B. The logical function NOT is realized if for $H_A\neq 0$ the magnetizations (i.e., spin projections) of dots A and B have opposite directions. *Complete* switching of the inverter is said to take place if spin projections are saturated ($S_{zA}=1/2$, $S_{zB}=-1/2$ or $S_{zB}=1/2$, $S_{zA}=-1/2$, where $S_{zi}=\langle\hat{S}_{zi}\rangle=\langle\hat{n}_{i\uparrow}-\hat{n}_{i\downarrow}\rangle/2$, $\hat{n}_i$ being the particle number operators for dots $i=A,B$). Upon complete switching, the magnetizations of both dots reach the maximum absolute value $g\mu_B$, where g is the Landé factor and μ_B is the Bohr magneton. We stress that the ground state at any *finite* value of H_A is organized in such a way that $|S_{zA}|<1/2$ and $|S_{zB}|<1/2$ (Refs. 3,7). Hence, the complete switching of the inverter cannot be achieved through its *inelastic relaxation* to a new ground state.

The Hubbard Hamiltonian for the inverter has the form

$$\hat{H}=-V\sum_{\sigma}\ (\hat{a}^{+}_{A\sigma}\hat{a}_{B\sigma}+\hat{a}^{+}_{B\sigma}\hat{a}_{A\sigma})+U\hat{n}_{A\uparrow}\hat{n}_{A\downarrow}+U\hat{n}_{B\uparrow}\hat{n}_{B\downarrow}-g\mu_B H_A\sum_{\sigma}\ \hat{n}_{A\sigma}\ \mathrm{sign}(\sigma), \tag{1}$$

where the quantities V, U, H_A, g, and μ_B are defined above (the remaining notation is standard; see, e.g., Ref. 4). Here we assume that each dot has one size-quantized level with on-site potential $\varepsilon_0=0$ (i.e., all energies are measured from ε_0). In what follows, we set $g\mu_B=1$.

The complete orthonormal set of inverter eigenstates is formed by two-electron basis states $|1\rangle=|\uparrow,\downarrow\rangle$, $|2\rangle=|\downarrow,\uparrow\rangle$, $|3\rangle=|\uparrow\downarrow,0\rangle$, $|4\rangle=|0,\uparrow\downarrow\rangle$, $|5\rangle=|\uparrow,\uparrow\rangle$, $|6\rangle=|\downarrow,\downarrow\rangle$, where, e.g., the notation $|\uparrow,\downarrow\rangle$ denotes the state with a spin-up electron at dot A and a spin-down electron at dot B, $|\uparrow\downarrow,0\rangle$ denotes the state with two (spin-up and spin-down) electrons at dot A, and no electrons at dot B, etc. The magnetic moment of the electron with spin-up polarization is oriented along the direction of the local applied magnetic field H_A.

At $H_A=0$ the ground state eigenvector of the Hamiltonian (1) is

$$\Psi_0=\frac{1}{2}\sqrt{1+\frac{U}{\sqrt{U^2+16V^2}}}\left(|1\rangle+|2\rangle+\frac{\sqrt{U^2+16V^2}-U}{4V}|3\rangle\right.$$
$$\left.+\frac{\sqrt{U^2+16V^2}-U}{4V}|4\rangle\right). \tag{2}$$

The corresponding eigen energy is $E_0=(U-\sqrt{U^2+16V^2})/2$. In the ground state we have $\langle\Psi_0|\hat{S}_{zA}|\Psi_0\rangle=\langle\Psi_0|\hat{S}_{zB}|\Psi_0\rangle=0$. We suppose that at $t\leqslant 0$ the system is in its ground state.

If the local external magnetic field is applied at time $t=0$, then the wave function $\Psi(t)$ at $t\geqslant 0$ is

$$\Psi(t)=\sum_{k=1}^{6} A_k\Psi_k \exp(-iE_kt/\hbar), \tag{3}$$

where Ψ_k and E_k $(k=1-6)$ are eigenvectors and eigen energies of the stationary Schrödinger equation

$$\hat{H}\Psi_k=E_k\Psi_k. \tag{4}$$

The coefficients A_k are to be found from the initial condition $\Psi(t=0)=\Psi_0$. It is convenient to write Ψ_k as

$$\Psi_k=\sum_{n=1}^{6} B_{kn}|n\rangle. \tag{5}$$

Then

$$\Psi(t)=\sum_{n=1}^{6} f_n(t)|n\rangle, \tag{6}$$

where

$$f_n(t)=\sum_{k=1}^{6} A_kB_{kn} \exp(-iE_kt/\hbar). \tag{7}$$

The probability of finding the system in the basis state $|n\rangle$ at time t is $p_n(t)=|f_n(t)|^2$.

At arbitrary values of V, U, and H_A the eigenvalue equation (4) reduces to an algebraic equation of the third power in E_k. The resulting analytical expressions are too cumbersome for analysis, so it is more convenient to solve Eq. (4) numerically. Before proceeding to the results of these calculations, let us consider the limiting case $U=0$, which corresponds physically to $U\ll V$ (closely spaced large dots).[6]

At $U=0$ we have rather simple equations for the probabilities $p_n(t)$:

$$p_1(t)=\frac{1}{4}\left(1+\frac{4H_AV}{H^2+4V^2}\sin^2(\omega t/2)\right)^2, \quad p_2(t)=\frac{1}{4}\left(1-\frac{4H_AV}{H^2+4V^2}\sin^2(\omega t/2)\right)^2,$$

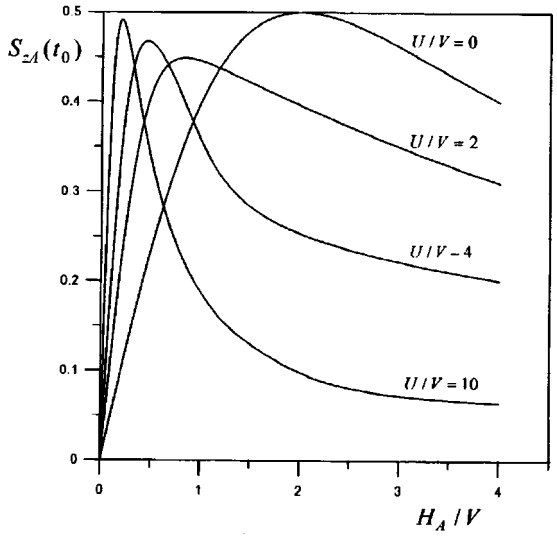

FIG. 1. The maximum value of $S_{zA}(t_0)$ versus H_A/V at different U/V.

$$p_3(t)=p_4(t)=\frac{1}{4}\left(1-\frac{16H_A^2V^2}{(H^2+4V^2)^2}\sin^4(\omega t/2)\right), \quad p_5(t)=p_6(t)=0, \tag{8}$$

where $\omega=\sqrt{H_A^2+4V^2}/\hbar$. From (6) and (8) it is straightforward to find that

$$S_{zA}(t)=\langle\Psi(t)|\hat{S}_{zA}|\Psi(t)\rangle=-S_{zB}(t)=(p_1(t)-p_2(t))/2=\frac{2H_AV}{H_A^2+4V^2}\sin^2(\omega t/2). \tag{9}$$

From (9) we see that the spins S_{zA} and S_{zB} are oppositely directed at any time t according to the physical truth table of the logical gate NOT.[3] For the sake of definiteness, let us consider the case $H_A>0$. In this case S_{zA} is always positive and peaks at $t_0=\pi/\omega$. Moreover, a *complete* switching, $S_{zA}(t_0)=1/2$ and $S_{zB}(t_0)=-1/2$, is achieved at $H_A/V=2$. The dependence of $S_{zA}(t_0)$ on H_A/V is shown in Fig. 1. We stress that this dependence has been obtained by us in the weak coupling limit of the Hubbard model. Nevertheless, it is analogous to those calculated in Ref. 7 within the Heisenberg model (i.e., in the strong coupling limit of the Hubbard model, $U\gg V$), except that in the Heisenberg model $\omega=\sqrt{H_A^2+4J^2}/\hbar$, $t_0=\pi/2\omega$, and $S_{zA}(t_0)$ reaches a maximum value of 1/2 at $H_A=2J$ (Ref. 7), where J is the antiferromagnetic exchange energy (for a two-site cluster $J=V^2/U$ at $U\gg V$). Hence, one may expect that complete switching of the inverter can occur at an *arbitrary* ratio of U to V.

To check this hypothesis, we calculated numerically the dependence of S_{zA} on t and $S_{zA}(t_0)$ on H_A/V at different values of U/V, where t_0 is generally defined as the time of the first maximum on the curve $S_{zA}(t)$, t_0 being a function of H_A/V and U/V. The curves

of $S_{zA}(t_0)$ versus H_A/V are shown in Fig. 1 for several values of U/V. One can see that an increase in U/V at first results in a decreased height of the maximum on the $S_{zA}(t_0)$ versus H_A/V curve. For $U/V>2$ the height of this maximum increases once more, but doesn't reach the saturation value 1/2 at finite U/V, though $S_{zA}(t_0)\to 1/2$ if $U/V\to\infty$ (this corresponds to the Heisenberg model and agrees with the results obtained in Ref. 7).

It seems that complete switching of the inverter cannot be achieved at realistic values of the ratio U/V, i.e., at $U/V\neq 0$ and $U/V\neq\infty$. Note, however, that at arbitrary values of H_A/V and U/V the function $S_{zA}(t)$ is not periodic in time since it includes several harmonics with different frequencies and amplitudes. Hence, in principle, the value $S_{zA}=1/2$ can be achieved at some longer time. But this case is of no interest for us since we should like not only to reach the maximum permissible value of S_{zA}, but to do it in as short as possible switching time.

However, the impossibility of achieving the complete switching of the inverter doesn't imply that it is impossible to perform the logical operation NOT at the unitary evolution stage. One just needs to ''read'' the signal at a time when $S_{zA(B)}$ has a large absolute value, e.g., at a time t_0. Indeed, $S_{zA}(t_0)\geqslant 0.45$ at any value of U/V (see Fig. 1). Hence, the error probability $P_{\text{err}}=1-p_1(t_0)$ (i.e., the probability of reading the ''wrong'' signal $S_{zA}=-1/2$ or $S_{zA}=0$ at a time t_0) is less than 0.1. Our calculations have shown that at $U/V\ll 1$ and at the ''optimal'' (for a given U/V) value of H_A/V the time t_0 is of the order of $\hbar/V$, i.e., $t_0\approx 10^{-13}$ s for $V\approx 10$ meV. The value of t_0 increases as U increases and reaches $\approx 6\hbar/V$ at $U/V=10$. The limiting value of t_0 at $U\gg V$ is $t_0=\pi\hbar U/4\sqrt{2}V^2$, in accordance with Ref. 7. Thus, to speed up the calculation, we should have small U and large V. If the shape of a single quantum dot is a cube with side length a and the distance between the quantum dots is d, then V is exponentially decreasing in both d and a, while U is roughly inversely proportional to a and is almost independent of d (Refs. 6,9). Hence, small values of d and a favor short switching times t_0 (the values of U and V can be calculated numerically for a given set of geometrical parameters of the quantum dot array and for a particular choice of semiconducting materials.[6]).

On the other hand, the ''optimal'' value of H_A increases with V as $H_A^{\text{opt}}=2V$ at $U=0$ (9) and as $H_A^{\text{opt}}=2V^2/U$ at $U/V\gg 1$ (see also Ref. 7). The product $H_A^{\text{opt}}t_0$ is of the order of $\hbar$ at any U/V. Hence, one can have a realistic value of $H_A^{\text{opt}}<1$ T only at the expense of increasing t_0 to $\approx 10^{-11}$s. Nevertheless, this value of t_0 is still several orders of magnitude smaller than characteristic inelastic relaxation times.[6]

In summary, the switching of the spin gate NOT (inverter) at the unitary evolution stage is much faster than through relaxation to a new ground state. The switching time can be reduced to 10^{-11} s, with an error probability of less than 0.1, through proper choice of the geometrical parameters of the quantum dots and strength of the local external magnetic field.

This work was supported by the Russian Fund for Fundamental Research under Grant 96-02-18918. We are grateful to S. Bandyopadhyay for sending us a preprint of the Ref. 7 prior to publication. We thank S. N. Molotkov for numerous valuable comments. Helpful discussions with V. F. Elesin, A. V. Krasheninnikov, and S. S. Nazin are gratefully acknowledged.

[a)]e-mail: opn@supercon.mephi.ru

[1] R. P. Feynman, Uspekhi Fiz. Nauk **149**, 671 (1986).
[2] S. Bandyopadhyay, B. Das, and A. E. Miller, Nanotechnology **5**, 113 (1994); S. Bandyopadhyay, V. P. Roychowdhury, and X. Wang, Phys. Low-Dim. Struct. **8/9**, 28 (1995).
[3] S. N. Molotkov and S. S. Nazin, JETP Lett. **62**, 273 (1995); Zh. Éksp. Teor. Fiz. **110**, 1439 (1996) [JETP **83**, 794 (1996)].
[4] A. V. Krasheninnikov and L. A. Openov, JETP Lett. **64**, 231 (1996).
[5] C. S. Lent and P. D. Tougaw, J. Appl. Phys. **74**, 6227 (1993).
[6] K. Nomoto, R. Ugajin, T. Suzuki, and I. Hase, J. Appl. Phys. **79**, 291 (1996).
[7] S. Bandyopadhyay and V. P. Roychowdhury, Superlatt. Microstruct., to be published.
[8] Yu. A. Izyumov, Uspekhi Fiz. Nauk **165**, 403 (1995).
[9] A. V. Krasheninnikov, S. N. Molotkov, S. S. Nazin, and L. A. Openov, Zh. Éksp. Teor. Fiz. **112** (1997) [JETP **85** (1997)], to be published.

Published in English in the original Russian journal. Edited by Steve Torstveit.